The influence of microstructure on the fracture behaviour of ferritic ODS steels

DISSERTATION

zur Erlangung des Grades eines Doktors

der Ingenieurwissenschaften

vorgelegt von

M.Sc. Aniruddh Das

eingereicht bei der Naturwissenschaftlich-Technischen Fakultät

der Universität Siegen

Siegen 2018

Betreuer und erster Gutachter

Prof. Dr.-Ing. habil. H.-J. Christ

Universität Siegen

Zweiter Gutachter

Prof. Dr.-Ing. Martin Heilmaier

Karlsruher Institut für Technologie

Tag der mündlichen Prüfung

17. Dezember 2018

Eidesstattliche Erklärung

„Ich erkläre hiermit an Eides statt, dass ich die vorliegende Arbeit ohne unzulässige Hilfe Dritter und ohne Benutzung anderer, nicht angegebener Hilfsmittel angefertigt habe. Die aus anderen Quellen direkt oder indirekt übernommenen Daten und Konzepte sind unter Angabe der Quelle gekennzeichnet.

Die Arbeit wurde bisher weder im In- noch im Ausland in gleicher oder ähnlicher Form einer anderen Prüfungsbehörde vorgelegt.

Es wurden keine Dienste eines Promotionsvermittlungsinstituts oder einer ähnlichen Organisation in Anspruch genommen."

Aniruddh Das

Acknowledgement

This present thesis is the result of my activities at the research group of Structural Materials in the institute Resource Ecology of Helmholtz Zentrum Dresden Rossendorf, Dresden, Germany (HZDR) with an affiliation as an external PhD student to the chair of Materialkunde und Werkstoffprüfung (LMW) at the Universität Siegen, Germany. First and foremost, I express my sincere gratitude to Dr. Viehrig and Dr. Altstadt for giving me the opportunity to do research on this very interesting and challenging topic. I am grateful to Prof. Christ for accepting me as an external PhD student and for his valuable guidance. I also thank Prof. Heilmaier for sharing his experience on this topic with us.

This thesis contributes to the Joint Program on Nuclear Materials (JPNM) of the European Energy Research Alliance (EERA). Research on this field would not have been possible without the wonderful support of all my colleagues. A friendly and encouraging working environment is indeed the most important ingredient for good research. I thank Dr. Viehrig, my immediate supervisor in HZDR, for his continuous support and guidance right throughout my time as a PhD student. I express my appreciation to Dr. Altstadt, Dr. Bergner and Dr. Heintze for the numerous discussion sessions which propelled my research in the right direction. My heartfelt thanks goes to Dr. Heintze for painstakingly correcting my errors, asking 'stupid questions', clarifying conceptual problems as well as for being a moral support throughout my tenure. The introduction of TEM in this work, which contributed greatly to the quality of this research, wouldn't have been possible without her efforts. The use of the HZDR Ion Beam Center TEM facilities and the support by its staff is gratefully acknowledged. In particular, the funding of TEM Talos by the German Federal Ministry of Education and Research (BMBF), Grant No. 03SF0451 in the framework of HEMCP is greatly acknowledged. I acknowledge Dr. Hoffmann from Karlsruhe Institute of Technology, who collaborated with us and provided us with valuable material inputs in terms of ODS steels.

I also take this opportunity to thank Wolfgang Webersinke, who efficiently managed and carried out all the mechanical testing, Gudrun Müller, for introducing me to SEM and EBSD and alongside performing various measurements on them, Mario Houska, for providing technical support and Michaela Rossner, for all the metallographic preparations and for the use of optical and stereo microscope. Additional thanks goes to our colleagues at the workshop for providing mechanical testing samples in a timely manner.

Last but not the least, I thank my friends and family for providing me with emotional support, without which this thesis would not exist.

Dresden, May 2018 Aniruddh Das

Contents

Symbols and abbreviations

Latin symbols

a	[mm]	Crack length
a_i	[mm]	Instantaneous crack length
Δa	[mm]	Crack extension
$A_{pl(i)}$	[J]	Instantaneous area under the load displacement curve
b	[mm]	Ligament length
b_i	[mm]	Instantaneous ligament length
b*	[nm]	Burgers vector
B	[mm]	Thickness of the C(T) specimen
B_N	[mm]	Net C(T) specimen thickness after side-grooving
C	[mm/N]	Compliance
C_{LL}	[mm/N]	Compliance at the load line
C_x	[mm/N]	Compliance at the shifted location
d	[nm]	Size of the void initiating particle
d_{eff}	[nm]	Effective size of the particle in the C-L orientation
d_{HD}	[nm]	Effective size of the particle in the HD region
d_{LD}	[nm]	Effective size of the particle in the LD region
E	[GPa]	Elastic modulus
G	[GPa]	Shear modulus
G_C	[kJ/m^2]	Critical energy release rate value for linear elastic materials
J	[kJ/m^2]	Energy release rate for elastic-plastic materials (J-integral)
J_i	[kJ/m^2]	Instantaneous J-integral value
$J_{el(i)}$	[kJ/m^2]	Elastic component of the instantaneous J-integral value
$J_{pl(i)}$	[kJ/m^2]	Plastic component of the iinstantaneous J-integral value
J_Q	[kJ/m^2]	Interim fracture toughness value for elastic-plastic materials
J_{IC}	[kJ/m^2]	Mode I critical energy release rate value for elastic-plastic materials

K_I	[MPa√m]	Mode I stress intensity factor for linear elastic materials
K_{IC}	[MPa√m]	Mode I critical stress intensity factor for linear elastic materials
K_i	[MPa√m]	Instantaneous stress intensity factor
K_{JQ}	[MPa√m]	Stress intensity factor corresponding to the J_Q value
K_{JIC}	[MPa√m]	Critical stress intensity factor corresponding to the J_{IC} value
K_{end}	[MPa√m]	Stress intensity factor at the end of fatigue pre-cracking
l	[mm]	Mean void initiating particle spacing
l_{eff}	[mm]	Effective inter-particle spacing in the C-L orientation
l_{HD}	[mm]	Effective inter-particle spacing in the HD region
l_{LD}	[mm]	Effective inter-particle spacing in the LD region
P	[N]	Load
$P_{(i)}$	[N]	Instantaneous Load
p	[-]	Fraction of particles encountered by the crack front
p_{HD}	[-]	Fraction of particles in the HD region encountered by the crack front
p_{LD}	[-]	Fraction of particles in the LD region encountered by the crack front
r	[-]	Rotation factor
T	[-]	Tearing modulus
w	[mm]	Width of the C(T) specimen
W	[J]	Work of adhesion or particle-matrix bond strength
x	[mm]	Distance of measuring point from the load line

Greek symbols

α	[-]	alpha fibre texture {100} <110>
Δ_{LL}	[mm]	Crack opening displacement at the load line
Δ_x	[mm]	Crack opening displacement at the shifted location
$\Delta_{elastic}$	[mm]	Crack opening displacement in the elastic regime
$\Delta_{plastic}$	[mm]	Crack opening displacement in the plastic regime
ε	[-]	Decohesion strain between particle and matrix
ε^*_f	[-]	Critical fracture strain

γ	[-]	Gamma fibre texture {111} <110>
ϑ	[-]	Poisson's ratio
φ_2, φ_1 and φ	[-]	Euler angles in the Euler space
σ_g	[MPa]	Hall-Petch strengthening
σ_d	[MPa]	Dislocation forest strengthening
σ_p	[MPa]	Nano-particle strengthening
σ_{YS}	[MPa]	Yield stress
σ_0	[MPa]	Yield stress
σ_f	[MPa]	Critical stress for void nucleation
σ_c, σ_{zz}	[MPa]	Constraint induced stress
σ_{yy}	[MPa]	Stress along the loading direction

Abbreviations

AISI	American Iron and Steel Institute
ASTM	American Society for Testing and Materials
BCC	Body-centered cubic
CCD	Charged-coupled device
COD	Crack opening displacement
CSM	Centro Sviluppo Materiali
C(T)	Compact tension
DBTT	Ductile to brittle transition temperature
dpa	Displacements per atom
EBSD	Electron backscatter diffraction
EDS	Energy dispersive X-ray spectroscopy
FCC	Face-centered cubic
FEG	Field emission gun
FM	Ferritic Martensitic
FWHM	Full width half maximum
GAR	Grain aspect ratio
Gen- IV	Generation IV

GFR	Gas-Cooled Fast Reactor System
GWd/t	Gigawatt-days/metric ton of heavy metal
HAADF	High-angle annular dark-field
HAGB	High-angle grain boundary
HD	High number density particle region
HE	Hot-extrusion
HIP	Hot iso-static pressing
HR	Hot-rolling
IPF	Inverse pole figure
IPF map	Inverse pole figure map
ITER	International thermonuclear experimental reactor
J-R curve	J resistance or J-integral versus crack growth curve
KIT	Karlsruhe Institute of Technology
LAGB	Low-angle grain boundary
LD	Low number density particle region
LFR	Lead-Cooled Fast Reactor System
MA	Mechanical alloying
MO	Misorientation
MSR	Molten Salt Reactor System
NFA	Nano-ferritic alloy
ODF	Orientation distribution function
ODS	Oxide dispersion strengthened
RAFMS	Reduced activated ferritic martensitic steel
R curve	Resistance curve
RT	Room temperature
SCWR	Supercritical-Water-Cooled Reactor System
SEM	Scanning electron microscope
SFR	Sodium-Cooled Fast Reactor System
S-Prism	Super-Power Reactor, Innovative, Small Module

SPS	Spark plasma sintering
SPT	Small punch test
STEM	Scanning transmission electron microscope
TEM	Transmission electron microscope
TMT	Thermo-mechanical treatment
UFG	Ultra-fine grain
USE	Upper shelf energy
VHTR	Very-High-Temperature Reactor System

Abstract

Oxide dispersion strengthened (ODS) steels are candidate materials for cladding tube and structural components in Generation IV nuclear fission reactors and as candidate materials for structural components in fusion devices. Fracture toughness is an important parameter required for the structural integrity and workability of a material. Despite having high strength at high temperatures and high irradiation swelling resistance, ODS steels have been known to possess lower fracture toughness than non-ODS ferritic martensitic steels, their immediate competitor. They also exhibit anisotropic fracture behaviour, especially for the hot-rolled and hot-extruded variants. In addition, ODS steels tend to form secondary cracks, which absorb energy but can lead to design problems.

In the present work, the microstructural features which cause low fracture toughness, anisotropic fracture behaviour and secondary cracking are investigated. This information can help manufacturers develop ODS steels with better fracture properties. Fracture toughness testing on three different batches of ODS steels are performed using miniature fracture toughness C(T) specimens using the unloading compliance method. The basic microstructure, fracture surfaces and crack propagation are investigated using techniques such as SEM, TEM and EBSD and compared with the fracture behaviour. A quantitative assessment of the microstructural parameters affecting fracture toughness is made using a critical strain based fracture toughness expression.

It was observed that the low fracture toughness of ODS steels is predominantly affected by the bond strength between the void initiating particle and the matrix. The size and inter-particle spacing of void initiating particles along with the yield stress did not dominantly affect the fracture toughness. The anisotropic fracture behaviour in ODS steels was found to be predominantly affected by the anisotropic grain morphology. Crystallographic anisotropy and anisotropy in void initiating particle distribution did not dominantly affect the fracture anisotropy. Secondary cracking favoured hot-rolled over hot-extruded specimens due to higher degree of microstructural anisotropy. Secondary cracks could stabilize primary crack propagation as well as prevent cleavage fracture at low temperatures. However, the drawback with secondary cracks was that they initiated earlier or at lower loads than the primary crack.

Kurzfassung

Oxidverfestigte Stähle (ODS) sind als Hüllmaterial für Brennstäbe in Generation IV Kernreaktoren und als Strukturmaterial in Fusionsreaktoren vorgesehen. Die Bruchzähigkeit ist ein wesentlicher Parameter für die Bewertung der strukturellen Integrität und die Bearbeitbarkeit. Ungeachtet einer guten Festigkeit bei hohen Temperaturen und einer guten Beständigkeit gegenüber bestrahlungsinduziertem Schwellen haben ODS-Stähle im Vergleich zu konventionellen martensitisch-ferritischen Cr-Stählen eine niedrige Bruchzähigkeit. Sowohl gewalzte als auch warm stranggepresste ODS-Stähle zeigen ein anisotropes Bruchverhalten. Zusätzlich treten Sekundärrisse auf, welche zu einem Versagen der Struktur führen können.

In der vorliegenden Arbeit werden die mikrostrukturellen Merkmale, welche für die niedrige Bruchzähigkeit verantwortlich sind, das anisotrope Bruchverhalten und das Auftreten von Sekundärrissen untersucht. Diese Informationen sind zur Verbesserung der Brucheigenschaften für Hersteller von ODS-Stählen von großer Bedeutung. Von drei ODS-Stählen wurden mit Miniatur-Kompaktzugproben Risswiderstandskurven mit dem Teilentlastungsverfahren gemessen und daraus Bruchzähigkeiten nach ASTM E1820 ermittelt. Die Mikrostruktur, die Bruchflächen und die Rissausbreitung wurden mit dem Raster- und Transmissionselektronenmikroskop und Elektronenrückstreubeugung untersucht und das Bruchverhalten charakterisiert. Eine quantitative Bewertung der die Bruchzähigkeit beeinflussenden mikrostrukturellen Parameter wird mit einer auf der kritischen Dehnung basierenden Beziehung der Bruchzähigkeit vorgenommen.

Es wurde beobachtet, dass die niedrige Bruchzähigkeit in erster Linie durch die Haftfestigkeit zwischen porenbildenden Teilchen und der Matrix bestimmt wird. Die Größe und der Abstand der porenbildenden Teilchen haben zusammen mit der Fließfestigkeit keinen dominanten Einfluss auf die Bruchzähigkeit. Es wurde festgestellt, dass das anisotrope Bruchverhalten der ODS-Stähle in erster Linie durch die anisotrope Struktur der Körner hervorgerufen wird. Kristallographische Anisotropie und Ausrichtung der Poren bildenden Teilchen haben keinen wesentlichen Einfluss auf das Bruchverhalten. Sekundärrisse treten durch den hohen Grad der Anisotropie bevorzugt bei warmgewalzten Material auf. Sie können das Wachsen des Hauptrisses und das Auftreten von Spaltbruch beeinflussen. Sekundärrisse entstehen vor der Ausbreitung des Hauptrisses bei geringerer Belastung.

1 Introduction

1.1 Background

Nuclear power plants are a well-established source of power production in the world, contributing about 13% of the electrical power demand worldwide [1]. While nuclear fusion is still a work in progress, nuclear fission reactors have been functional for a long time.

In the beginning of this century, a group of nations started working together for the research and development of advanced nuclear fission reactors, called Generation IV or Gen-IV type reactors, which would provide better sustainability, economics and safety [2]. In the nuclear fusion community, the European Union along with seven other countries are working on the International thermonuclear experimental reactor (ITER), which aims to produce more energy than the energy needed to initiate the fusion reaction. The materials used in such nuclear fission and fusion reactors would be exposed to high neutron doses (100-200 dpa) and high temperatures (550 - 650 ˚C). Under such harsh environments, a material suitable for application must possess the following properties for a longer operational life:

- High strength at high temperatures
- High ductility (also at low temperatures)
- Low activation
- Less irradiation induced swelling
- Less irradiation induced embrittlement
- High creep resistance at high temperatures
- High corrosion resistance at high temperatures
- High fracture toughness over a vast temperature range

Austenitic stainless steels and ferritic martensitic steels were seen as candidate materials which could satisfy the above mentioned properties. However they could not fulfil one or more of the properties required for nuclear application. Therefore, the focus was shifted to the development of novel materials which could retain high strength at temperatures close to 650 ˚C and were also resistant towards neutron irradiation induced effects.

Dispersion strengthening is a technique through which a material can be strengthened by introducing dispersoids which block dislocation motion. A novel alloy with Fe and Cr as base elements was developed which is strengthened with the help of dispersed oxide particles such as Y_2O_3 in high number density. These alloys came to be known as oxide dispersion strengthened (ODS) steels. They are typically manufactured by mechanical alloying the steel alloy powder with the Yttrium oxide powder followed by consolidation, hot-rolling, hot-extrusion and heat treatment.

ODS steels find their application in furnace construction, glass industry, combustion of waste materials, thermocouple protection tubes, high temperature testing equipment and combustion chamber for turbines [3]. In nuclear applications, ODS steels are candidate materials for making cladding tubes for Gen-IV nuclear fission reactors such as sodium fast reactors [4] and also for structural components [2]. Cladding tubes are used to separate the fuel rods and the coolant in nuclear fission reactors, serving as the first barrier against dissemination of fission products. Burn up, which is a measure of the energy extracted from a primary nuclear fuel source, is to a large extent dependent on the life of the cladding material [5].

ODS steels are also candidate materials for the blanket and the divertor section in fusion reactors [6]. The blanket in the fusion reactor engulfs the fusion confinement while the divertor removes the fusion reaction ash (α- particles or Helium), unburned fuel, and eroded particles from the reactor. Two variants of ODS steels have been the most prolific: the ferritic/martensitic ODS steels with Cr content in the range of 9-12 wt. % and the ferritic ODS steels with Cr content in the range of 12-20 wt. %. Ferritic ODS steels have higher corrosion resistance and do not go through any phase transformation at high temperatures.

1.2 Motivation

ODS steels retain their strength up to 650 ˚C and are resistant against thermal creep and irradiation swelling. However, they are known to possess poorer fracture toughness and ductility than ferritic martensitic steels, their closest competitor for nuclear applications. Components made out of ODS steels, such as cladding tubes, are also known to possess pronounced anisotropic properties owing to production methods such as cold pilgering, hot-extrusion and hot-rolling. In addition, they also can exhibit secondary cracking which absorb energy and retard primary crack propagation but can initiate at lower loads than primary cracks thus posing design problems.

Fracture toughness is an important characteristic of a material which determines its structural integrity, machinability/hot workability and the ability to absorb operational stresses arising from thermal and mechanical loads. Fracture toughness testing provides a value which can be utilized directly for structural integrity assessment. The test works on the principle in which a sharp crack is loaded rather than a notch which can be related to real components where sharp microcracks are inevitable. An acceptable limit of fracture toughness for ODS steels ($K_{JQ} \geq 100$ MPa$\sqrt{m}$) was defined by Byun et al. [7]. Fracture toughness is dependent on the microstructural features of the material, which can be deliberately tailored. The fracture surfaces give information about the dominating fracture mechanisms, which depend on the microstructure and anisotropy of the material. Fracture toughness along with the fracture mechanisms constitutes the fracture behaviour of a material.

1.2.1 Problem definition

In the context of fracture behaviour of ferritic ODS steels, the three main areas on which this thesis is focussed are:

- **Fracture toughness of non-irradiated material**: ODS steels are generally known to exhibit inferior fracture properties as compared to ferritic martensitic non-ODS steels. Knowledge about the microstructural parameters which affect the fracture toughness in the non-irradiated form can help manufacturers to tailor ODS steels with better fracture toughness. The effect of irradiation on fracture toughness is also interesting but is beyond the scope of this thesis.
- **Anisotropic fracture behaviour**: The fracture mechanisms that lead to anisotropic fracture behaviour in ODS steels are interesting and have not been studied in great detail. These fracture mechanisms arise from the microstructural anisotropy (grain morphology anisotropy, sub-micron particle anisotropy and crystallographic anisotropy) which in turn is dependent on the composition of the material and the manufacturing method. A better understanding of the factors leading to anisotropic fracture behaviour can lead to mitigation of fracture anisotropy or to introduce fracture anisotropy in a beneficial manner.
- **Secondary cracking:** are often found in ODS steels and some non-ODS steels. They absorb energy but can lead to design problems due to their early initiation. Secondary cracking appears more often in hot-rolled than in hot-extruded materials. The reason why secondary cracking favours materials manufactured through certain manufacturing processes and also favours materials in certain orientations in not clear. This research focuses on answering these questions. The fracture mechanisms of secondary cracking are also discussed. Knowledge about factors affecting secondary cracking and their mode of fracture allows the avoidance or utilization of them in certain orientations, where they can be beneficial.

1.3 Approach

Three different ferritic ODS steels in their non-irradiated form are used in this research. Two of the three ODS steels possess the same chemical composition (13 wt. % Cr) and two were produced using the same manufacturing technique (hot-extrusion). Two batches of 13 wt. % Cr ODS steels were manufactured in Karlsruhe Institute of Technology (KIT), Germany, one using hot-rolling and the other using hot-extrusion. The third batch of ODS steel (14 wt. % Cr) was manufactured by Centro Sviluppo Materiali (CSM), Italy using hot-extrusion.

In the results section, a detailed characterization of basic microstructure using optical, scanning electron, electron backscatter diffraction and transmission electron microscopy is presented for these three materials. This is followed by tensile and fracture toughness test results obtained through miniature specimen testing from room temperature (RT) up to 600 ˚C in different orientations. Primary crack propagation was investigated using EBSD measurements on the side surfaces of C(T) specimens in

different orientations after fracture toughness testing. The primary and secondary fracture surfaces of C(T) specimens were then exposed and investigated using stereo and scanning electron microscope after breaking them apart.

Fig. 1 shows a flowchart of the three ODS materials used in this research along with the focus areas (described in 1.2.1) to which they predominantly contribute. These focus areas will be further explored in the discussion section.

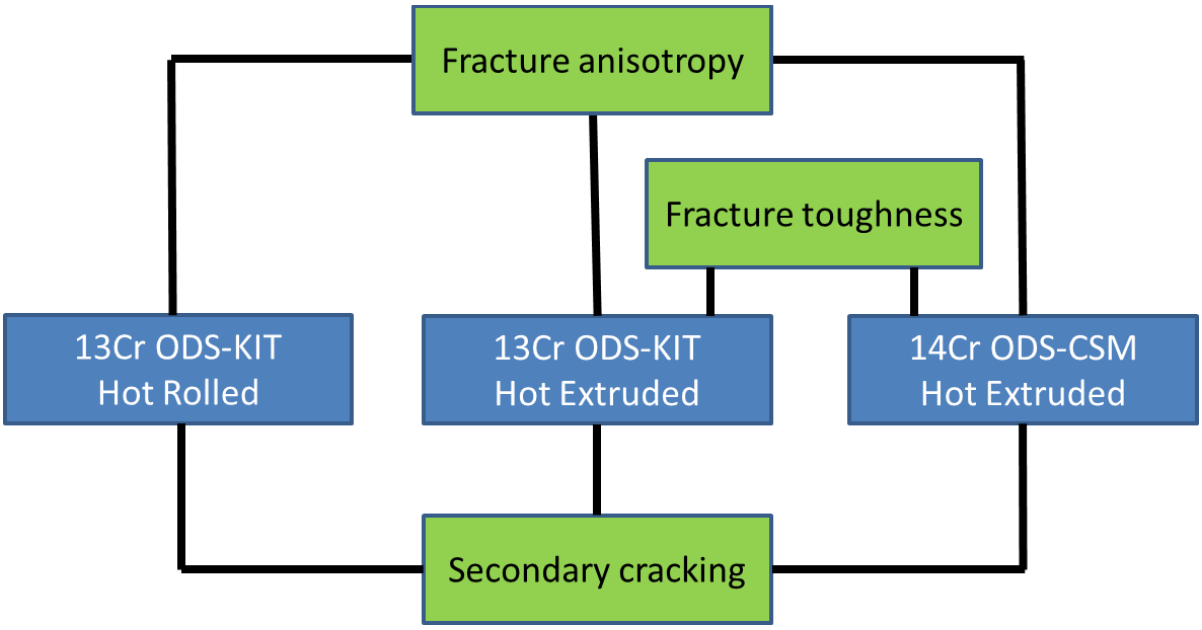

Fig. 1 Flowchart of the ODS steels together with the focus areas to which they contribute.

- The microstructural factors affecting the **fracture toughness** are predominantly discussed by comparing **two hot-extruded ferritic ODS steels of different compositions**. A quantitative assessment on the microstructural features playing a dominant role in inducing high and low fracture toughness is presented.
- **Fracture anisotropy** is discussed by assessing the microstructural anisotropies in **all the three ODS steels**. Hot-rolling and hot-extrusion are commonly used fabrications steps for manufacturing thin plates and rods of ODS steels respectively. A quantitative assessment based on the microstructural factors affecting the fracture anisotropy is presented.
- **Secondary cracking** is discussed by comparing **all the ODS steels**. A comparison, along with reasons for the extent of secondary cracking in hot-rolled and hot-extruded materials is made. The fracture mechanisms of secondary cracking and its role in stabilization of the primary crack are also discussed.

2 State of the art

2.1 Nuclear fusion and fission

2.1.1 Nuclear fusion

The energy produced by the combination of two light nuclei was achieved in 1951and was tipped to be the solution to the increasing energy demands of the world. Till now, however, no design has produced more fusion energy than the energy needed to initiate the reaction. This is the aim for ITER which plans to begin its first plasma in seven years from now [8].

The core of the nuclear reactors is essentially a plasma, where the fuel (Deuterium and Tritium) reaches extremely high temperatures and fuses together to release energy and neutrons. These neutrons carry 80% of the energy and are captured by a thick blanket which engulfs the fusion confinement [6]. This blanket is made with the combination of various materials, such as Li to breed more tritium and materials which can withstand high temperature, high neutron dose and erosion through sputtering. The average temperature of a blanket is 500 °C. The divertor, on the other hand, is located at the bottom of the fusion confinement and keeps the plasma clean by removing He ash, unburnt fuel and eroded particles from the reactor. As the divertor receives the flow of all the plasma components, it has a high heat flux. Temperatures of 1000 °C to 1500 °C have been observed in the divertor section. Materials which are suitable for the blanket or for the divertor section must be resistant against irradiation induced degradation of mechanical properties and should possess sufficient creep strength up to high temperatures.

2.1.2 Nuclear fission

Nuclear fission occurs when heavy nuclei such as uranium 235 split up after being bombarded with neutrons to produce lighter nuclei, energy and more neutrons. A coolant is used to harness this energy and drive a turbine. A clad or a cladding tube is a component of the nuclear fission reactor, which is used to protect the fuel from the environmental exposure to coolant. The cladding tube should have a low cross-section for the capture of neutrons, which are essential for the sustainability of the fission reaction. Zirconium alloys were often used as cladding material as it has very low absorption cross-section of thermal neutrons, high hardness, high ductility and corrosion resistance. However, zirconium alloys can suffer from hydrogen embrittlement which occurs after reaction of water with zirconium forming hydrogen gas and hydrides.

In nuclear power technology, burnup (also known as fuel utilization) is the actual energy released per mass of initial nuclear fuel in gigawatt-days/metric ton of heavy metal (GWd/t). Generation II reactors were typically designed to achieve about 40 GWd/t. With advancements in fission technology, a higher burnup of over 100 GWd/t is envisaged which imposes a number of requirements for cladding materials, including resistance to neutron irradiation embrittlement, dimensional stability under irradia-

tions, corrosion resistance, low susceptibility to stress corrosion cracking and hydrogen and/or helium embrittlement, high-temperature strength and long creep life.

2.1.3 Generation-IV reactors

Such desire for advancements in nuclear technology has resulted in the formation of collaborative efforts between various nations to come up with the concept of Generation IV reactors. The advantages of Gen-IV reactors over previous reactor systems are higher burnup, faster decay of radioactive waste and improved safety features [2]. These requirements result in more severe operation conditions including higher temperature, higher neutron dose and more corrosive environment. There are six proposed systems for Gen-IV reactors. The operating temperature and neutron exposure of these systems are shown in Fig. 2 [9]. The candidate cladding and structural materials which are suitable for these reactors as have been listed in Table 1 [2].

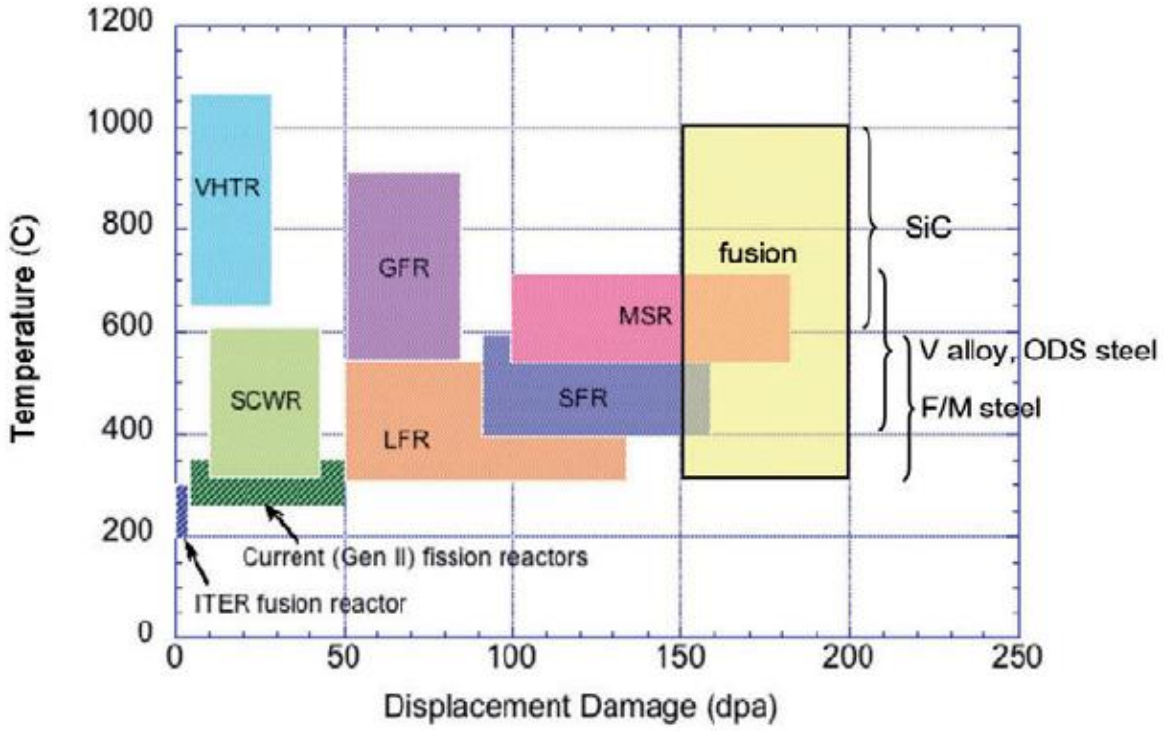

Fig. 2 Overview of operating temperatures and displacement damage dose regimes for structural materials in generation II and proposed future (Generation IV) fission and fusion energy systems. The six Gen IV fission systems are Very High Temperature Reactor (VHTR), Super Critical Water Reactor (SCWR), Lead Fast Reactor (LFR), Gas Fast Reactor (GFR), Sodium Fast Reactor (SFR), and Molten Salt Reactor (MSR) [9]

Table 1 Candidate cladding and structural materials for Gen-IV reactors [2]

System	Cladding material	Structural Materials	
		In-core	Out-of-core
GFR	Ceramic	Refractory metals and alloys, Ceramics, ODS Vessel: FM	Primary Circuit: Ni-based superalloys
LFR	High-Si FM, Ceramics, or refractory alloys		High-Si austenetics, ceramics, or refractory alloys
MSR	Not applicable	Ceramics, refractory metals, High-Mo Ni-based alloys, Graphite, Hastelloy N	High-Mo Ni-base alloys
SFR	ODS	FM ducts, 316SS grid plate	Ferritics, austenitics
SCWR	FM (12Cr, 9Cr, etc.), Incoloy, ODS	Same as cladding	FM
VHTR	ZrC coating and surrounding graphite	Graphite PyC, SiC, ZrC, Vessel: FM	Ni-based superalloys, ODS

2.2 ODS steels

2.2.1 History

The development of ODS steels began with a necessity to produce a material suitable for Gen-IV type nuclear fission reactors and fusion devices. Initially, Ni-based super alloys were an obvious choice as they are known for their high temperature creep strength and oxidation resistance. Ni, however, is more expensive than Fe and suffers from the problem of activation [10]. Ni also produces large quantities of He bubbles which results in irradiation induced damage [11,12]. Austenitic stainless steels were tried thereafter as they exhibit good strength and ductility up to 600 ˚C. However, they are prone as well to irradiation induced swelling and embrittlement owing to its face-centered cubic (FCC) crystal structure [13]. Focus then shifted to ferritic martensitic steels which combine high corrosion and creep resistance at low costs. They exhibit high resistance against irradiation induced swelling and even exhibit high fracture toughness both at room and at operating temperatures [7,14]. However, it was found that they contain certain elements which get activated under irradiation. Therefore, these elements were avoided in ferritic martensitic steels in order to simplify the radioactive waste disposal problem by faster radioactive decay [10,15]. Materials which exhibited high induced radioactivity like

cobalt in combination with nickel, molybdenum and niobium were avoided and replaced with tungsten and vanadium [16]. This class of materials is known as reduced activated ferritic martensitic steels (RAFMS). However, they exhibit high strength only up to 550 ˚C which is below the desirable operation temperature envisaged for Gen-IV type nuclear fission reactors and fusion reactors. Addition of fine oxide particles in RAFMS gave rise to ODS steels which combines the advantages of RAFMS along with the improvements related to oxide dispersion strengthening such as high creep resistance up to 650 ˚C and high resistance against irradiation induced effects [17,18].

2.2.2 Manufacturing

To manufacture ODS steels, mixing oxides and steel alloy powder in a traditional melt metallurgical procedure is almost impossible due to insufficient wetting of the powder and agglomeration problems. Therefore, ODS steels are produced by powder metallurgy. They are typically produced by mechanically alloying the gas atomized steel alloy powder together with oxide powders such as Y_2O_3, which are considered one of the most thermodynamically stable material [14,19]. The milling parameters such as milling speed, time, atmosphere and ball to powder weight ratio play an important role in the final microstructure. They then go through a process of canning, degassing, followed by hot isostatic pressing (HIP) to make fully dense and homogenous structures. The consolidation temperature plays an important role in the volume fraction, number density and size of the dispersed particles [20]. Post processing methods like hot-extrusion (HE) and hot-rolling (HR) often follow along with heat treatments to complete the manufacturing process. This production route is well established but expensive. A typical flowchart of the manufacturing process is shown in Fig. 3.

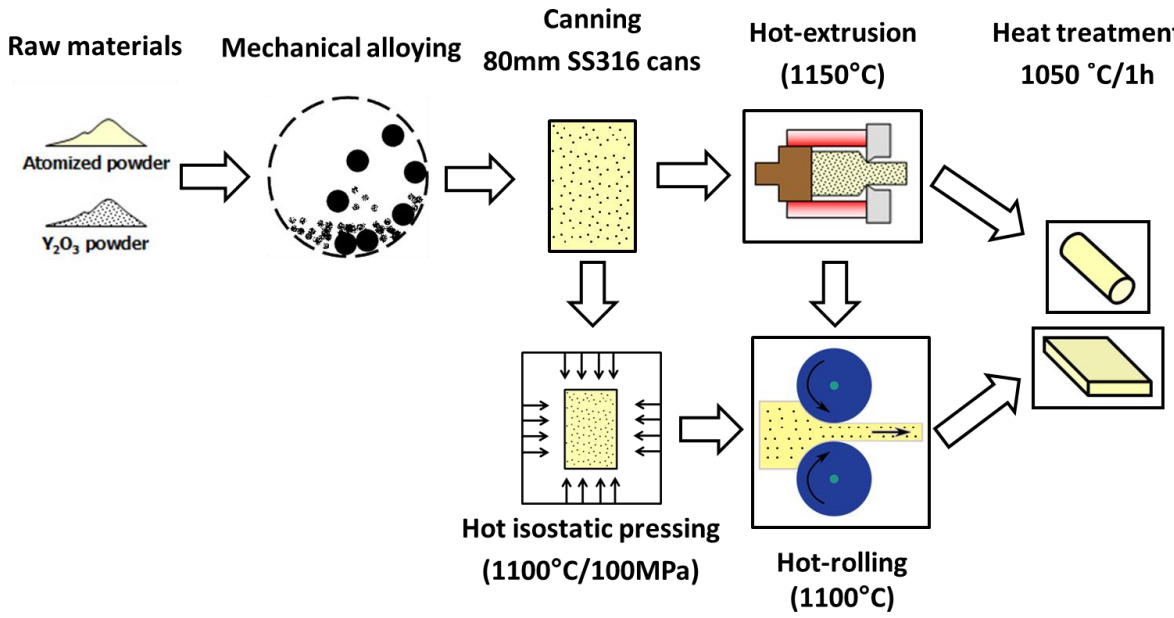

Fig. 3 Typical manufacturing process of ODS steel production.

2.2.3 Basic microstructure

The basic microstructure of ODS steels consists of high number density (> 10^{23}) of nano-particles in the size range of 1-10 nm [14,21–27] and sub-micron particles in the size range of 100-1000 nm [28,29]. The nano-particles are reported to be Y, Ti and O-enriched [21,23,26,29,30]. The most common structures reported are $Y_2Ti_2O_7$ [19,31–34] and Y_2TiO_5 [19,34,35]. Alinger et al. [20] used small-angle neutron scattering (SANS) and suggested that Y_2O_3 may dissociate into Y and O, which then forms a solid solution with the Fe alloy matrix. There is ongoing uncertainty and ambiguity as to the precise mechanism, and whether one or more mechanisms may operate under any particular set of milling conditions [36]. Ti was found to play a significant role in nano-particle refinement [31,32,37]. ODS nano-particles act as defect trapping sites increasing the swelling resistance. ODS nano-particles also lead to fine-grained microstructure due to their pinning effect. Fine grains have defect trapping ability which further improves swelling resistance. ODS nano-particles and fine grains also help improve material strength through Orowan and Hall-Petch relation, respectively [38].

Presence of alumina stringers in the microstructure was also reported in certain works which was either a product of contamination during manufacturing process, or due to Al presence in the ODS steel matrix [25,27,33,39,40] added for corrosion resistance enhancement. Elongated microcracks may exist due to improper sintering followed by rolling or extrusion. These microcracks can hamper the ductility and fracture toughness of the material [41,42].

Sometimes, ODS steels are also referred to as nano-ferritic alloys (NFAs). These usually refer to even finer microstructures, with Cr content more than 12 wt.%, nano-particles in the size range of 1-10 nm and grain sizes in the sub-micron range [14,22,27]. The particles are often not distributed homogenously. This, along with inhomogeneous temperature distribution during sintering and inhomogeneous dislocation density after mechanical alloying, leads to inhomogeneous recrystallization resulting in bimodal grain size distribution [43]. This recrystallization is dynamic in nature and may take place several times during the course of consolidation [3].

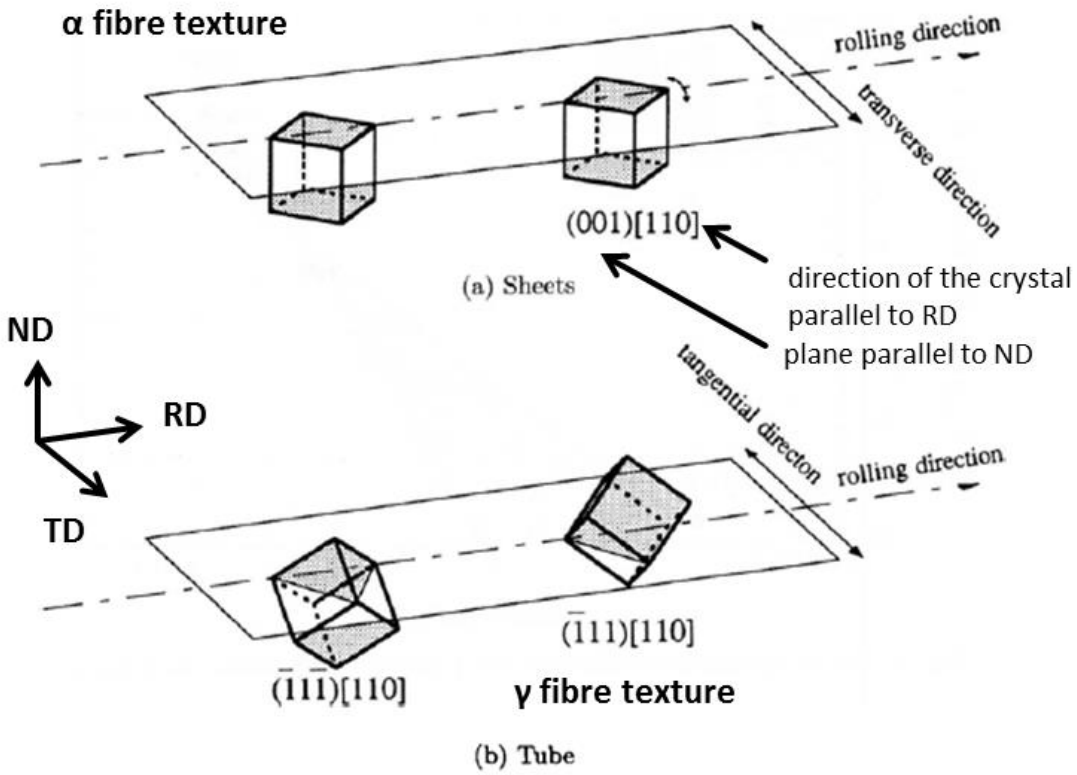

Fig. 4 Schematic of texture components developed in ODS ferritic a) sheets and b) cladding tubes [44].

Hot-rolling and hot-extrusion are known to refine the grain structure but they also induce anisotropy [27,45]. α fibre texture of {100} <110> [44,46,47] was reported in sheets while γ fibre texture {111} <110> were reported in cladding tubes [44] (Fig. 4). This means that the {100} and {111} planes are parallel to the rolling plane respectively and are directed towards the [110] direction. Materials manufactured through hot-extrusion exhibited a crystallographic texture with grains oriented in the <110> direction parallel to the extrusion direction [25,27,48]. The grains are often observed to be elongated in the direction of rolling/extrusion. The ideal orientations of texture components in body-centered cubic (BCC) materials was reported in previous works [49,50] using ODF plots at the constant Euler angle φ_2 of 0˚ and 45˚ as shown in Fig. 5.

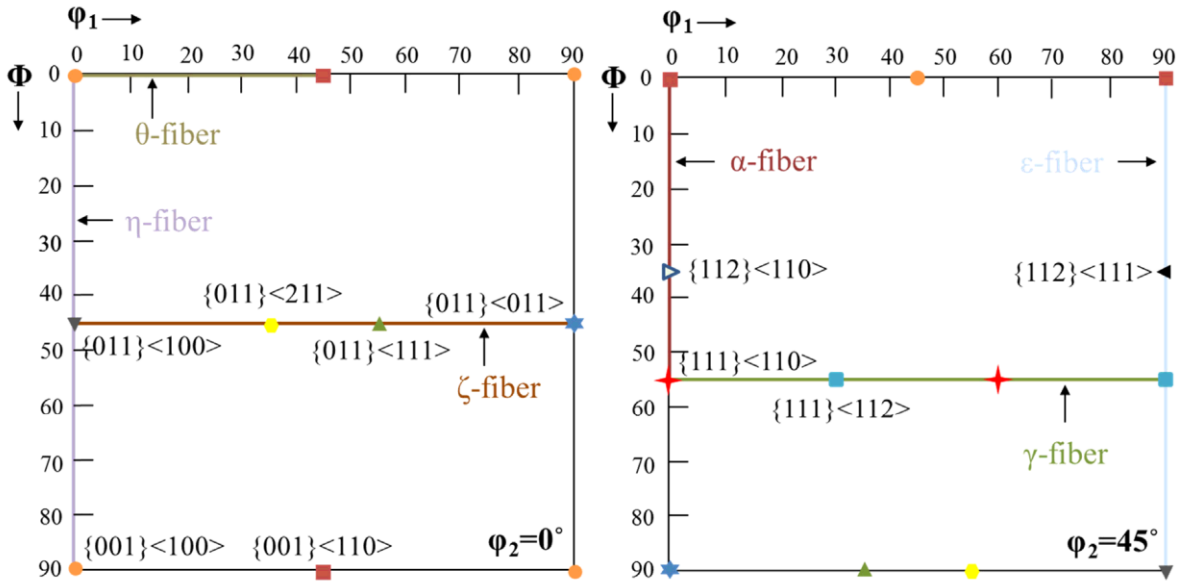

Fig. 5 Schematic illustration of the important texture components in BCC materials [50].

2.2.4 Strengthening mechanisms in ODS steels

ODS steels make use of a combination of strengthening mechanisms which results in its superior strength. The yield stress of an ODS material at RT can be written in terms of some dominant strengthening mechanisms [51].

$$\sigma_{ys} = \sigma_g + \sqrt{{\sigma_d}^2 + {\sigma_p}^2} \quad (1)$$

where σ_g, $\sigma_d$and σ_p are the contributions from Hall-Petch strengthening, dislocation forest strengthening and nano-particle strengthening, respectively. When dislocations pile up at the grain boundaries, a threshold stress needs to be exceeded in order for the dislocations to pass on to the next grain. The smaller the grain size is, the higher the Hall-Petch strengthening (σ_g) is. Dislocation forest strengthening (σ_d) is due to the interaction between dislocations while nano-particle strengthening (σ_p) comes from the interaction between dislocations and nano-particles, which are less than 50 nm in size. If the particles are small and coherent with the matrix, the dislocations might cut them. If the particles are large enough and incoherent, then the dislocations bow. In ODS steels, the dislocations are pinned by the nano-particles, which subsequently bow between two particles and unpin to form dislocation loops around the particles. The strengthening induced by dislocation bowing is known as Orowan strengthening and the dislocation loops as Orowan loops. The share of nano-particle strengthening to the yield stress is dominant at RT [51]. In addition, there are also contributions from lattice friction, the stress required to move a dislocation through a perfect lattice and solid solution strengthening, the obstruction of dislocation motion caused by strain fields induced by substitutional and interstitial atoms. However, the last two are not the dominant contributors.

At the high temperature regime (T ≥ 700 °C), the athermal components such as Hall-Petch strengthening and dislocation forest strengthening reduces drastically and the grain boundaries become weak

[52].Strengthening by nano-particles however, still functions at this temperature. An additional thermally activated detachment stress, faced by the dislocation at the departure side of nano-particle, is also active at this temperature [53].

2.2.5 Mechanical properties and fracture toughness

ODS steels possesses excellent strength due to high number density of oxide particles in the nanometer size range which obstructs the dislocation movement [54]. These nano-particles exhibit good high temperature stability and therefore can maintain the strength of the alloy, even above 600 ˚C. ODS steels also possess high temperature creep resistance [4,30,40,48,55–58], exhibit high resistance against irradiation induced swelling [4,11,14,59,60] and embrittlement [11,61,62]. The ductility of ODS steels is often lower than ferritic martensitic steels but is still above acceptable limits [61,63–65].

Fracture toughness of non-irradiated ODS steels have previously been investigated using fracture toughness compact tension (C(T)) [22,47,48,66] and three point bend specimens [23,24,61,67–69]. Fig. 6 shows a graph from a comprehensive study performed by Byun et al. [7], where only a handful of ODS steels were reported to exhibit acceptable fracture toughness ($K_{JQ} \geq 100$ MPa$\sqrt{m}$) along with high yield stress at high temperatures (500 - 600 ˚C). The cloud of ODS steel variants possessing an acceptable fracture toughness and a high yield stress at a temperature range of RT to 300 ˚C was larger. It was found that ODS steel often possess lower fracture toughness than non-ODS ferritic martensitic (FM) steels [7,23,66,70] at RT (Fig. 7). The difference can be even more pronounced at higher temperatures (comparing Fig. 6 and Fig. 7) [7]. The microstructural factors which are responsible for high and low fracture toughness in certain ODS steels are explored through this research.

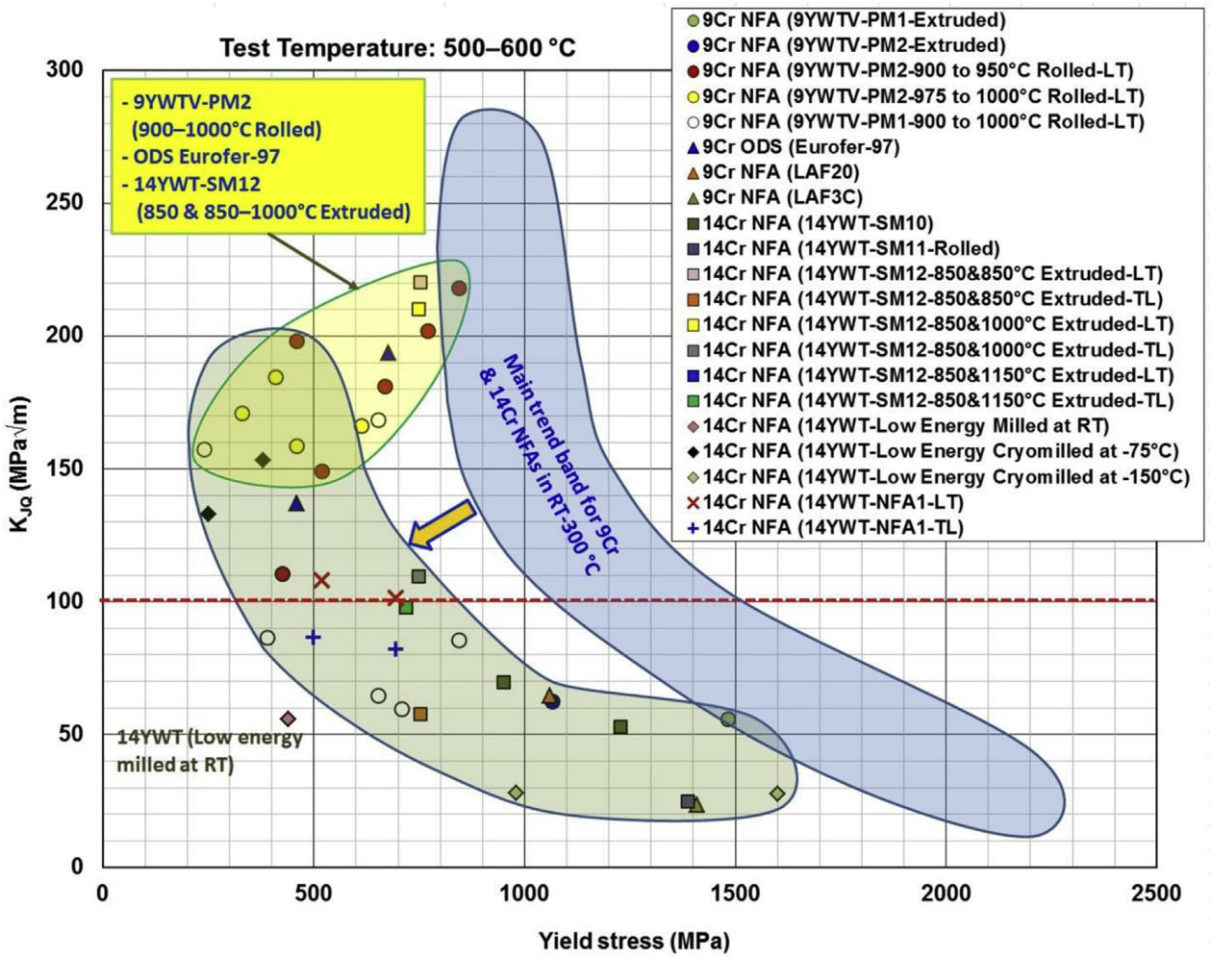

Fig. 6 Fracture toughness versus yield stress plot for major ODS steels tested in a high temperature region of 500-600 ˚C [7]. The plot for the low temperature region (22-300 ˚C) is also shown for comparison.

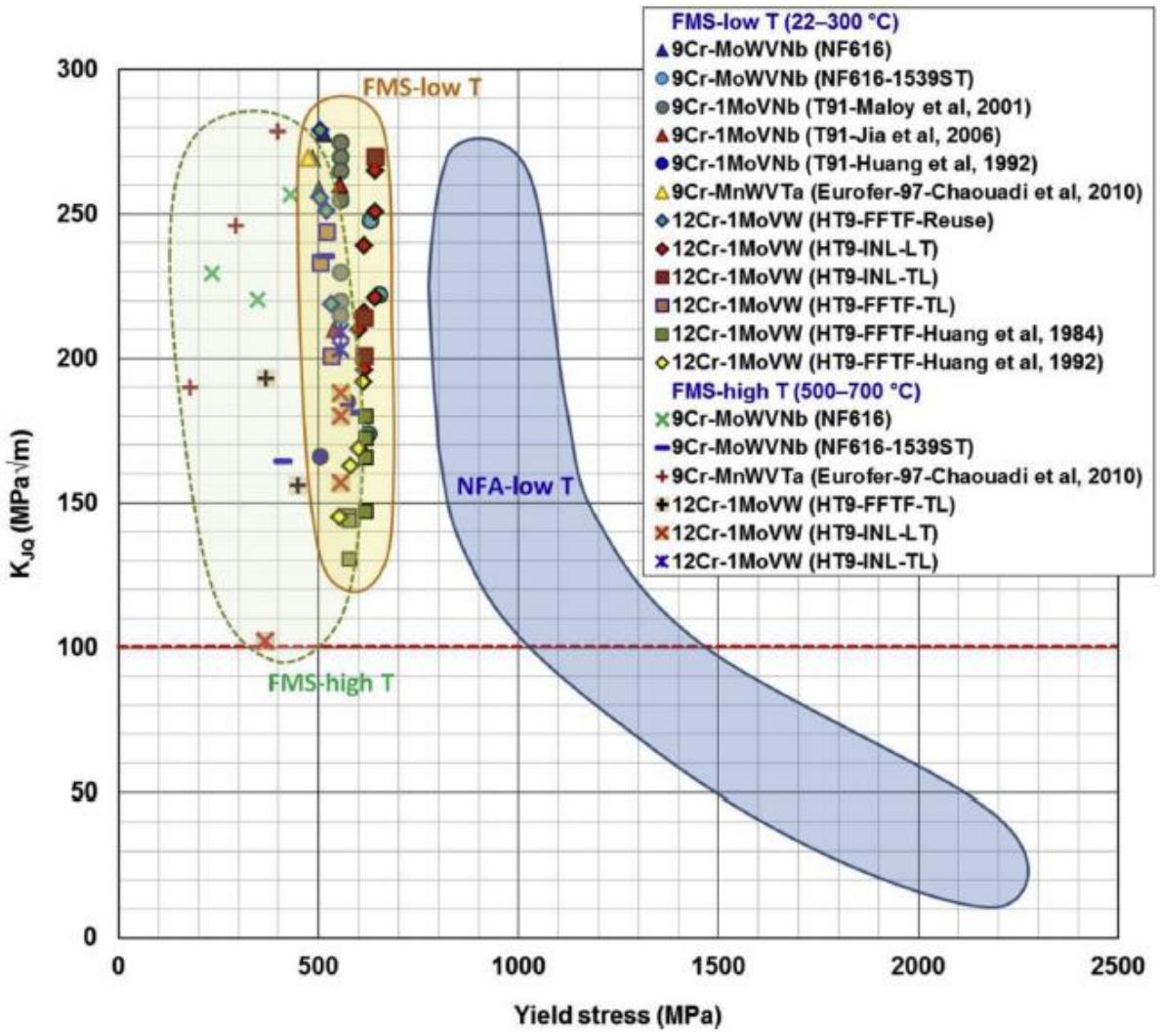

Fig. 7 Fracture toughness versus yield stress plot for major ferritic-martensitic steels tested in low-temperature (22-300 ˚C) and high-temperature (500-600 ˚C) regions along with ODS steels tested in the low-temperature region (22-300 ˚C) [7].

2.2.6 Fracture anisotropy of ODS steels

Fracture anisotropy of ODS steels have previously been investigated using tensile [23,39,48,55,71–73], Charpy impact [27,29,39,46,48,74–79], three point bend [24,67] and fracture toughness compact tension (C(T)) specimens [47,48].

Fracture toughness anisotropy was observed in both hot-rolled [29,47,74,77] and hot-extruded materials [29,39,77,78], with the highest fracture toughness in specimens with crack propagation perpendicular to the rolling/extrusion direction. It was also reported that hot-extrusion resulted in better fracture properties than hot-rolling [27,29,77].

The explanation for the anisotropic fracture behaviour has been a point of debate. Byun et al. reported debonding of oxide coated aggregates of grains formed in the canning process after milling [42] while

others have mentioned segregation of carbides and oxides at grain boundaries, which are formed after post processing, promoting intergranular fracture along elongated grains [39,75,78,80].

A significant part of this research has been dedicated to understanding the anisotropic fracture properties of ODS steels and its relation to the microstructure.

2.2.7 Secondary cracking

Secondary cracks are a striking feature often observed on the primary fracture surfaces of ODS materials tested close to RT in certain orientations. Secondary cracking has also occasionally been observed in some non-ODS steels, e.g. low carbon steels [81,82] and FM steels [83], however, it appears to be less common. Secondary cracks propagate in a plane perpendicular to the primary crack plane and are formed due to constraint induced stress. Fig. 8 shows a primary crack fracture surface containing secondary cracks. Different primary crack growth regions have also been highlighted.

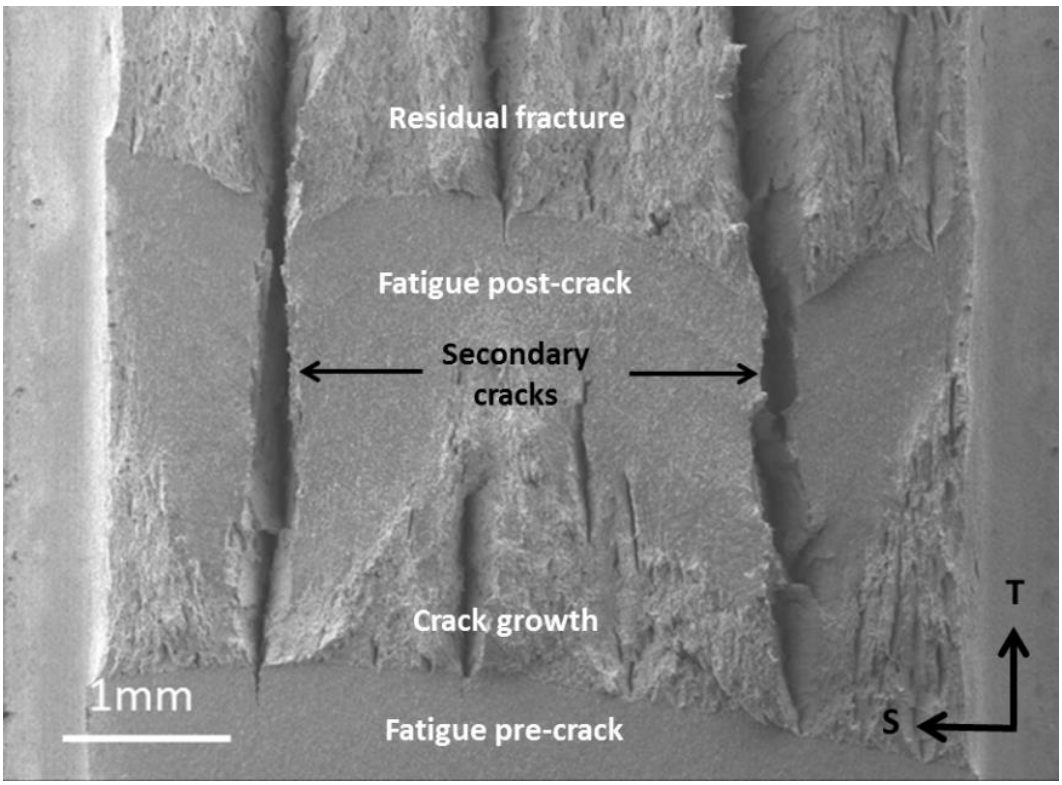

Fig. 8 A typical macroscopic SEM image of the primary crack fracture surface of an ODS steel at RT indicating different primary crack propagation stages and secondary cracks in the L-T orientation.

Secondary cracks may appear under certain conditions due to the phenomenon of delamination [74,75,81,82], also known as splitting [29,71,74,81], which inhibits the primary crack propagation. The term delamination was first taken from composites where it means separation of different composite layers through an interfacial mechanism. Although ODS steels have some similarity to composites, it is highly unlikely that delamination in ODS steels takes place at the interfaces of different layers as there is no sharp transition between different material zones.

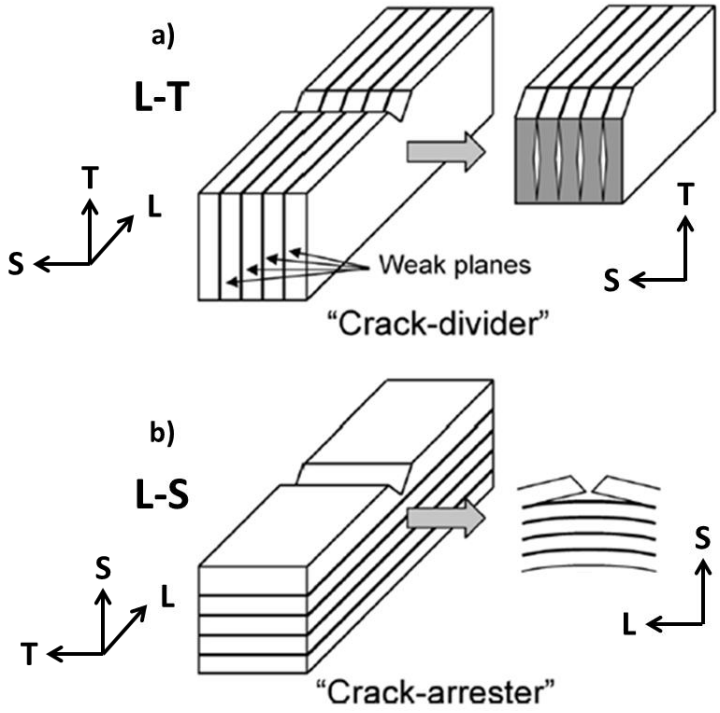

Fig. 9 Schematic illustration showing the two most common splitting geometries for the a) L-T and the b) L-S oriented specimen machined from a hot-rolled material [84].

Delamination can transpire in two configurations, the "crack-divider" and the "crack-arrester" geometries, both associated with hot-rolled specimens as shown in Fig. 9 [84]. Secondary cracks seem to accompany delamination in certain sample orientations, such as L-T and T-L in hot-rolled materials, which are classified as crack divider geometries [84]. Crack divider geometries have a specific primary crack propagation direction with respect to the anisotropic microstructure. These secondary cracks divide the specimen thickness into sub-specimens (Fig. 9a). The state of constraint near the primary crack is relaxed which retards the primary crack growth. Crack arrestor geometry, however, is associated with the L-S and T-S oriented samples in hot-rolled materials. In the crack arrester geometry, delamination deflects the primary crack through 90˚ and the fracture mode changes from mode I to mode II [67,74]. No secondary cracks are formed in the crack arrestor configuration (Fig. 9b). It is noteworthy, that in some publications, secondary cracking and delamination are used as synonyms. In this work however, a clear distinction between the two is made. The delamination geometries used for hot-rolled specimens like crack arrestor and crack divider are not usually used for hot-extruded specimens. It was observed that hot-rolled ODS steels exhibited greater propensity to secondary cracking [29,42,66,74,75,77,85] than hot-extruded ODS steels [29,77,78].

It has been found experimentally as well as by 3D finite element computations, that delamination can result in increased energy absorption [66,67,86]. The energy absorbed in crack arrestor geometry is usually higher than that of crack divider geometry. It was also found that secondary cracks resulting from delamination in the crack-divider geometry were beneficial for preventing cleavage fracture [14,67] and for stabilization of primary cracks [47].

It was found that in the brittle regime, secondary cracks were facilitated due to the {100} cleavage planes in hot-rolled materials [46,74]. In general, weak planes have been reported to be the primary cause for secondary cracks; however the source of weak planes remains a point of debate [39,75,78,87].

The reasons why secondary cracks are favoured in certain materials and in certain orientations will be discussed in more detail. The effect of secondary cracks on the primary cracks and on the overall fracture toughness is also discussed.

2.2.8 Development in ODS steel manufacturing

Fracture toughness at low temperatures has been above the acceptable limit for many ODS steels [7] but low fracture toughness at high temperatures has been a major cause of concern (Fig. 6). Different combinations of processing parameters and thermo-mechanical treatment have been carried out to increase the bonding between the grains at high temperatures. Thermo-mechanical treatment (TMT) such as controlled hot-rolling in 9Cr ODS steel was found to increase fracture toughness by diffusion bonding between different phases [88]. However, with ferritic ODS steels; diffusion bonding is not effective due to the absence of phase transformation. Similar heat treatments were nevertheless tried on ferritic ODS steels to find some improvements in fracture properties [26,27]. However, they were still not satisfactory enough. Hot forging was tried to get more homogenous microstructure, however the fracture toughness was reported to be reduced [89].

Higher tensile strength was obtained by milling at low temperatures (-150 ˚C), with higher milling speeds and at lower HIPing temperatures [90]. This however resulted in higher nano-particle number density at the grain boundaries which lowered the ductility and also lowered the fracture toughness.

Cross rolling and annealing after hot-extrusion proved to be effective in preventing bimodality in grain distribution [14] but could not increase ductility [72]. Cross rolling is nevertheless helpful to prevent extreme anisotropy in grain structure.

Alternate methods of fabricating ODS steels are also currently being developed. Among them, spark plasma sintering (SPS) has been found to reduce the processing times and thermal exposure during processing [36]. It was successfully scaled up to produce low-porosity compacts of semi-industrial size with nano-particles in low nm range and nano-grains [91,92].

Additive manufacturing techniques such as selective laser melting and electron beam melting can be used to design complex shapes. They do not replace the mechanical alloying (MA) stage, but instead the consolidation and post-processing steps. Methods such as controlled oxidation try to replace the MA stage, which reduces costs but can induce contamination and bimodality in the grain structure. Spray forming and melt spinning also work towards the same goal [36].

Liquid metal processing may provide advantages of low cost and high scalability. However due to poor wetting and agglomeration problems of ODS particles, they are still in the development stage. In

order to avoid agglomeration, powerful agitation techniques such as contactless magnetic stirring and cavitation induced through alternating magnetic fields are presently being developed [93].

2.3 Fracture behaviour

2.3.1 Fracture mechanisms

In BCC crystals, although there are as many total number of slip systems as in FCC crystals (12), the movement of dislocations happen only as a line of atom jumps from one potential energy valley to another. This is due to the fact that no real closed packed planes exist in BCC lattice. This process is thermally activated; therefore BCC materials are ductile at high temperatures and brittle at low temperatures. There is a particular range of temperature for each material, represented by ductile to brittle transition temperature (DBTT), where this shift of fracture mechanism happens. The DBTT and the upper shelf energy (USE) can be found out by impact testing. DBTT is dependent on the microstructural features of the material, the loading rate, the loading and the crack propagation direction. The DBTT of ODS steels is usually higher and the USE lower than that of ferritic martensitic steels [32,94]. Other testing methods, such as quasi-static fracture toughness testing also exhibit a ductile to brittle transition range, but the absolute value is different to the one obtained by impact testing.

In ODS steels at temperatures close to RT, cleavage, intergranular and ductile fractures may prevail depending on the DBTT of the material. At temperatures below the DBTT, cleavage and intergranular fracture compete depending on the ratio of shear and bulk modulus [95]. At temperatures above DBTT but below 600 ˚C, ductile fracture prevails as the crack tip is able to emit dislocations and crack blunting takes place. At high temperatures (> 600 ˚C), the fracture morphology changes into particle like nano-features from a wide dimple structure due to grain boundary decohesion [42,96]. Deformation mechanisms such as grain matrix deformation and grain boundary sliding have been attributed to fracture at such temperatures [52]. More intense dislocation activity or dislocation pile-up was also observed close to the grain boundaries at high temperatures using TEM [97,98]. This leads to localized deformation at the grain boundaries along with cavitation.

The three main mechanisms of fracture which may take place independently or as a combination depend on the material and testing conditions:

Cleavage fracture

Cleavage fracture can be defined as the rapid propagation of crack along a particular crystallographic plane [99]. Cleavage usually takes place at low temperatures, mostly below RT. Cleavage fracture surfaces are marked by steps or ridges with flat surfaces. Typical cleavage planes for BCC materials are the (100) planes.

Cleavage fracture is a form of transgranular fracture. It is usually initiated by second phase particles or sharp microcracks already existing in the microstructure [100]. After this, the crack propagates along

the (100) cleavage plane and reaches the grain boundary. Hereafter, the crack crosses over the grain boundary and continues to propagate on the (100) cleavage plane of the next grain [95].

Ductile fracture

Ductile fracture is marked by dimples and takes place due to the nucleation, growth and coalescence of voids at slightly higher temperatures as compared with cleavage fracture. Nucleation of such voids takes place on the second phase particles. Dimples on the fracture surfaces are the traces of the voids formed at second phase particles. Ductile fracture might also arise through the microcracks or pores already existing in the microstructure [42]. It is the most common fracture mechanism for metals above RT. Ductile fracture may propagate sometimes through grains (transgranular) and sometimes along grain boundaries (intergranular) depending on where the void initiating particles are located. Crack propagation through ductile fracture is usually slower than cleavage fracture.

Void nucleation may take place by particle-matrix debonding (in soft matrix) or particle cracking (in hard matrix). After this, the void grows, usually in the direction of tension and also grows laterally due to constraint induced stresses. Void coalescence may arise by internal necking, internal shearing or by necklace formation [95] which leads to crack propagation.

Intergranular fracture

This kind of fracture is usually associated with weak grain boundaries resulting in a brittle form of fracture with the crack propagating rapidly along the grain boundaries. Weak grain boundaries could exist at low temperatures due to segregation of impurities at the grain boundaries and can also exist at high temperatures due to higher dislocation activity at weakened grain boundaries [52]. The appearance of intergranular fracture depends on the condition of grain boundaries through which the crack propagates. It can have a faceted appearance in case of equiaxed grains or a flat appearance in case of elongated grains.

2.3.2 Fracture toughness

Fracture toughness of a material is an indication of the amount of stress or energy required to propagate a pre-existing flaw in it. It is an important material property since the occurrence of flaws is inevitable in the processing, fabrication, or service of a material/component. Flaws together with the fracture toughness of a material and the applied stress constitute the fracture mechanics approach to structural design and material selection.

In linear elastic materials, crack extension happens when energy available for crack growth exceeds G_C, the critical energy release rate value. In terms of stress intensity, crack extension takes place when K_I, the stress intensity factor at the crack tip which is dependent on the applied stress and the size of the crack, exceeds K_{IC}, the mode I critical stress intensity value, which is a material parameter. G_C and K_{IC} both represent the fracture toughness of a material. In elastic-plastic materials, the fracture toughness can be represented by the critical energy release rate J_{IC} value [99]. This can be converted to the

corresponding stress intensity K_{JIC} value, another measure of fracture toughness, using the following relation:

$$K_{JIC} = \sqrt{\frac{E\, J_{IC}}{1-\vartheta^2}} \tag{2}$$

where:

ϑ = Poisson's ratio

E = Elastic Modulus

Crack growth resistance curves or J-R curves are a measure of crack resistance of a material. It plots the energy needed for crack growth (G or J) versus the crack growth (Δa). A fully brittle material has a flat J-R curve while ductile fracture in metals usually results in a rising J-R curve. Here, the driving force must increase to maintain the crack growth. A typical J-R curve can be seen in Fig. 10. There are three stages of crack propagation in an elastic-plastic material. In the first stage, the crack blunts resulting in a steep J-R curve. In the second stage, crack growth takes place and the J-R curve is shallower than in the first region. The third stage is flat and marked by a steady state crack growth. This stage, however, is not reached in laboratory tests on ductile materials as the plastic zone is not small enough as compared to the specimen dimensions. The fracture toughness value usually refers to the crack initiation point at the second stage. It is usually impossible to determine the exact crack initiation point in most materials. Hence, an engineering definition of crack initiation, analogous to the 0.2% yield strength in tensile tests, is usually deployed [99]. In the test standard ASTM E1820, an offset line with a slope 2 times the effective yield strength (mean of yield stress and ultimate tensile stress) to exclude crack blunting and with an 0.2 mm offset is drawn to intersect the J-R curve (Fig. 10). The intersection point is called the J_Q or the interim fracture toughness value. J_Q becomes J_{IC} , the mode I fracture toughness value, when all the validity criteria in the test standard ASTM 1820 [101] are fulfilled. The slope of the J-R curve at a given crack extension, gives an indication about the relative stability of the crack growth. A material with a steep J-R curve is less likely to experience unstable crack propagation. The slope can be quantified by the tearing modulus T:

$$T = \frac{E}{\sigma_{YS}^2} * \frac{dJ}{da} \tag{3}$$

where:

σ_{YS} = Yield stress

a = crack length

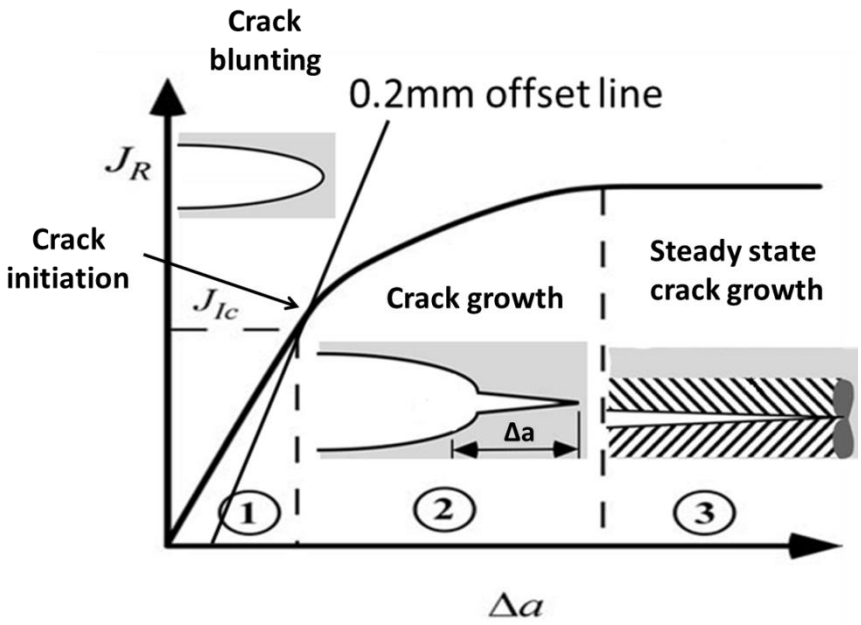

Fig. 10 A typical J-R curve for an elastic-plastic material showing three stages of crack propagation [99].

Unloading compliance test

The basic test method requires loading multiple specimens to different crack lengths in order to obtain J-R curves. Therefore, testing methods such as unloading compliance [101,102], normalization [101,103] and potential drop [104] were developed which require only a single specimen. In this research, only the unloading compliance method was used on the compact tension (C(T)) specimens.

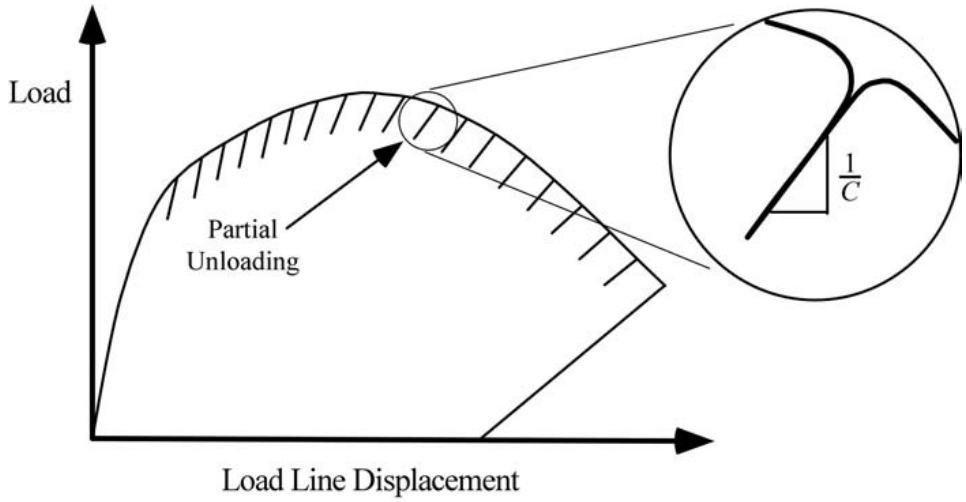

Fig. 11 Load-displacement graph from a typical unloading compliance test showing partial unloadings which are used to calculate the compliance at each crack growth step [99].

Computation of the J-R curve requires crack growth monitoring of the fracture specimen along with the J values at each crack length. In the unloading compliance method, the specimen is loaded and unloaded at equal displacement intervals and a load-displacement curve is obtained. The crack length at each interval is calculated using the measured compliance at the partial unloadings (Fig. 11). ASTM 1820 [101] provides polynomial expressions for conversion of compliance to crack length.

The J value is calculated using the addition of the elastic part, which is dependent on the instantaneous crack length and the plastic part, which is dependent on the area under the load displacement curve and the instantaneous crack length. The expressions for this calculation are presented below and also mentioned in ASTM 1820 [101]. Once the J versus crack growth graph is plotted, the fracture toughness value is obtained as described previously.

$$J_i = J_{el(i)} + J_{pl(i)} \tag{4}$$

$$J_{el(i)} = \frac{K_{(i)}^2\,(1-\vartheta^2)}{E} \tag{5}$$

$$K_{(i)} = \frac{P_{(i)}}{(BB_N w)^{1/2}} f\left(\frac{a_i}{w}\right) \tag{6}$$

$$f\left(\frac{a_i}{w}\right) = \frac{\left\{\left(2+\frac{a_i}{w}\right)\left[0.886 + 4.64\left(\frac{a_i}{w}\right) - 13.32\left(\frac{a_i}{w}\right)^2 + 14.72\left(\frac{a_i}{w}\right)^3 - 5.6\left(\frac{a_i}{w}\right)^4\right]\right\}}{\left(1-\frac{a_i}{w}\right)^{3/2}} \tag{7}$$

$$J_{pl(i)} = \left[J_{pl(i-1)} + \left(\frac{\eta_{pl(i-1)}}{b_{(i-1)}}\right)\frac{A_{pl(i)} - A_{pl(i-1)}}{B_N}\right]\left[1 - \gamma_{(i-1)}\left(\frac{a_{(i)} - a_{(i-1)}}{b_{(i-1)}}\right)\right] \tag{8}$$

where:

$$\eta_{pl(i-1)} = 2.0 + \frac{0.522 b_{(i-1)}}{w} \tag{9}$$

and

$$\gamma_{(i-1)} = 1.0 + \frac{0.76 b_{(i-1)}}{w} \tag{10}$$

J_i = Instantaneous J-integral

$J_{el(i)}$ = Instantaneous elastic component of J-integral

$J_{pl(i)}$ = Instantaneous plastic component of J-integral

K_i = Instantaneous stress intensity factor

$P_{(i)}$ = Instantaneous load

B = Thickness of the C(T) specimen

B_N = Net specimen thickness (after side-grooving)

w = Width of the C(T) specimen

a_i = Instantaneous crack length

b_i = Instantaneous ligament length

$A_{pl(i)}$ = Instantaneous area under the load displacement curve

Specimen thickness (B)

The size and shape of the cracked specimen should ideally have no influence on the shape of the J-R curve. However, thickness, in relation to other dimensions, plays a role in providing plane strain or plane stress conditions for the crack to grow. It becomes particularly important in case of small specimens where the thicknesses are quite small.

In a thick sample, due to high stresses near the crack front, the crack-tip material tries to contract but is resisted by the material surrounding it. This constraint causes a constraint induced stress state near the crack-tip which varies from the middle of the crack front to the sample surface as shown in Fig. 12. The high constraint induced stress (σ_{zz}) in the middle of the crack front is known as "Plane strain state" and results in high stresses in the thickness direction. At regions near the sample surface or in thin samples, "Plane stress state" exists where the stress in the thickness direction σ_{zz} is lower. The constraint induced stress state also results in higher stresses in the plastic zone (σ_{yy}). Crack tunnelling can happen where crack propagates more towards the middle of the crack front than the edges. This is usually mitigated by side grooving the fracture specimen [99].

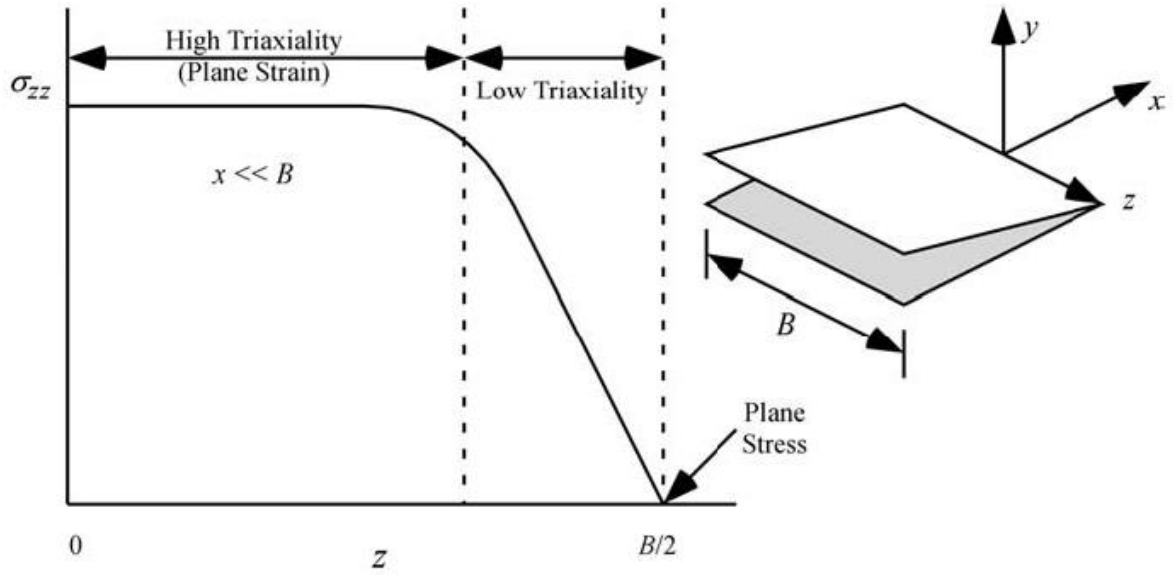

Fig. 12 Variation of constraint induced stress (σ_{zz}) through the thickness at a point near the crack tip [99].

The plastic zone for small specimen should be such that it does not exceed the thickness of the specimen. For this, a validity criterion is devised which ensures that plane strain condition is followed along the crack front:

$$B \geq 2.5 \left(\frac{K_{JIc}}{\sigma_{YS}}\right)^2 \quad (11)$$

2.4 Summary

ODS steels were developed for application in fusion and fission environments consisting of high neutron irradiation and high temperature. They are typically manufactured through powder metallurgy followed by canning, degassing, HIP and post processing methods such as hot-extrusion and hot-rolling. Alternate methods of fabricating ODS steels such as SPS, additive manufacturing, controlled oxidation and liquid metal processing work towards increasing scalability and decreasing time scales and costs.

ODS steels, due to the presence of high number density of Y, Ti and O-enriched nano-particles, exhibit high strength at a temperature range of 650 to 900 ˚C, possess high temperature creep resistance and exhibit high resistance against irradiation induced swelling and embrittlement. They possess bimodal grains and are often found to be elongated towards rolling/extrusion direction. The α fibre texture was predominantly found in hot-rolled sheets while a texture with grains oriented in the <110> direction parallel to the extrusion direction was found in hot-extruded material.

Many ODS steels possess acceptable fracture toughness and yield strength in the temperature range of RT to 300 ˚C. This number reduces drastically for the temperature range of 500 - 600 ˚C. TMT, cryomilling and other methods have partially been successful in improving fracture toughness in the temperature range of 500 - 600 ˚C. However, the exact microstructural features which affect the fracture toughness of ODS steels at a specific temperature range have not yet been fully explored. One of the aims of this research is to do that.

ODS steels exhibit fracture toughness anisotropy with hot-extruded materials possessing better fracture properties than hot-rolled materials. The explanation for the anisotropic fracture behaviour has been a point of debate with some suggesting segregation of carbides and oxides at the grain boundaries while others suggesting debonding of oxide coated aggregate of grains as the primary reason. This research targets this question and throws more light on the microstructural features which lead to fracture toughness anisotropy.

Secondary cracks are formed due to constraint induced stress and are often observed on the fracture surfaces of ODS materials close to RT in certain orientations. They may appear due to delamination in certain orientations such as “crack-divider” but don’t appear in the “crack-arrester” geometries. Secondary cracks can result in increased energy absorption, can be beneficial for preventing primary cleavage fracture and also for stabilization of primary cracks but they appear at lower loads than primary cracks. They are facilitated due to the {100} cleavage planes in hot-rolled materials at low temperatures. In general, weak planes have been reported to be the primary cause for secondary cracks; however the source of weak planes remains a point of debate. This research throws more light on this

by linking the microstructure and specimen orientation with the extent of secondary cracking. The reasons why hot-rolled materials are more prone to secondary cracking than hot-extruded materials are also discussed. The various fracture mechanisms of secondary cracking at different temperatures are still not very clear and are amply elaborated through this research.

3 Experimental work

3.1 Material

The 13 wt. % Cr ODS steels were provided by Karlsruhe Institute of Technology, Germany (KIT) in hot-extruded rod and hot-rolled plate forms. The nominal composition of the material was 13Cr1W0.3Ti0.3Y_2O_3 (in wt. %) and the bulk chemical composition can be found in Table 2. Fe_3Y intermetallic powder was added before mechanical alloying to reach 0.3 wt. % Y_2O_3. The main manufacturing steps for hot-extruded rod were the following: mechanical alloying of the steel alloy and intermetallic powder in an attritor ball mill, encapsulation of the powder, evacuation of the capsule and hot-extrusion at 1100 °C. The as-milled powders contained about 0.09 wt. % oxygen. The reduction of 80 mm initial diameter to a 12 mm final diameter rod resulted in a extrusion ratio of 44.4 [89]. The main production steps for manufacturing the hot-rolled plate were the following: mechanical alloying of the steel alloy and intermetallic powder in an attritor ball mill, encapsulation of the powder, evacuation of the capsule and hot isostatic pressing (HIP) at 1100 °C and 100 MPa and rolling at 1100 °C from an initial diameter of 80 mm to a plate of 7 mm thickness in 8 runs. Details of the production method for both the batches can be found in reference [89].

The hot-extruded 14 wt. % Cr ODS steel rod of 16 mm diameter was provided by Centro Sviluppo Materiali, Italy (CSM). The bulk chemical composition can be found in Table 2. This material was manufactured by the following steps: Gas atomized pre-alloyed steel matrix was added with 0.3 wt. % Y_2O_3 and dry ball milled in an environment of Ar and H. The as-milled powders contained about 0.22 wt. % oxygen. After canning, direct hot-extrusion was performed at 1150 ˚C with an extrusion ratio of 22.5. Heat treatment was performed thereafter at 1050 °C for one hour and then cooled in the furnace. The final rod had 1 mm outer layer of AISI 316 stainless steel, which came from canning. This outer part was excluded while machining out the mechanical testing samples.

For simplification, the terms ODS-KIT HR, ODS-KIT HE and ODS-CSM will be used throughout the thesis to represent hot-rolled 13Cr ODS steel from KIT, hot-extruded 13Cr ODS steel from KIT and hot-extruded 14Cr ODS steel from CSM, respectively. The term ODS-KIT is also sometime used to represent both ODS-KIT HR and ODS-KIT HE together. The bulk chemical composition of the materials, presented in Table 2, was obtained using optical emission spectrometry (Thermo Scientific ARL 8860) from BGH Edelstahl Freital GmbH, Germany. A flowchart of the manufacturing process deployed for the three investigated materials in this research is shown in Fig. 13.

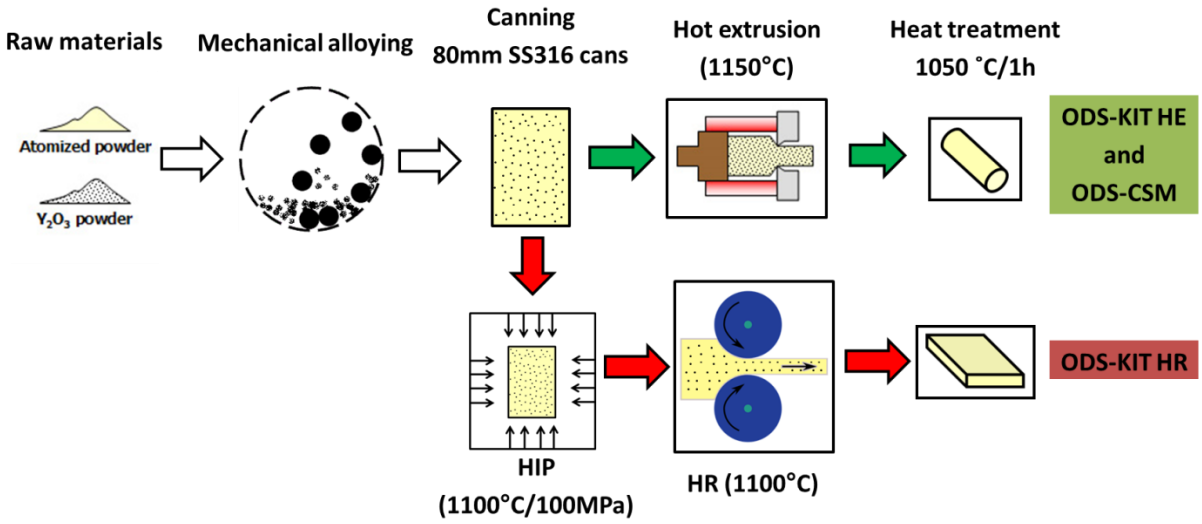

Fig. 13 Flowchart of the manufacturing processes used to manufacture the three investigated ODS steels.

Table 2 Bulk chemical composition of the investigated ODS alloys (wt.%).

Elements	ODS-KIT	ODS-CSM
Fe	85.28	83.84
Cr	12.99	13.76
W	1.03	0.842
V	0.007	0.012
Ti	0.138	0.238
Si	0.051	0.371
Al	0.009	0.027
Ni	0.101	0.239
Cu	0.017	0.012
Mn	0.088	0.056
Zr	0.037	0.047
P	0.01	0.006
N	0.009	0.166
C	0.028	0.01
Y	0.165	0.279

3.2 Methods

3.2.1 Tensile tests

Tensile tests for ODS-KIT HE (three tests at each temperature) and ODS-CSM (one test at each temperature) were performed using miniature flat tensile test specimens with their gauge length parallel to the extrusion direction. The cross-section of the samples was 1 mm x 2 mm with an overall length of 20 mm. Tests were carried out at temperatures varying from 20 ˚C to 700 ˚C. The tests were performed in air with a crosshead speed of 0.1 mm/min.

The tensile tests for ODS-KIT HR were performed at Karlsruhe Institute of Technology, Germany. Miniature cylindrical tensile test specimens, with gauge length parallel to rolling direction, were tested at temperatures varying from 20 ˚C to 700 ˚C. The gauge length and diameter were 7 mm and 2 mm, respectively. The tests were performed in air with a test velocity of 0.1 mm/min.

3.2.2 Fracture toughness tests

Fracture toughness specimens

Fracture toughness tests were performed to obtain fracture toughness, J-R curves, load versus displacement curves and crack growth versus load line displacement curves. The ASTM notation suggests two letters for the identification of the orientation of a fracture toughness testing specimen; the first letter indicates the direction of principal tensile stress, which is perpendicular to the crack plane in Mode I tests, and the second letter denotes the direction of crack propagation.

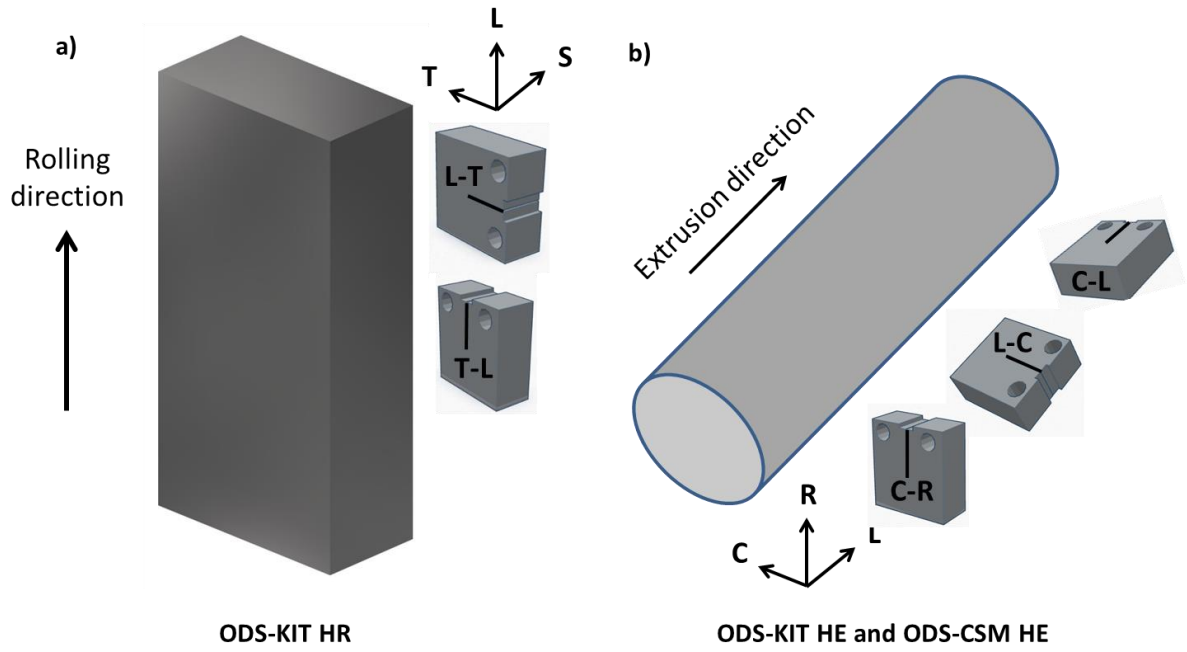

Fig. 14 Cutting scheme of a) ODS-KIT HR and b) ODS-KIT HE and ODS-CSM.

Miniature compact tension C(T) specimens of 4 mm thickness (0.16T) were machined in three orientations (L-C, C-R and C-L) from a 12 mm diameter rod of ODS-KIT HE and from a 15 mm diameter rod of ODS-CSM. Miniature compact tension C(T) specimens of 6.35 mm thickness (0.25T) were machined from the 8 mm thick plate of ODS-KIT HR in two orientations, L-T and T-L. The cutting schemes of the specimens in different orientations can be seen in Fig. 14.

All the C(T) specimens were 20% side grooved and fatigue pre-cracked at RT (ODS-CSM) and 200 ˚C (ODS-KIT) to a crack length to width ratio (a/w) of 0.5 using a resonance testing machine. The nominal cyclic stress intensity at the end of the fatigue pre-cracking stage (K_{end}) was 14 MPa$\sqrt{m}$.

Quasi-static fracture toughness testing

Quasi-static fracture toughness tests were carried out on small size C(T) specimens using the unloading compliance method [102]. The unloadings were carried out with a 25% load drop and a 30 s relaxation time. Single tests were performed in air for ODS-KIT HE and two tests were performed in air for ODS-CSM, at temperatures of 22, 200, 400, 600 ˚C. For ODS-KIT HR, the same test plan as ODS-KIT HE was adopted with additional single tests at -100 ˚C, 100 ˚C, 500 ˚C and 700 ˚C. The crosshead speed of the machine was 0.1 mm per minute with unloading steps of 0.015 mm. The tests were stopped after approximately 1 mm crack propagation and thereafter the specimens were heat tinted in order to mark the crack growth region. Heat tinting was not required for specimens tested at and above 400 ˚C. The initial and the final primary crack lengths were measured on the fracture surfaces using optical microscope according to the nine point standard ASTM method [101]. For the 0.16T specimens, the crack opening displacement (COD) measurements were done on the load line using a contact clip on gauge in the temperature range from RT to 200 ˚C. From 200 ˚C to 600 ˚C, a contactless video extensometer was used at the front face. For 0.25T specimens, front face displacement measurement using a contactless video extensometer was used at all temperatures. For all the front face displacement measurements, the compliance and displacement values had to be converted to the load line values [105] as explained below. Thereafter, the evaluation was performed according to ASTM E1820-13 [101].

Front face correction

ASTM E1820 usually refers to the standard sized C(T) specimens [101]. For small specimen testing, which are commonly deployed for ODS materials owing to their limited availability, certain modifications in the testing setup are necessary, e.g., for front face crack opening displacement measurement. The front face displacement is converted back to the load line displacement using certain geometrical relations as described below [105,106]:

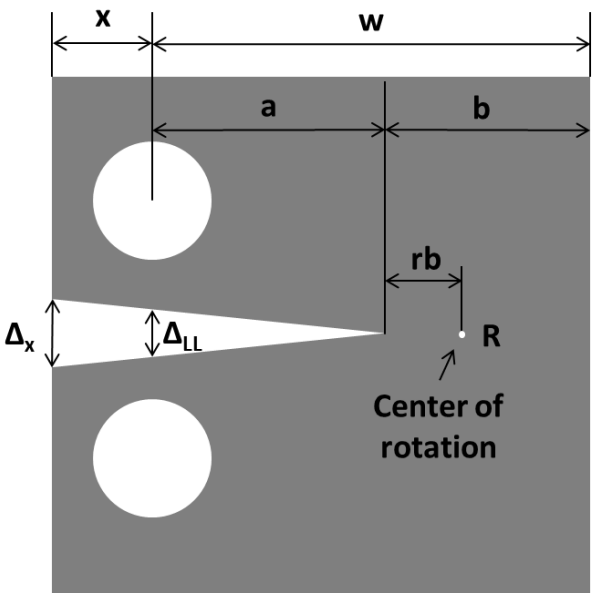

Fig. 15 Schematic of a typical C(T) specimen showing important dimensions.

$$\Delta_{LL} = \frac{(a + r * b) * \Delta_x}{a + r * b + x} \tag{12}$$

where:

a = Crack length

b = Ligament length

w = Width of the C(T) specimen

Δ_{LL} = Load line displacement

x = Distance of the measuring point from the load line

Δ_x = Shifted measuring point displacement

r = Rotation factor

The rotation factor (r) of a C(T) specimen is a factor which is used to determine the rotation point R (Fig. 15), about which the C(T) specimen rotates during crack propagation and can be found using the following relation:

$$r = \frac{0.13 * \Delta_{elastic} + 0.43 * \Delta_{plastic}}{\Delta_x} \tag{13}$$

$\Delta_{elastic}$ and $\Delta_{plastic}$ are displacements in the elastic and plastic regimes, respectively and can be determined using the compliance (C), load (P) and displacement at the shifted measuring location (Δ_x) using:

$$\Delta_{elastic} = P * C \quad (14)$$

$$\Delta_{plastic} = \Delta_x - \Delta_{elastic} \quad (15)$$

The compliance from the front face measured during testing also has to be converted into load line compliance using [105]:

$$C_{LL} = \frac{A * C_x}{A + \frac{x}{w}} \quad (16)$$

where:

$$A = \left(1.07 + 0.976 * \frac{x}{w}\right) * \frac{a}{w} + \left(0.35 - 4.056 * \frac{x}{w}\right) * \left(\frac{a}{w}\right)^2 - \left(2.874 - 8.981 * \frac{x}{w}\right) * \left(\frac{a}{w}\right)^3 + \left(4.99 - 10.23 * \frac{x}{w}\right) * \left(\frac{a}{w}\right)^4 - \left(2.547 - 4.318 * \frac{x}{w}\right) * \left(\frac{a}{w}\right)^5 \quad (17)$$

C_x = Compliance at the shifted measuring point

C_{LL} = Compliance at the load line

Once the instantaneous load line compliance is known, the crack length estimation is performed at each step in a standard way. The J-R curves are plotted after the instantaneous J-integral values and crack lengths are calculated at each step using both the shifted load line compliance and shifted load line displacement values.

3.2.3 Stereo optical microscopy

Most of the C(T) specimens were broken apart after fracture toughness testing. Stereoscopic microscope imaging was done on all fracture surfaces for macroscopic images. The crack growth region after heat tinting was clearly distinguishable (coloured) from the rest of the fracture regions. It was also used to image the polished fracture surface after the interrupted fracture toughness test (described later).

3.2.4 Optical microscopy

Optical microscopy (Leica REICHERT MEF4) was used to investigate primary crack propagation by polishing and etching side surfaces of the C(T) specimens. It was also performed on polished planes of tested C(T) specimens perpendicular to secondary crack planes in order to measure secondary crack depths.

3.2.5 Scanning electron microscopy

The scanning electron microscope (SEM) produces images by scanning the sample with a high-energy beam of electrons emitted from a tungsten filament. As the electrons interact with the sample, they

produce secondary electrons, backscattered electrons and characteristic X-rays. These signals are collected by one or more detectors to form images which are then displayed on the computer screen. The secondary electrons are low energy electrons which are emitted from the sample surface giving topographical information about the sample.

Backscattered electrons are higher energy electrons that are elastically backscattered by the atoms of the sample. This mode can be used to detect compositional contrast in the sample. It is also able to detect small amounts of grain contrast in polished and etched samples.

Energy dispersive X-ray spectroscopy (EDX) is used to determine the chemical elements present in a sample, and can be used to estimate their relative abundance. This is done by detecting the characteristic X-rays emitted from a specimen.

Basic microstructure

Bulk samples were polished using a polycrystalline diamond solution down to 1 µm and then etched (50 ml distilled water, 15 ml hydrochloric acid, 2.5 g iron (III) chloride). Scanning electron microscopy was performed (Zeiss EVO 50) on etched bulk samples using an accelerating voltage of 15 kV, a filament current of 2.6 A, a probe current of 200 pA and a working distance of 11 mm at various magnifications ranging from 50X to 10000X to locate the sub-micron particles. Due to the limit in the spatial resolution of the SEM, the particles in the size range of 50 nm to 1000 nm were easily resolvable. Detection of particle with size lower than 50 nm was not easy using the SEM. Energy dispersive X-ray spectroscopy (EDS) was performed on etched samples using a higher spot size (probe current: 1000 pA) with a working distance of 18 mm to chemically identify sub-micron particles and inclusions. The backscatter mode in SEM was used on the oxide polishing suspension (OP-S) (amorphous silica, water and1,3 butanediol) polished samples to observe grain contrast together with sub-micron particle locations. Most particles however, fell out of the sample during OP-S polishing and holes of similar sizes were left behind.

Fractography

Most of the C(T) specimens were broken apart after fracture toughness testing. SEM was performed on all the primary fracture surfaces for higher magnification images. Some selected C(T) specimens were not broken apart after fracture toughness testing. The side surfaces of these C(T) specimen containing the propagated primary crack were investigated using SEM. Some of these specimens were also polished down inwards from the side surface and then etched.

The secondary cracks observed sometimes on the primary fracture surface, were opened up from a broken C(T) specimen after the test by selective machining as shown in the schematic (Fig. 16). SEM was used to examine the secondary fracture surface thereafter.

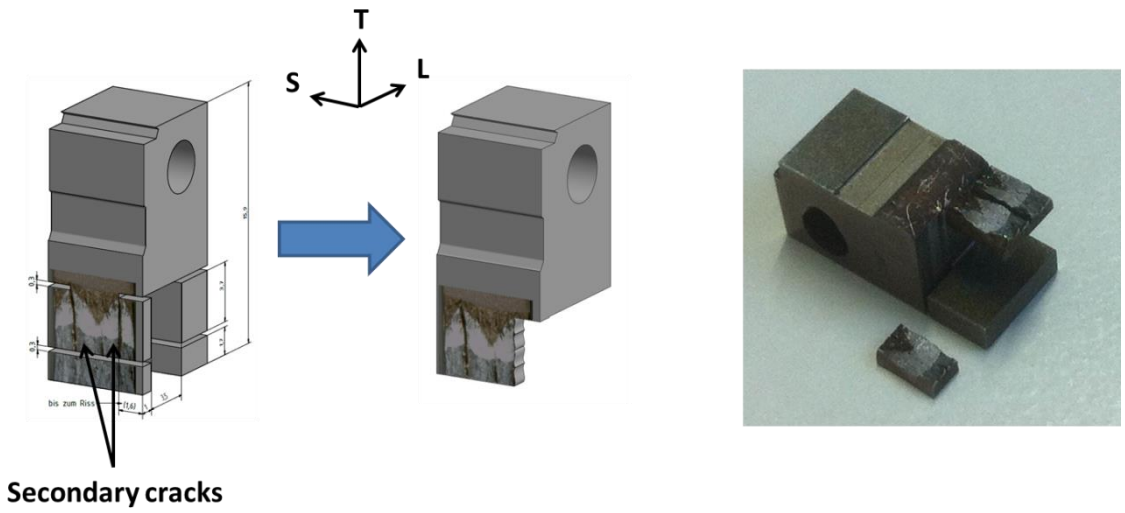

Fig. 16 Schematic showing the cutting scheme for opening of secondary crack fracture surfaces.

3.2.6 Electron backscatter diffraction microscopy

Electron backscatter diffraction (EBSD) is a valuable tool for the analysis of crystalline materials. Information such as local crystallographic orientation, grain distribution and morphology can be obtained using EBSD. The electron beam from the filament of the SEM strikes the specimen at a highly tilted angle to the diffraction camera. The electrons enter the sample and backscatter to exit at the Bragg condition related to the spacing of the lattice planes in the crystalline structure producing a diffraction pattern on the phosphor screen. A high sensitivity, low-light level CCD camera is used to view the phosphor and to capture an image of the electron backscatter pattern which consists of Kikuchi bands [107].

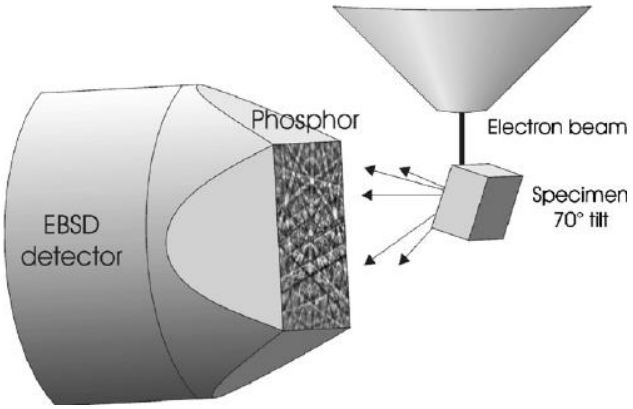

Fig. 17 Schematic of the EBSD setup [107].

This characteristic Kikuchi bands give information about the orientation of the measurement point which is then converted into one colour coded pixel in the inverse pole figure map (IPF map). The IPF maps make the connection between the reference macroscopic coordinate system and the crystallographic coordinate system using a specific colour key. The IPF Z map of a sample plane for example, shows the orientation of grains in the crystallographic coordinate system which have the normal of their planes parallel to the macroscopic Z direction. Additionally, pole figures and inverse pole figures

(IPFs) can be generated. Pole figures show how specific crystallographic directions of each grain are distributed in the sample reference system and IPFs show how a selected direction in the sample reference system is distributed in the crystal reference system. The orientation distribution function (ODF) is a two-dimensional plot of the three dimensional Euler space (using Euler angles φ_1, φ and φ_2) where orientation of each pixel can be described. It is also an effective tool to describe texture in a material.

Grain distribution maps consisting of random coloured grains can be obtained by defining the misorientation angle threshold, which defines a grain boundary. This can be achieved in the post-processing mode of the EBSD software (ESPRIT 2.1). All the grains above this threshold are considered as high-angle grain boundaries (HAGBs) and all the grains below the threshold limit are considered as low-angle grain boundaries (LAGBs). LAGBs are not displayed in the grain distribution map however; they are displayed in the quality map which displays them together with HAGBs as black lines as these areas possess extremely low diffraction quality (the same happens also for pre-existing pores and cracks). The grain aspect ratio (GAR) gives the ratio of the planar dimensions of an elongated grain. A high GAR value indicates high amount of grain elongation. This, along with equivalent circular diameters (diameter of a circle with the same area as the grains) can be found in the grain size distribution list which can be used to make grain size distribution graphs. The lower the step size, the higher the pixel resolution and the higher the exposure time, the greater is the quality of mapping. However, due to time constraints, a compromise is made where an optimum combination of these parameters are chosen. In case of bimodal grain distribution, which is often found in ODS steels, the mean grain size of ultra-fine grains (UFGs) is determined by separate mapping using small step sizes for higher resolution. Due to the limits in spatial resolution of the SEM, nano-grains are hard to map.

Basic Microstructure

Electron backscatter diffraction (EBSD) was performed on the OP-S polished samples to obtain information about crystallographic texture and grain distribution. An accelerating voltage of 20 kV and a working distance of 18 mm were used. The image resolution was fixed at 800 x 600 as a trade-off between total image acquisition time and a sufficiently high degree of detail. The step size of 0.19 µm was chosen for a large field of view to obtain a statistically large ensemble of grains. Inverse pole figure Z maps (IPF maps), Inverse pole figures (IPFs) and orientation distribution functions (ODFs) were acquired from different planes to describe the crystallographic orientation of the microstructure. The IPFs are convoluted i.e. point densities are taken into account using a Gaussian function defined by its Full Width Half Maximum (FWHM). This is represented by higher intensity in the IPF for higher level of texture. Grain distribution maps were extracted to describe the size, morphology and alignment of grains in the microstructure. Noting that the materials are ferritic and that high-angle boundaries (as opposed to low-angle boundaries) generally play a dominant role in fracture [108], this study is focussed on high-angle boundaries and the minimum misorientation angle for the EBSD analysis was arbitrarily fixed at 10°.

Fractography

Some selected C(T) specimens were not broken apart after fracture toughness testing. The side surfaces of the C(T) specimen containing the propagated primary crack were OP-S polished and then EBSD was performed to obtain information about primary crack propagation with respect to the grain arrangement and morphology. A step size of 48 nm was used to obtain high magnification images of the propagating crack.

In some cases, secondary cracks were observed on the primary crack plane. EBSD misorientation (MO) line scan analysis was performed across such a secondary crack on subsequently polished planes either parallel or perpendicular to the primary crack plane in order to understand the fracture mechanisms. Here the IPF X, Y and Z maps, which belong to the same secondary crack, were taken into consideration to obtain the complete information about the three dimensional grain orientations on both sides of the crack. It is possible to perform the misorientation line scan with respect to the immediately previous point or with respect to the first measurement point. It was however, decided to perform the line scan using the former as the latter does not give the misorientation of a grain relative to the immediately previous grain, which is what is required. The misorientation line scan exhibits sharp peaks when the orientation changes between two sequential points. The magnitude of the peaks is the misorientation between two grains or across the crack.

3.2.7 Transmission electron microscopy

The transmission electron microscope (TEM) uses a beam of electrons, which are transmitted through a thin sample (100 nm), to form an image. Owing to the small de Broglie wavelength of electrons, the TEM has much higher magnification than light microscopes.

In the bright-field mode of operation in the TEM, the areas with higher atomic numbers block more electrons and appear dark in the image while low atomic number regions appear bright. In diffraction contrast, grains and particles which satisfy the Bragg's condition are displayed brightly. This is also known as dark-field imaging. The TEM can also work in a scanning mode which is called the scanning transmission electron microscope (STEM).

Basic Microstructure

TEM investigations were performed using a Talos F200X FEG-(S)TEM (FEI) operated at 200 keV to detect particles which were smaller than the spatial resolution of the SEM (< 50 nm) and also to obtain high resolution images of the grains and larger particles. Samples were prepared by means of electropolishing in a TenuPol-5 in 5% perchloric acid in methanol at -60°C employing a voltage of 23 V. Bright field imaging and low magnification STEM imaging techniques with a HAADF detector were performed to characterize the sub-micron particles and nano-particles in terms of size and spatial distribution. Information on the composition of the particles was obtained by means of STEM-EDS mapping.

4 Results

This chapter begins with the characterization of the basic microstructure of all the three ODS steels. Subsequently, the mechanical properties of ODS steels are explored with respect to the tensile and fracture behaviour. The fracture behaviour of ODS steels is holistically represented by the results from the fracture toughness tests together with the fractography of the primary and secondary fracture surfaces. This is followed by the crack propagation analysis of the primary and secondary cracks using different microscopy techniques.

4.1 Basic characterization of the microstructure

The basic microstructure of all the ODS steels were investigated in different orientations using various microscopy techniques. Through this section, the following questions will be answered:

- What size and morphology do the grains possess and how are they distributed?
- Is there a difference in grain size and morphology in hot-rolled and hot-extruded materials?
- Is there a crystallographic texture?
- What kind of particles are in the microstructure?
- What is the size of the particles and how are they distributed?

4.1.1 ODS-KIT HR

Grains

A bimodal distribution of grains was found in all the ODS materials. Fine-grained zones typically alternate with coarse-grained zones. The coarse grains are arranged in zones which are elongated in the rolling and transverse directions. It is found using EBSD grain size distribution analysis, that the coarse grains are ‘pancake’-shaped and have maximum elongation towards the L direction followed by the T and S directions (Fig. 18). The fine grains are more or less equiaxed and appear to assemble themselves in fine-grained zones, similar to the coarse-grained zones (Table 3).

The grains were defined with a misorientation angle threshold of 10°, i.e. grains with high-angle grain boundaries (HAGBs) appear in different random colours. The low-angle grain boundaries (LAGBs) are also visible inside the HAGBs in the superimposed quality and grain distribution maps. A detailed statistical grain size analysis in terms of equivalent circular diameter (the diameter of a circle with the same area as the grains), grain aspect ratio (GAR) and area fraction is presented in Table 3 and Table 4 for fine and coarse grains, respectively. The GAR of the fine grains is lower than the coarse grains. The distinction between the fine and coarse grains was made at 3 µm for the TS and LS planes and at 10 µm for the LT plane based on the grain size distribution.

It is observed that {100} cleavage planes (depicted by red colour in the IPF map of the LT plane) arrange themselves parallel to the rolling plane (LT plane) and are directed towards the [110] direction

parallel to the rolling direction (depicted by yellow colour in the IPF map of the TS plane) as shown in Fig. 19. This same information is corroborated by the IPFs. The Z plot of the IPF of the TS plane in Fig. 19 shows a high intensity of [001] and [111] which means that many grains are aligned with the <100> and <111> directions parallel to the normal of the rolling plane (LT). This also means that {100} and {111} planes of the grains are parallel to the rolling plane. The X plot of the IPF shows a high intensity of [101], which means that a large number of grains are oriented with the <110> directions parallel to the rolling direction. The strong {100} <110>texture component is also confirmed by the ODF plot at the constant Euler angle φ_2 of 45˚ as shown in Fig. 19 [50].γ fibre {111} planes parallel to the rolling plane are also corroborated by the ODF. The fine and the coarse-grained regions both have similar texture as presented in Fig. 20, where IPF Z map of the TS plane is plotted for the fine and coarse grains separately.

Table 3 Grain size analysis for fine grains from all the materials.

Material	Plane	Equivalent grain diameter (µm)	GAR	Area fraction (%)
ODS-KIT HR	TS (0.3 - 3 µm)	1	2	20.4
ODS-KIT HR	LT (1.4 - 10 µm)	3	1.6	27.3
ODS-KIT HR	LS (0.4 - 3 µm)	1.1	2	17.6
ODS-KIT HE	T (0.2 - 3 µm)	0.78	1.7	68.9
ODS-KIT HE	L (0.2 - 3 µm)	0.9	1.7	39.4
ODS-CSM	T (0.25 – 1.5 µm)	0.65	1.43	46
ODS-CSM	L (0.25 – 1.5 µm)	0.75	2	35.4

Table 4 Grain size analysis for coarse grains from all the materials.

Material	Plane	Equivalent grain diameter (µm)	GAR	Area fraction (%)
ODS-KIT HR	TS (3 - 13 µm)	6	4	79.6
ODS-KIT HR	LT (10 - 91 µm)	21	3.3	72.7
ODS-KIT HR	LS (3 - 16 µm)	6	10	82.4
ODS-KIT HE	T (3 - 21 µm)	4.7	2.2	31.1
ODS-KIT HE	L (3 - 30 µm)	7.7	10	60.6
ODS-CSM	T (1.5 – 5 µm)	2.1	1.54	54
ODS-CSM	L (1.5 – 9.4 µm)	2.4	3.3	64.6

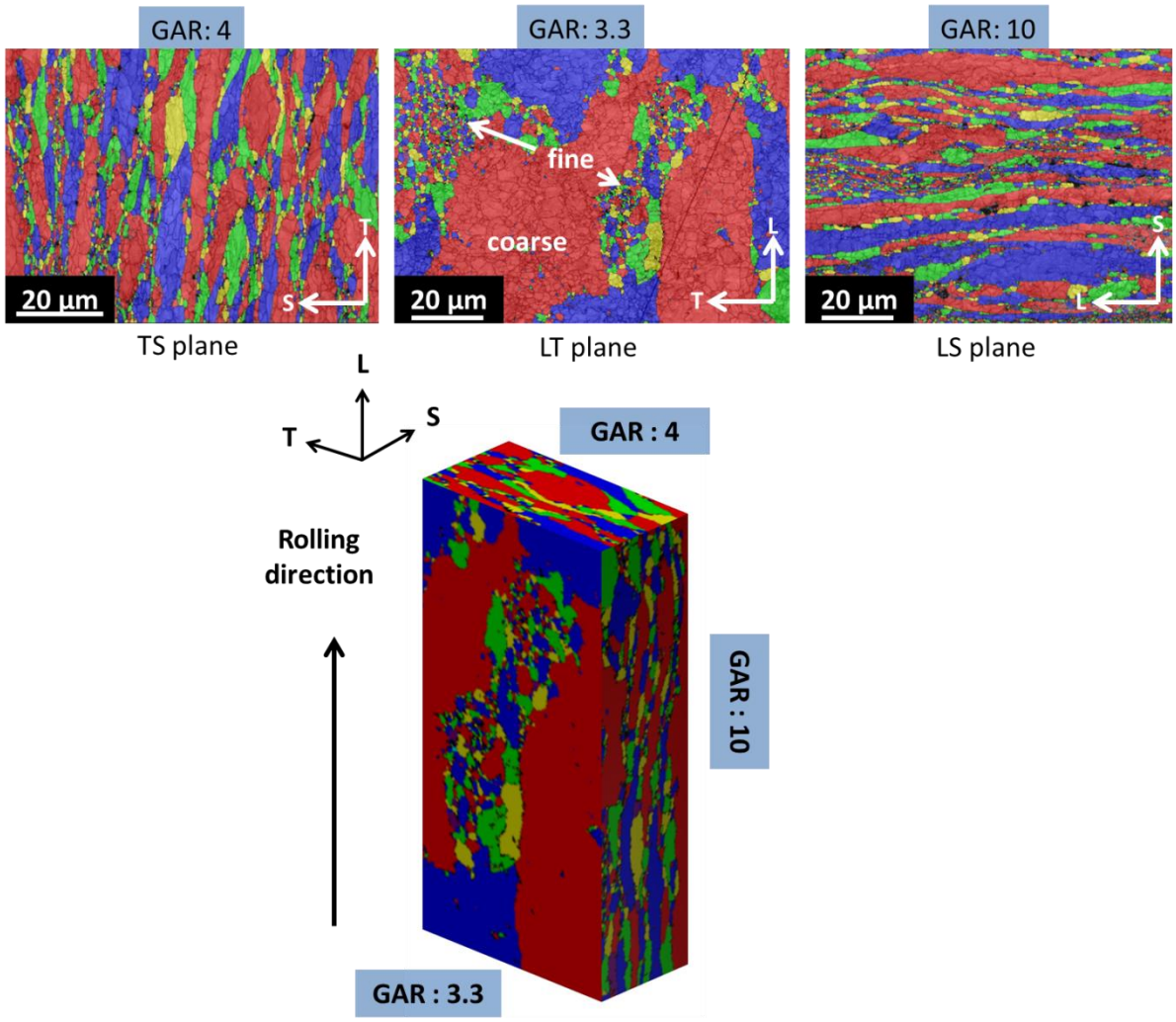

Fig. 18 Grain distribution map together with the superimposed quality map of TS, LT and LS planes in ODS-KIT HR (10° misorientation threshold angle). A schematic representation (below) of the hot-rolled material with 'pancake'-shaped elongated grains (not to scale). Indicated GAR values are for coarse grains.

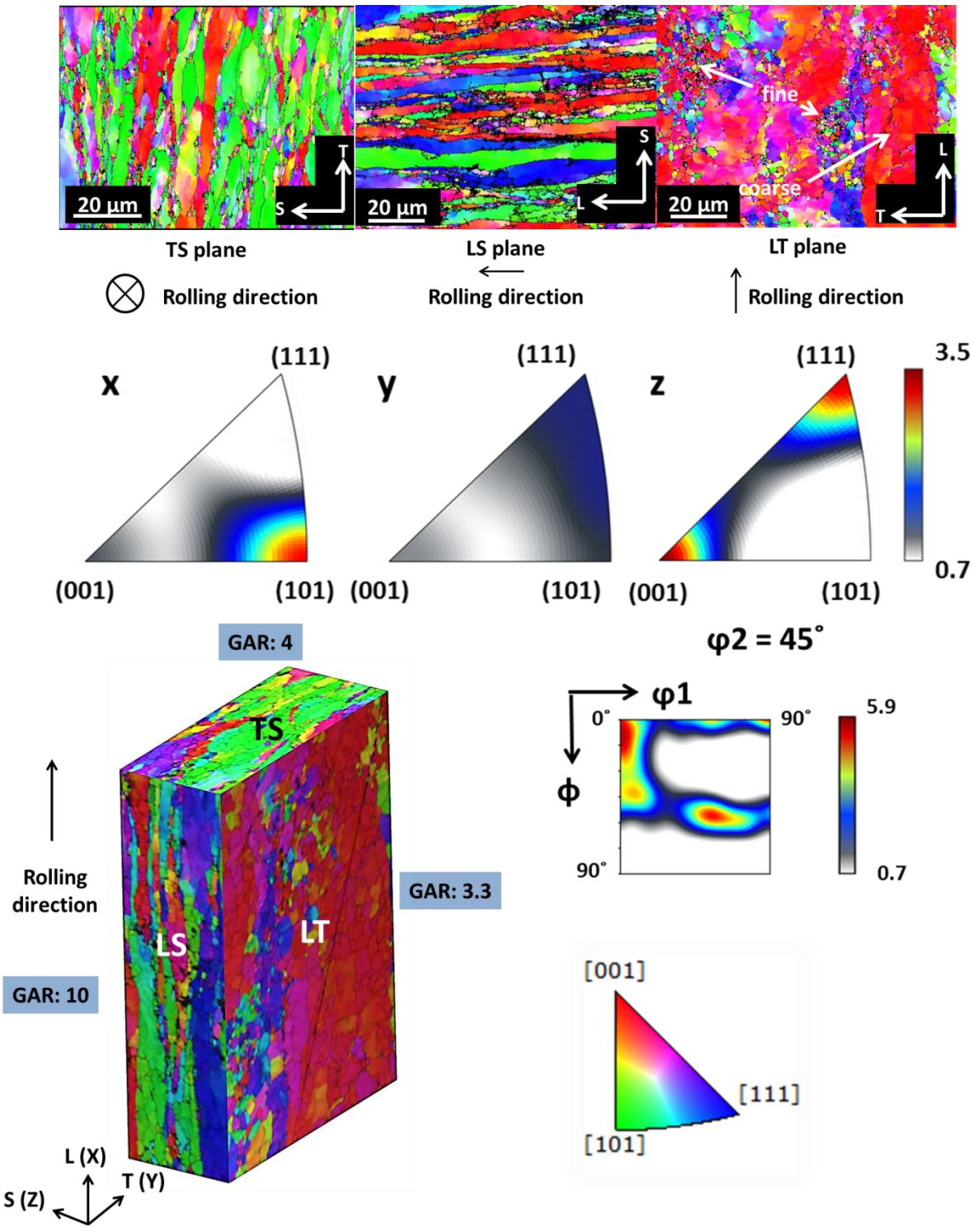

Fig. 19 Inverse pole figure Z maps in TS, LS and LT planes along with inverse pole figures (IPFs) in the TS plane and the ODF plot at $\phi 2 = 45^\circ$ (right bottom). A schematic representation (left bottom) of ODS-KIT HR with 'pancake'-shaped elongated grains (not to scale) is presented. Indicated GAR values are for coarse grains.

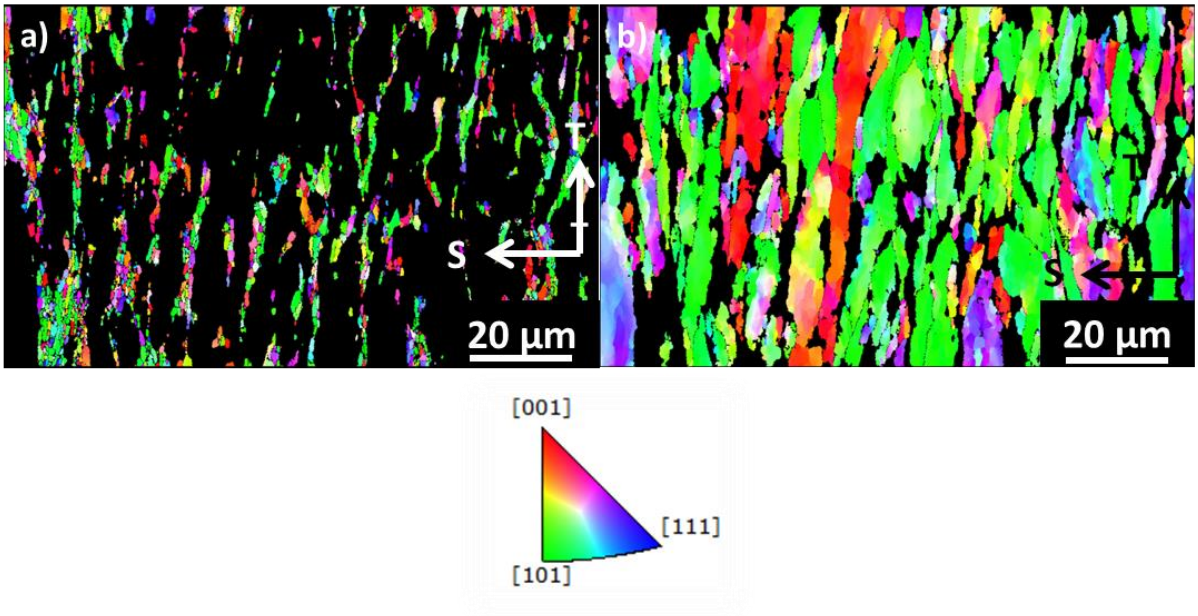

Fig. 20 Inverse pole figure Z map of ODS-KIT HR in the TS plane selectively highlighting a) fine and b) coarse grains

Particles

In this work, we distinguish sub-micron particles with sizes in the order of 50 nm up to 1 µm and nano-particles in the range of 2 nm up to 50 nm. Although the latter are characteristic particles of ODS steels, the sub-micron particles are more important from the viewpoint of fracture behaviour (elaborated in section 5.2.2).

The average nano-particle size is found to be 3.8 nm by TEM analysis (Fig. 21). The spatial distribution of the nano-particles is inhomogeneous with no visible preference to the grain boundaries. It was found using SEM-EDS on an etched sample, that the material contains zones of high and low number density of sub-micron Ti-enriched particles preferentially arranged in lines parallel to the rolling and transverse directions as can be seen from the backscattered SEM image in Fig. 22c and d and also from the SEM image in Fig. 22b. OP-S polishing used for backscattered imaging resulted in the fall out of the sub-micron particles leaving behind voids of similar size. Some pre-existing cracks are also observed elongated in the direction of rolling as shown by the SEM images of the etched sample in Fig. 22a and b.

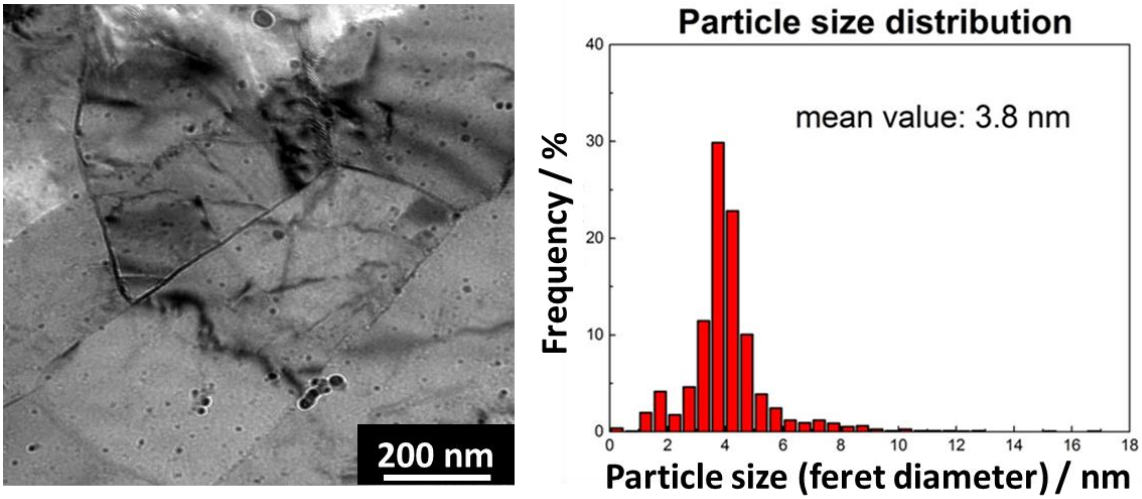

Fig. 21 TEM image and particle size distribution of hot-rolled 13Cr ODS Steel.

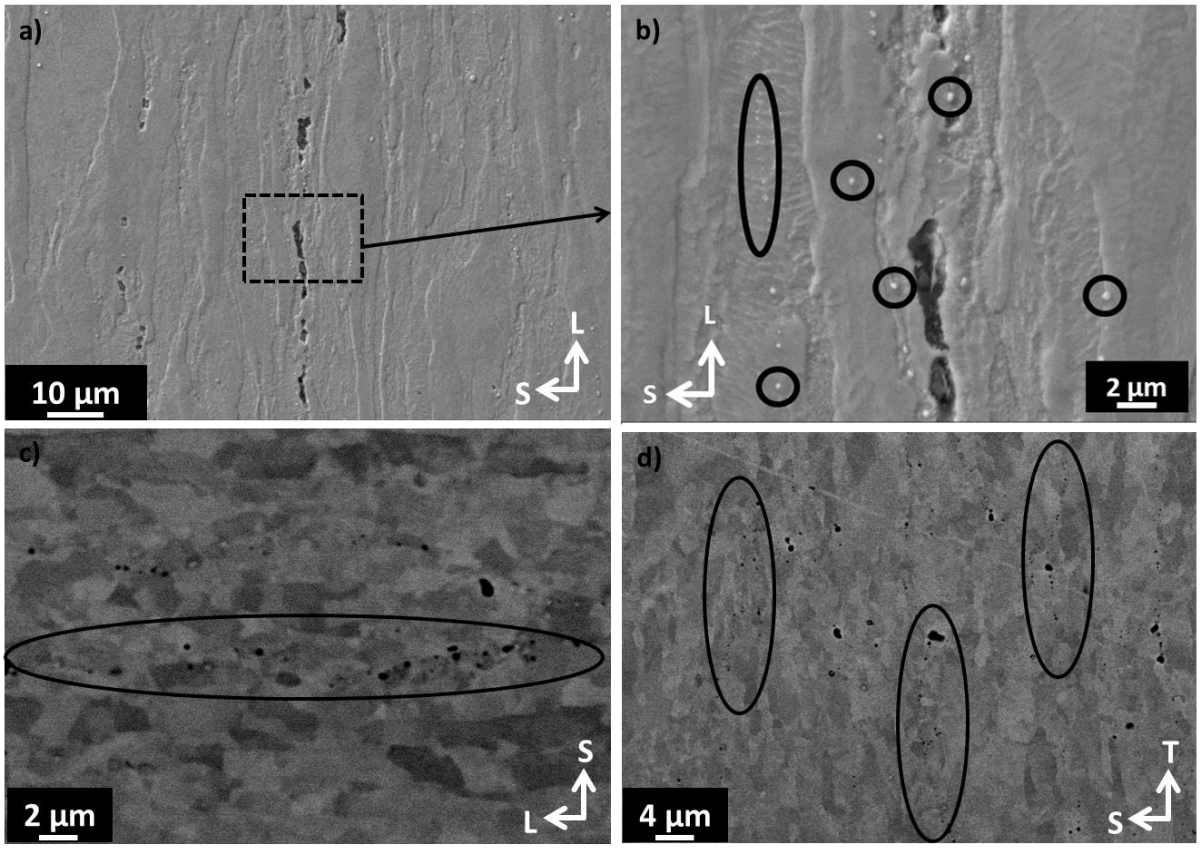

Fig. 22 SEM images showing Ti-enriched particles (encircled) in ODS-KIT HR found by EDS on etched surface along with some pre-existing cracks (a and b) and backscattered SEM image of OP-S polished surface showing aligned holes (encircled) formed after Ti-enriched particle fall out in the c) LS plane and in the d) TS plane.

4.1.2 ODS-KIT HE

Grains

In ODS-KIT HE, the coarse grains are arranged in zones elongated in the direction of the extrusion. The coarse grains (> 3 µm) are 'cigar'-shaped and are elongated in the direction of extrusion with a GAR of 10 as can be seen from the grain distribution (Fig. 23) and IPF maps (Fig. 25). The coarse grains are further divided into sub-grains marked by low-angle grain boundaries (misorientation angle < 10°) with a size similar to the fine grains as seen in the superimposed grain distribution and quality maps (Fig. 23) and low magnification STEM image (Fig. 24). The fine grains are equiaxed (< 3 µm) and are arranged in fine-grained zones similar to the coarse-grained zones (Table 3).The distinction between fine and coarse grains was made at 3 µm based on the grain size distribution.

The crystallographic texture from the IPF maps shows that the grains are preferentially oriented with the <110> direction parallel to the extrusion direction (Fig. 25). The X plot of the IPF in the T plane corroborates this by exhibiting a high intensity of [101]. There is no dominant texture perpendicular to the extrusion direction but weak textures of <111> and <001> are observed from the Y and Z plots of the IPFs in the T plane. The orientation distribution function (ODF) plot at a constant Euler angle φ_2 of 45° also confirms the α-fiber texture <110> parallel to the extrusion direction [50]. There is no difference between the fine and the coarse-grained regions in terms of texture as shown in Fig. 26, where IPF Z map of the T plane is plotted for the fine and coarse grains separately. The {100} planes of the grains are not parallel to any specific plane contrary to what was observed in ODS-KIT HR.

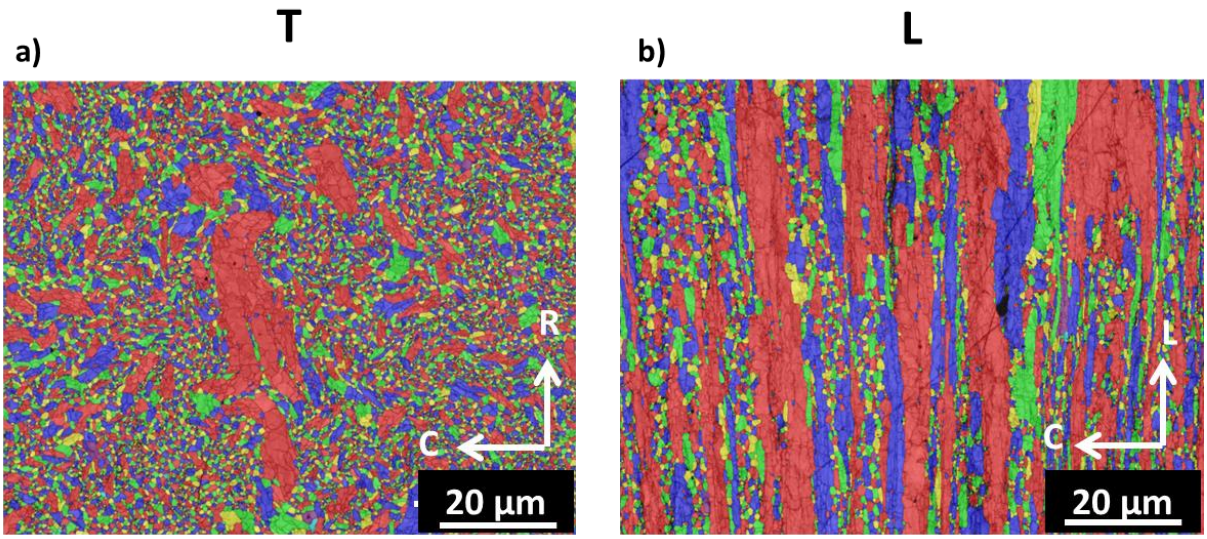

Fig. 23 Grain distribution map together with the superimposed quality map (10˚ misorientation threshold angle) of the a) transversal (T) and the b) longitudinal (L) plane in ODS-KIT HE.

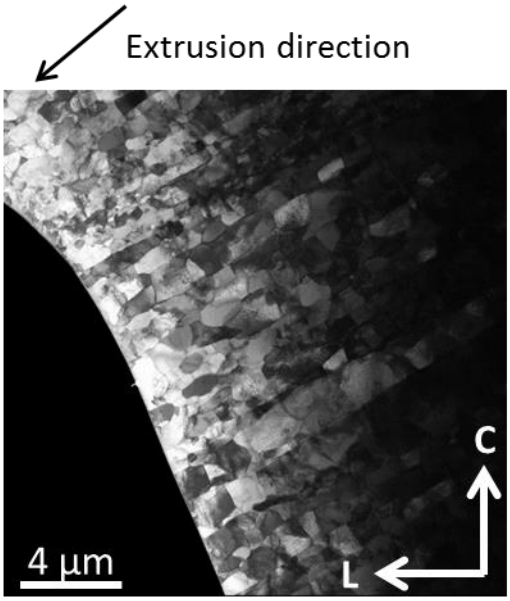

Fig. 24 Low magnification STEM image showing grains (both LAGB and HAGB) in ODS-KIT HE.

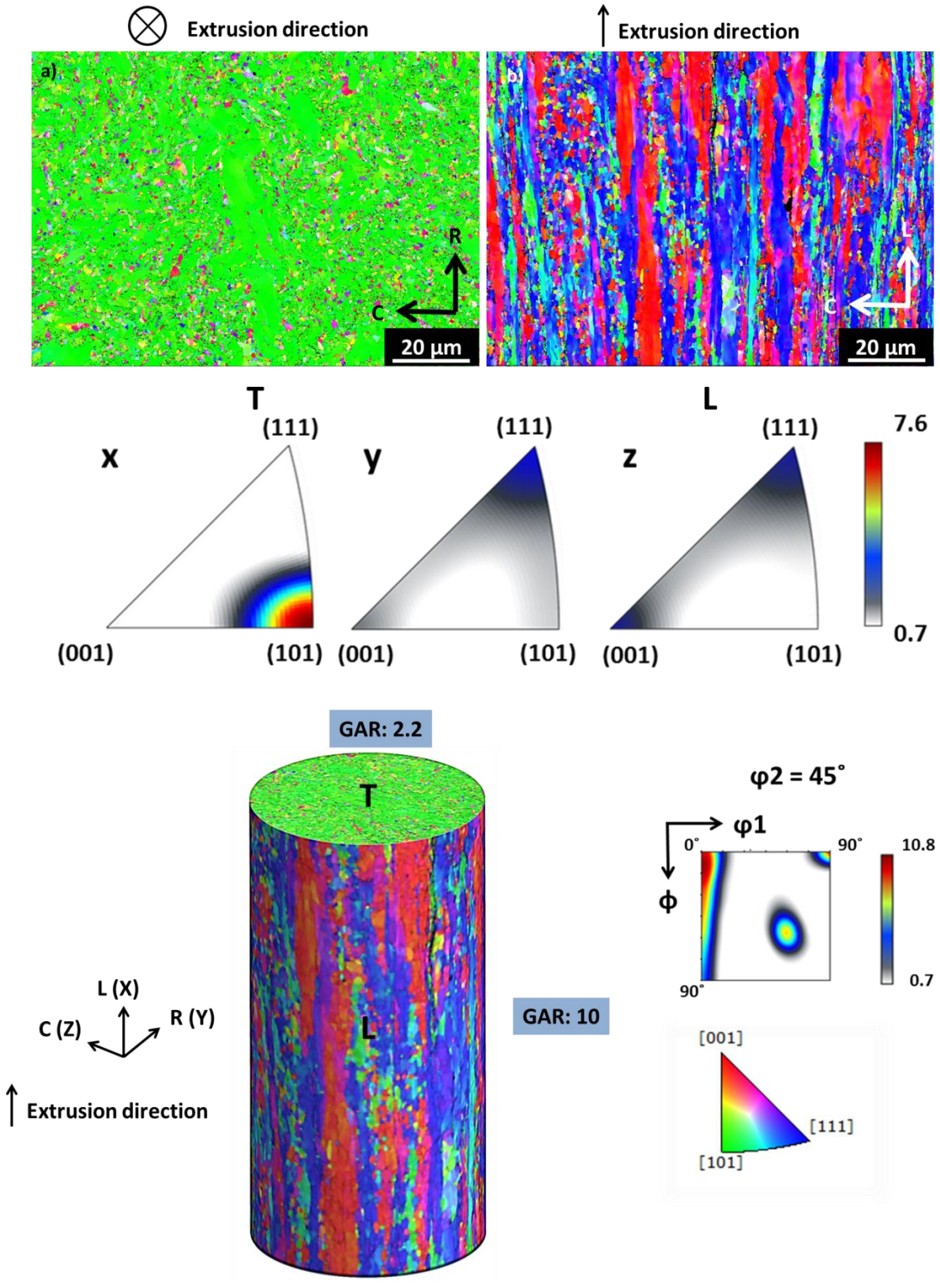

Fig. 25 Inverse pole figure Z maps of the transversal (T, top left) and the longitudinal (L, top right) plane along with the inverse pole figures in the T plane (middle) and the ODF plot at $\phi_2 = 45^\circ$ (right bottom). A schematic representation (left bottom) of ODS-KIT HE with 'cigar'-shaped elongated grains (not to scale) is presented. Indicated GAR values are for coarse grains.

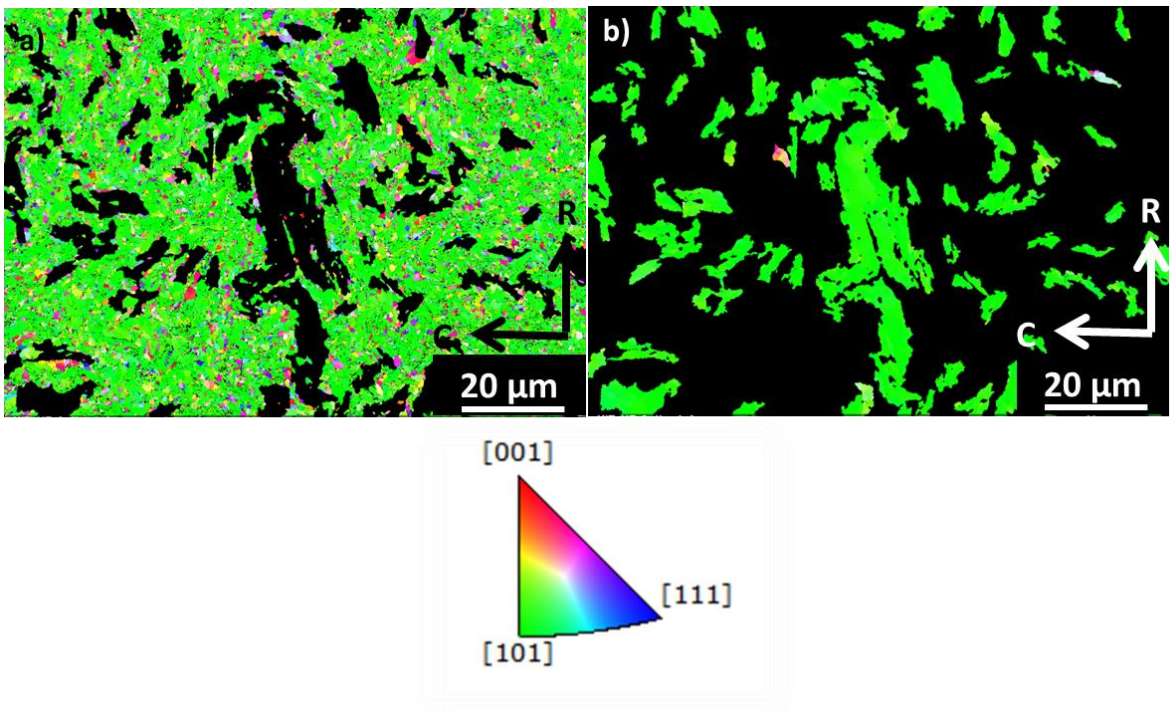

Fig. 26 Inverse pole figure Z map of ODS-KIT HE in the T plane selectively highlighting a) fine and b) coarse grains

Particles

The average nano-particle particle size in ODS-KIT HE is found to be 3 nm by TEM analysis (Fig. 27). The spatial distribution of the nano-particles is inhomogeneous with no visible preference to the grain boundaries.

Sub-micron particles in ODS-KIT HE are located sometimes on the grain boundaries (Fig. 28a) and sometimes inside the grains (Fig. 28b) with a size ranging from 30 nm to 130 nm (average size 60 nm) as can be seen from the low magnification TEM micrographs. Most of these particles are arranged in high number density bands parallel to the extrusion direction (HD zones) covering a length of several µm and with a mean thickness of 0.4 µm (Fig. 28b). The backscattered SEM image in Fig. 29 shows that the mean spacing between individual bands is 7.6 µm. The particle number density in the regions between these bands is low (LD zones). The backscattered image shows the holes left out by the sub-micron particles after OP-S polishing. These are very close to the resolvable limit using SEM. The mean particle size, the inter-particle spacing and the volume fraction of the sub-micron particles can be found in Table 5 separately for the HD and LD zones. STEM-EDS was performed to obtain information on the composition of the particles as shown in Fig. 28c and Fig. 30. The majority of the sub-micron particles are enriched with Ti which can be assumed to be Ti oxides. Occasionally, the particles are enriched with Al and/or Y particles. As Al is present in small quantities in the bulk composition, it is highly unlikely that it would be the reason for the presence of Al enriched particles (Table 2). The Al particles possibly originated from contamination of the powder during or after milling.

Table 5 Sub-micron particle analysis of low and high number density regions using TEM images of ODS-KIT HE and ODS-CSM.

Material	Region	Mean Particle Size (µm)	Volume fraction	Inter-particle spacing (µm)
ODS-KIT HE	HD zone	0.06	0.038	0.22
ODS-KIT HE	LD zone	0.06	0.0027	0.87
ODS-CSM	HD zone	0.47	0.0134	2.93
ODS-CSM	LD zone	0.09	0.0016	1.65

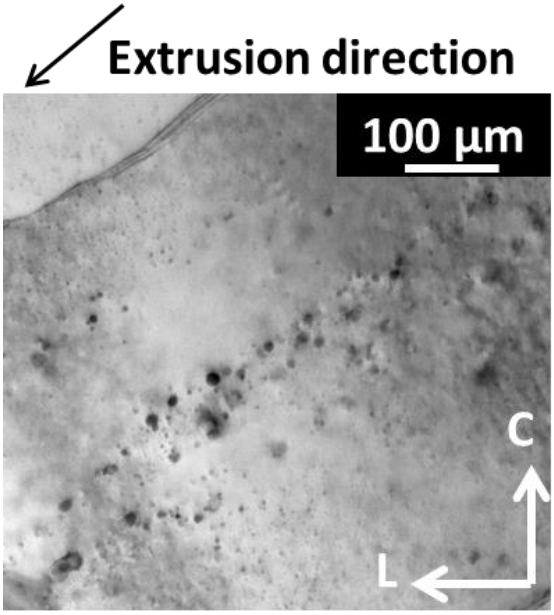

Fig. 27 A high magnification bright field TEM image of ODS-KIT HE showing nano-particles.

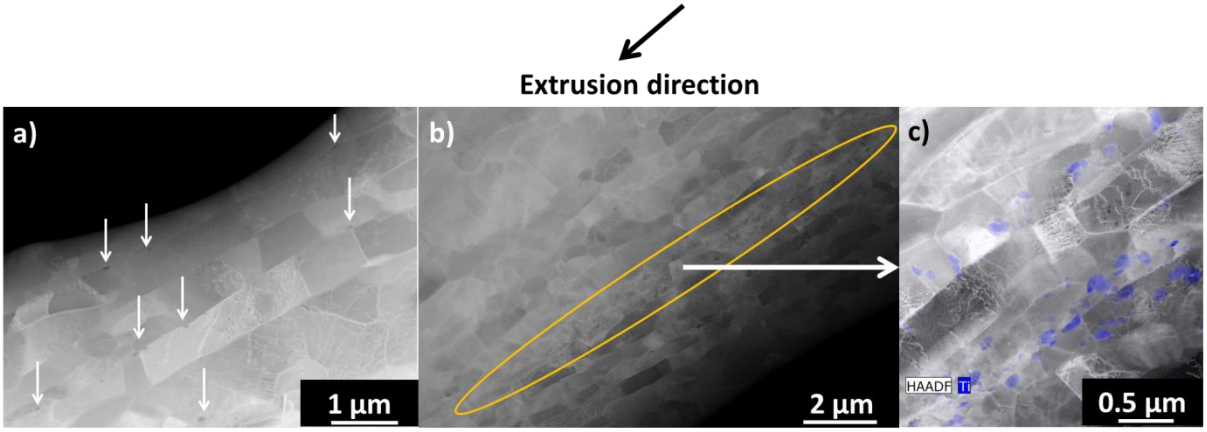

Fig. 28 Low magnification STEM images of ODS-KIT HE indicating presence of sub-micron particles on a) grain boundaries and b) inside grains arranged and elongated towards the extrusion direction. c) shows an HAADF-STEM image with elemental overlay map of region in b).

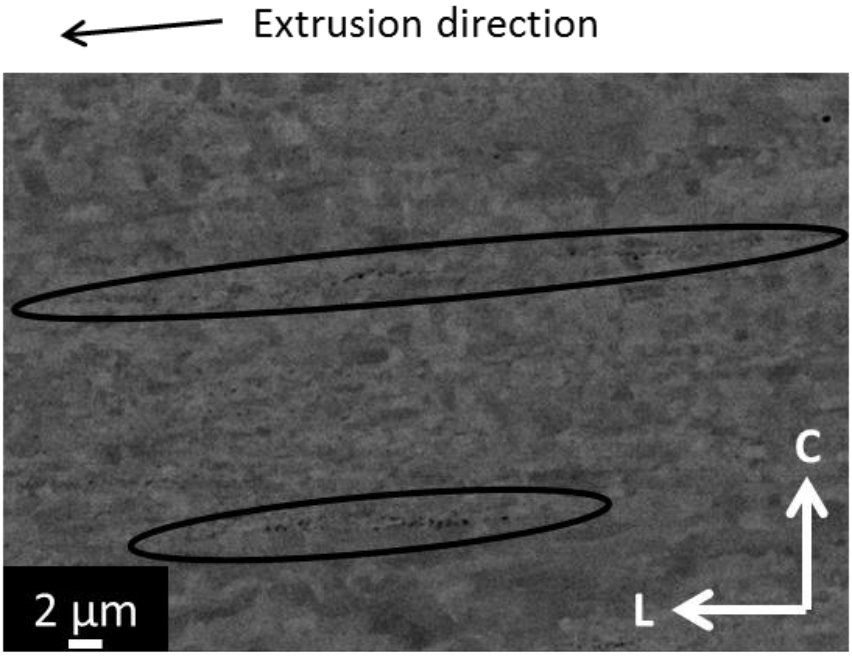

Fig. 29 SEM backscattered image of ODS-KIT HE showing grain contrast along with holes left out by sub-micron particles after OP-S polishing (encircled).

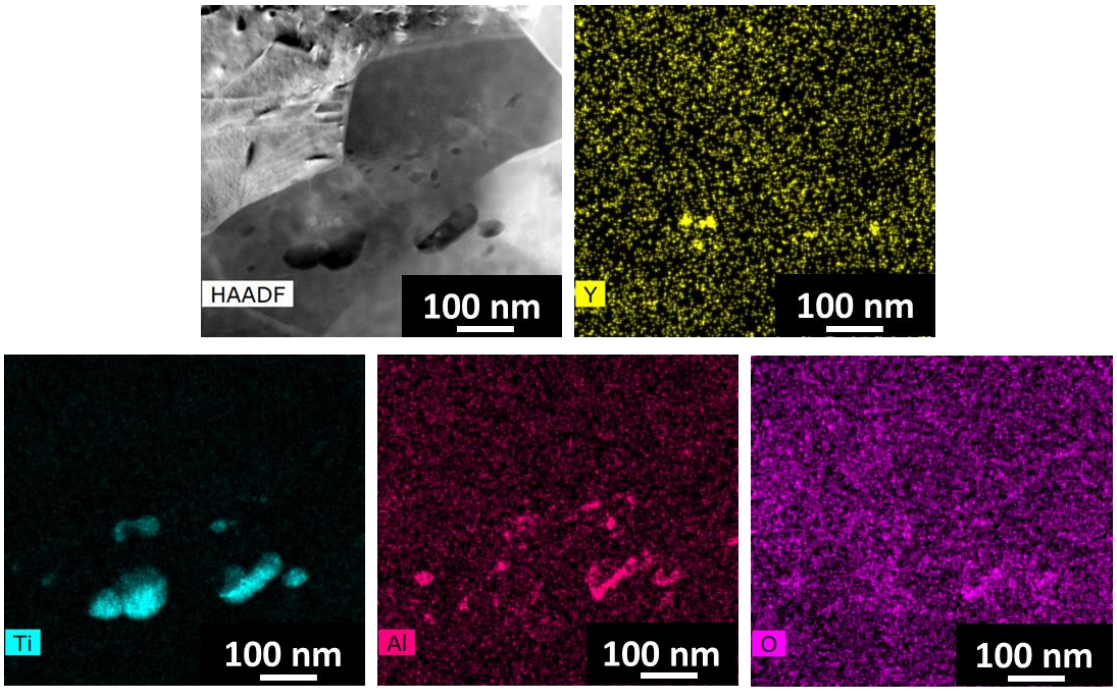

Fig. 30 HAADF-STEM image and elemental maps showing presence of Ti-enriched sub-micron particles with traces of Y and Al in ODS-KIT HE.

4.1.3 ODS-CSM

Grains

In ODS-CSM, the coarse grains are arranged in zones elongated in the direction of extrusion, similar to ODS-KIT HE. The coarse grains (> 1.5 µm) are partially elongated in the extrusion direction with a GAR of 3.3 as can be seen from the grain distribution maps (Fig. 31), low magnification STEM image (Fig. 32) and IPF maps (Fig. 33). Further division of coarse grains into sub-grains marked by low-angle grain boundaries (misorientation angle < 10°) are not observed in the superimposed grain distribution and quality maps (Fig. 31). The fine grains are equiaxed (< 1.5 µm) and are aligned in fine-grained zones similar to the coarse-grained zones (Table 3).The distinction between fine and coarse grains was made at 1.5 µm based on the grain size distribution.

The crystallographic texture shows that the grains are preferentially oriented with the <110> direction parallel to the extrusion direction (Fig. 33) as seen from the X plot of the IPF in the T plane. There is no dominant texture perpendicular to the extrusion direction with only a weak texture of <111> and <110> directions as observed from the Y and Z plots of the IPFs in the T plane. The ODF plot at a constant Euler angle φ_2 of 45˚ also confirms the dominant α-fiber texture of <110> parallel to the extrusion direction [50]. The fine and the coarse-grained regions both exhibited similar texture as shown in Fig. 34, where IPF Z map of the T plane is plotted for the fine and coarse grains separately. Similar to ODS-KIT HE, the {100} planes of the grains are not parallel to any specific plane.

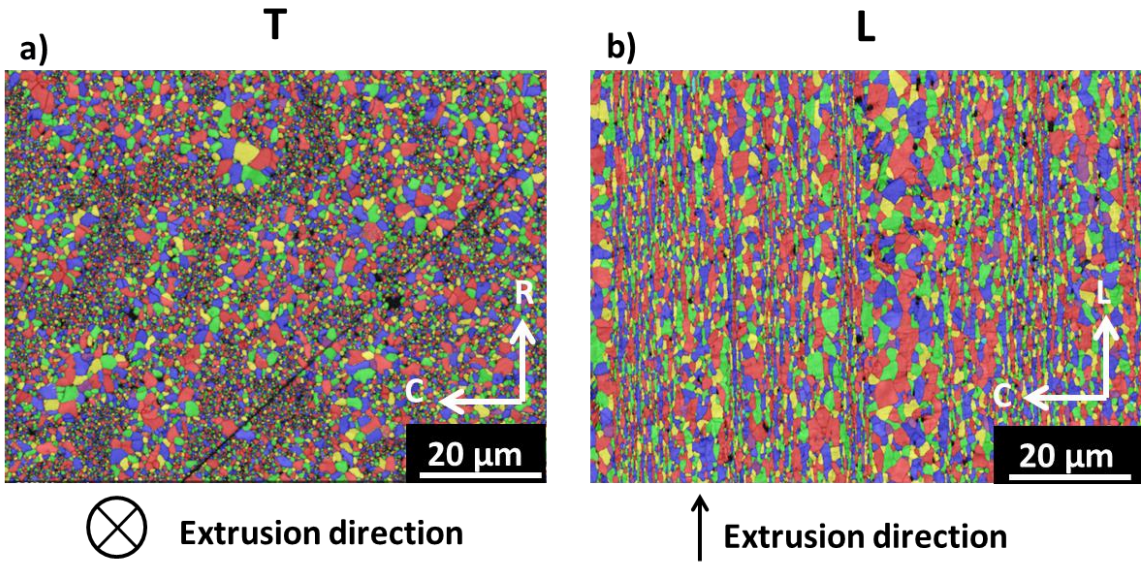

Fig. 31 Grain distribution map together with the superimposed quality map (10° misorientation threshold angle) of the a) transversal (T) and the b) longitudinal (L) plane in ODS-CSM.

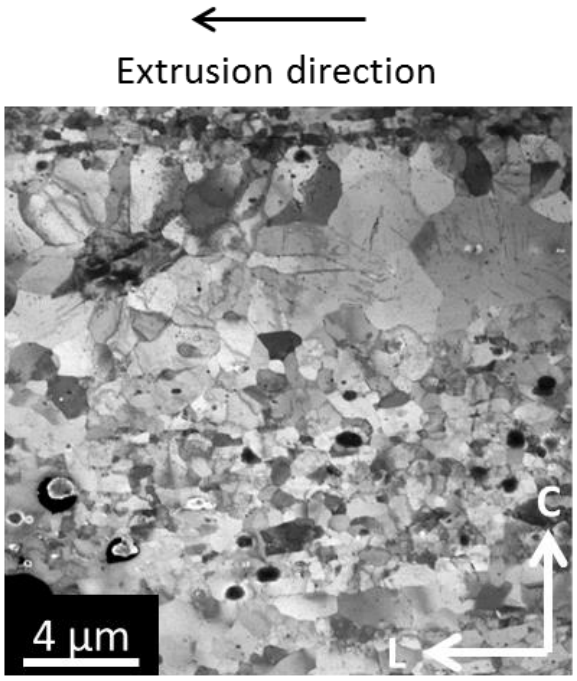

Fig. 32 Low magnification STEM image showing HD and LD zones of sub-micron particles along with coarse and fine-grained regions in ODS-CSM.

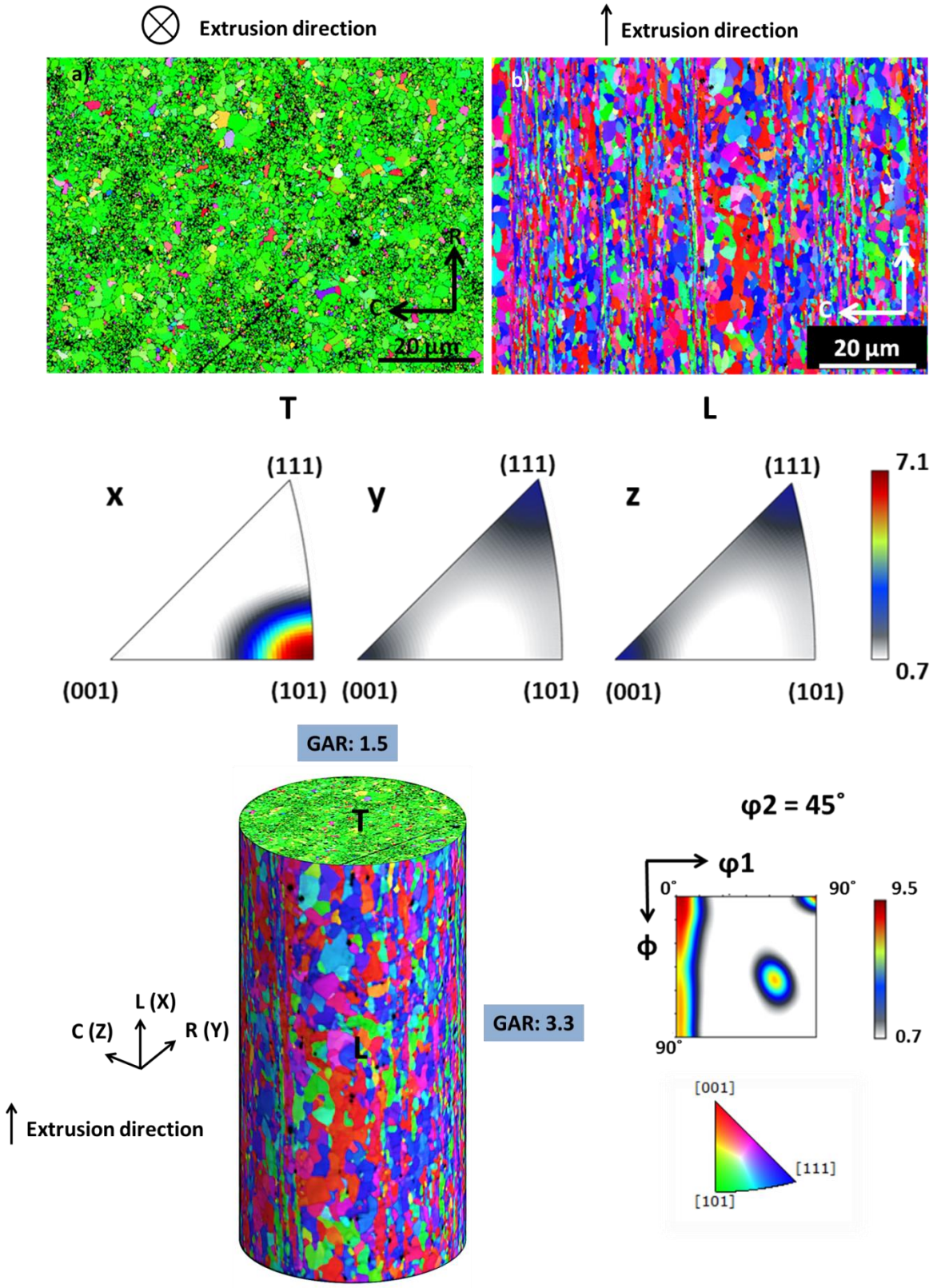

Fig. 33 Inverse pole figure Z maps of the transversal (T, top right) and the longitudinal (L, top left) plane along with the IPFs in the T plane (middle) and the ODF plot at ϕ_2 = 45° (right bottom). A schematic representation (left bottom) of ODS-CSM (not to scale) is presented. Indicated GAR values are for coarse grains.

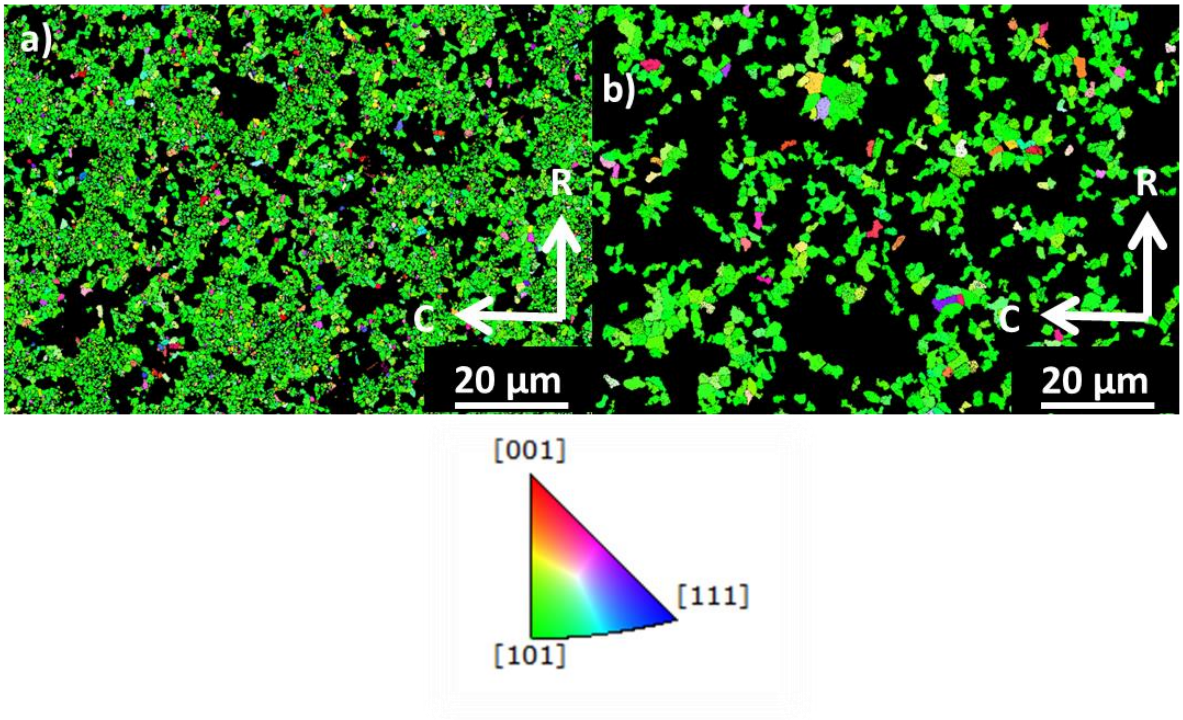

Fig. 34 Inverse pole figure Z map of ODS-CSM in the T plane selectively highlighting a) fine and b) coarse grains

Particles

The average nano-particle size in ODS-CSM is found to be 8 nm (Fig. 35b) by TEM analysis. The spatial distribution of the nano-particles is inhomogeneous with no visible preference to the grain boundaries similar to the other materials.

The sub-micron particles in ODS-CSM, in contrast with ODS-KIT HE, are larger (0.2 µm to 1.2 µm) and not arranged in bands as seen from the backscattered SEM image in Fig. 35a. Here, zones of high (HD zones) and low number density (LD zones) of the sub-micron particles can be distinguished within which the particles are distributed homogeneously. This is also confirmed from the low magnification STEM image in Fig. 32. The HD and the LD zones are elongated in the direction of extrusion and have a mean thickness of 4.4 µm and 6 µm, respectively. The HD zones often coincide with the fine-grained zones, while the LD zones often coincide with the coarse-grained zones. The larger sub-micron particles (mean size 0.47 µm) in ODS-CSM can be identified as Si oxides by STEM-EDS elemental mapping (Fig. 36). The smaller sub-micron particles (< 0.5 µm) include Y-oxides, Ti-oxides and oxides of more complex composition enriched in Y, Ti and Si. Additionally, Cr-rich precipitates, most likely Cr-rich carbides, are located predominately at the grain boundaries (Fig. 36).

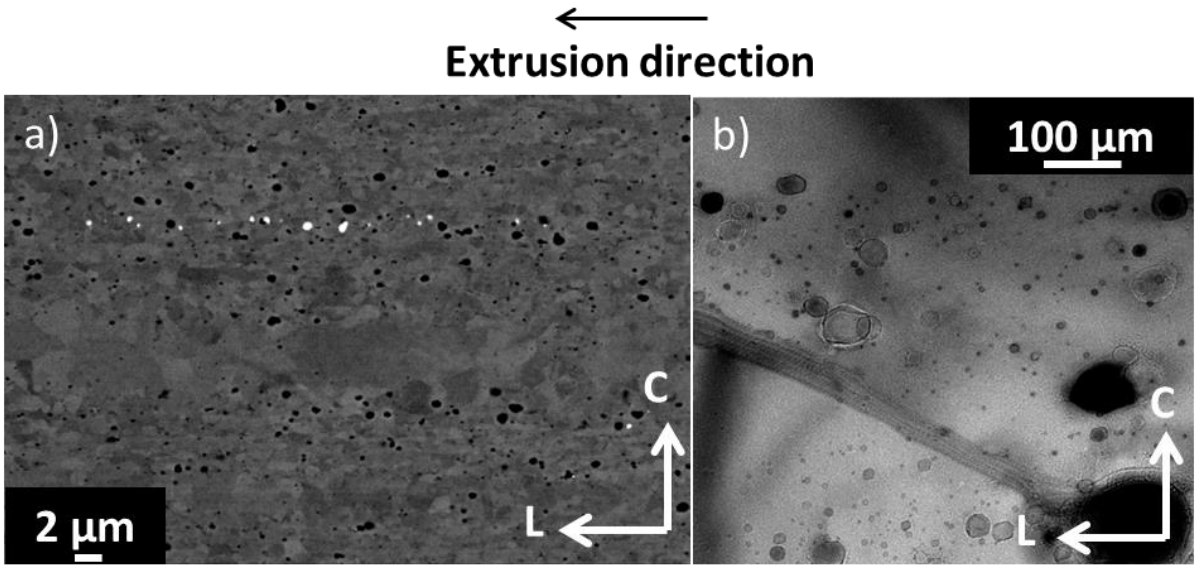

Fig. 35 a) SEM backscattered image showing grain contrast along with holes left out by sub-micron particles after OP-S polishing and b) a bright field TEM image of the nano-particles in ODS-CSM.

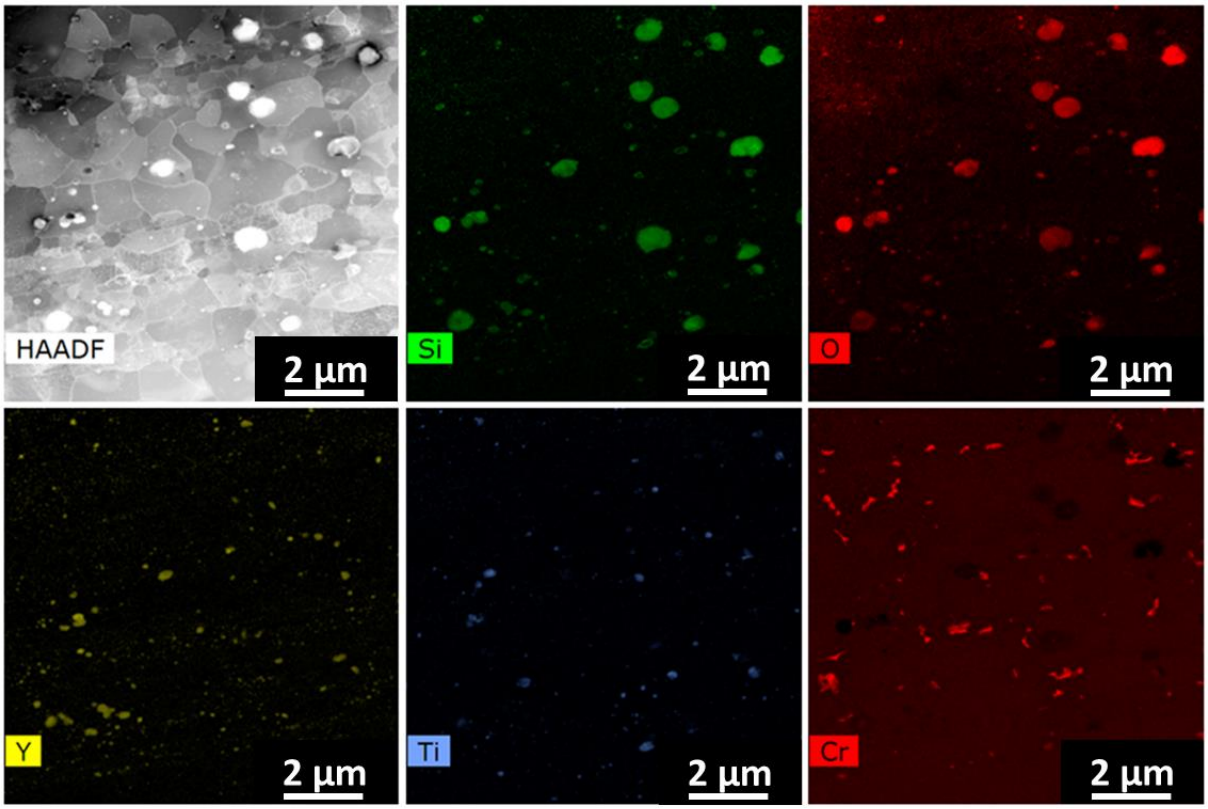

Fig. 36 HAADF-STEM image and elemental maps showing presence of Si and O-enriched sub-micron particles along with some smaller Y and Ti particles in ODS-CSM. Cr enrichments were observed at the grain boundaries (right below).

4.1.4 Summary

All the ODS steels in this work contain bimodal microstructure, which after manufacturing processing, transforms into zones of coarse and fine grains elongated in the rolling/extrusion direction. As these manufacturing processes differ from each other, the zones and the grains inside them possess different morphologies. Hot-rolling gives rise to 'pancake'-shaped microstructure morphology (ODS-KIT HR) while hot-extrusion leads to 'cigar'-shaped (ODS-KIT HE) and partially elongated grain morphology (ODS-CSM).

A texture with grains preferentially oriented with the <110> direction parallel to the rolling/extrusion direction is observed for all ODS steels. A clustering of {100} cleavage planes are found parallel to the rolling plane in hot-rolled ODS steel while such an arrangement is not found in the hot-extruded materials.

Nano-particles in all the ODS steels are similar in size with inhomogeneous spatial distribution inside the grains. The sub-micron particles in ODS-KIT HR and ODS-KIT HE are Ti-enriched and smaller (60 nm). On the other hand, the sub-micron particles in ODS-CSM are Si-enriched and almost one order of magnitude larger (0.47 μm).

The mechanical properties of a material are affected by the basic microstructure. Therefore in the next few sections, we will look at the mechanical properties, beginning with the tensile properties and then moving on to the fracture properties. The next section on tensile tests throws light on the following:

- How does the strength of ODS steels vary with temperature?
- How do the strengths compare with each other and with the strength of FM steel?
- How does the ductility of ODS steels vary with temperature?
- How does the ductility compare with each other and with the ductility of FM steel?

4.2 Tensile tests

A tensile test is the most common method to obtain basic information about the mechanical properties of a material such as the strength and ductility. All the ODS steels exhibit a general decrease in yield strength and ultimate tensile strength with an increase in temperature in the longitudinal direction as can be seen from the strength versus temperature plot in Fig. 37a. A ferritic martensitic P91 non-ODS steel (Fe9Cr0.1C1Mo0.5Mn0.46Si0.23V0.23Ni in wt. %) tested also in the longitudinal direction is presented for comparison. ODS-KIT HE exhibits higher yield strength and ultimate tensile strength than all the other materials from RT up to 400 ˚C. At temperatures greater than 400 ˚C, the yield strength and ultimate tensile strength of all the materials drops at a higher rate. The differences in yield and ultimate tensile strength at 600 °C are not as large as at RT for all the ODS steels. P91 exhibits lower yield strength and ultimate tensile strength than ODS steels at all temperatures, however, the differences in strengths at temperatures greater than 500 °C is not too large. As seen from the total elongation versus temperature plot in Fig. 37b, the total elongation drops to a minimum value between

200 ˚C and 400 ˚C for ODS steels and at 500 ˚C for P91 steel after beginning at a slightly higher value at RT. An increase in total elongation is observed at temperatures greater than 500 ˚C with the highest ductility at 600 ˚C for ODS steels and at 800 ˚C for P91 steels. A stronger drop in ductility is seen for ODS steels above 600 ˚C possibly due to weakening of grain boundaries (discussed later).

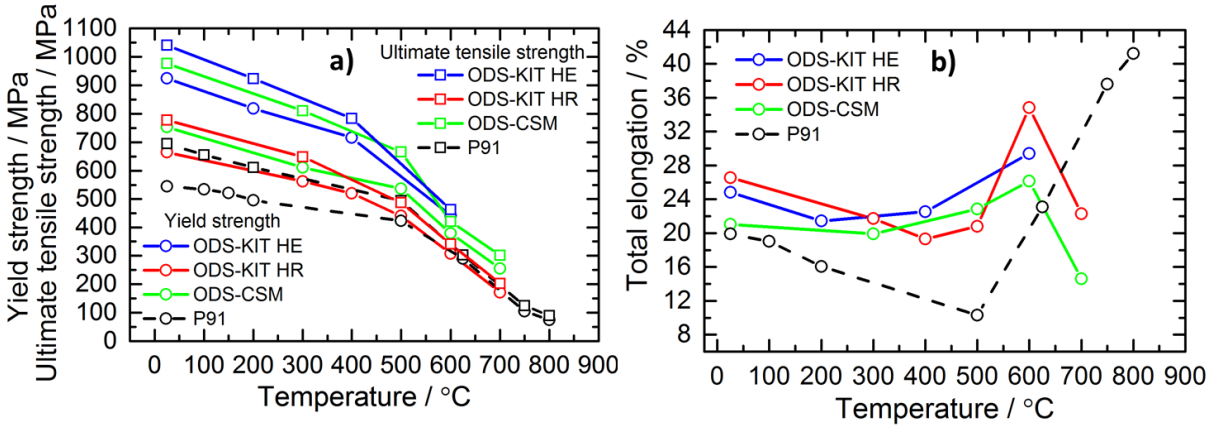

Fig. 37 a) Yield strength and ultimate tensile strength and b) total elongation variation with increasing temperature for all three ODS steels along with P91 steel in the longitudinal direction.

4.2.1 Summary

The strength of all the ODS steels drop gradually between RT and 400 ˚C, while the drop at temperatures greater than 400 ˚C is steeper. ODS-KIT HE exhibits slightly higher strengths than the other ODS steels between RT and 400 ˚C. Above 400 ˚C, the difference in strengths between all the ODS steels is not much. The ductility of all the ODS steels are similar with the maximum ductility appearing close to 600 °C. ODS steels exhibit in general, higher strength and ductility than ferritic martensitic steel P91 in the temperature range of RT and 500 ˚C. Above 500 °C, ODS steels have similar strength and ductility to P91.

The next section deals with the fracture toughness which, along with fracture mechanisms, constitutes the fracture behaviour of materials. The tensile properties of a material form the basis for all the fracture toughness calculations. The following questions will be addressed in the next section:

- How does the fracture toughness of ODS steels vary with temperature?
- Is there a dependence of fracture toughness of ODS steels on orientation?
- How does the fracture toughness of ODS steels compare with each other?
- How does the fracture toughness of ODS steels compare with FM steel?

4.3 Fracture toughness tests

ODS steel samples were tested at various temperatures from -100 °C to 700 °C and in various orientations using J_Q values (provisional J_{IC} values determined by the intersection of the J-R curve with the 0.2 mm offset line) which are listed inTable 6. The energy release rate for elastic-plastic material, J-integral or the J_Q value, is proportional to the fracture toughness of a material. The variation of fracture

toughness over the temperature range is plotted in the J_Q versus temperature plots for different orientations. Even though single specimen per temperature was tested for some materials, the systematic testing at temperatures intervals of 100 ˚C gives an idea about the trend of the fracture toughness at a particular temperature range. The J-Δa or J-R curves, which represent the fracture properties of materials, are also presented. The Load-load line displacement and the Δa – load line displacement curves provide information about the strength and ductility of the materials.

4.3.1 ODS-KIT HR

A general trend of decreasing fracture toughness (expressed in terms of J_Q) with increasing temperature is observed for both the orientations, L-T and T-L (Fig. 38a). In the L-T orientation, with the exception of RT, the fracture toughness remains more or less constant up to 400 °C after which a rapid decrease is observed. The T-L orientation exhibits a decrease in fracture toughness with increasing temperatures up to 400 ˚C. The decrease above 400 ˚C is less steep as compared with the L-T orientation. The fracture toughness of the L-T orientation is higher than that of the T-L orientation at all temperatures. The T-L oriented samples tested at 200 °C, 400 °C and 500 °C encountered unstable crack propagation (J_Q values suffixed with U in Table 6). The J-R curve in the L-T orientation is steeper than in the T-L orientation at RT as shown in Fig. 38b. The load maximum is higher for the L-T orientation than for the T-L orientation as can be seen from the load versus load line displacement plot in Fig. 38c. The area under the curve is also larger for the L-T orientation. The T-L oriented specimens exhibit larger crack growth than the L-T oriented specimens for the same load line displacement at RT as can be seen from the crack growth versus load line displacement plot in Fig. 38d.

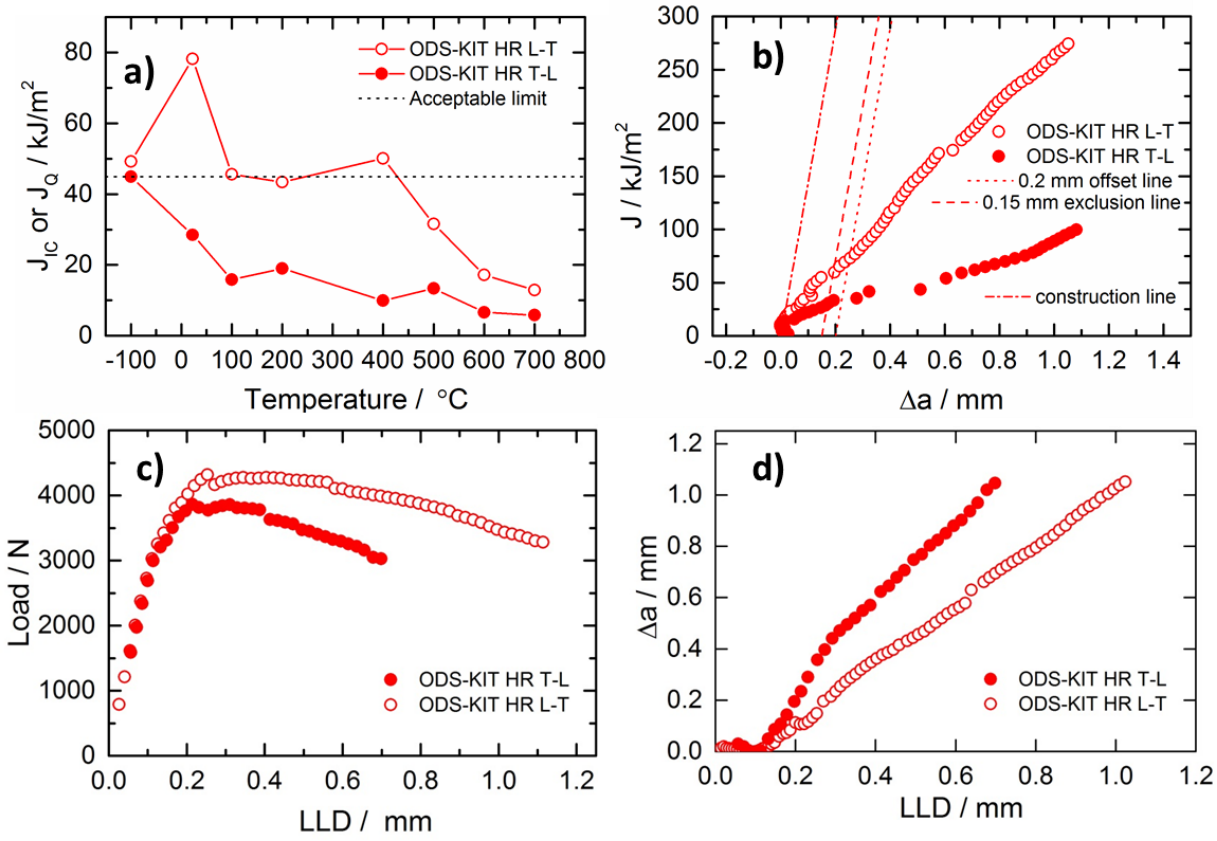

Fig. 38 a) Fracture toughness (J_Q) values at various temperatures, b) J-integral versus crack growth curves at RT, c) Load versus load line displacement curves at RT and d) crack growth versus load line displacement curves at RT for L-T and T-L oriented specimen of ODS-KIT HR.

Table 6 Fracture toughness (J_Q) values for ODS-KIT HR in various orientations and at various temperatures in kJ/m^2.

Orientation	Temperature (˚C)							
	-100	22	100	200	400	500	600	700
L-T	49.2	78.2	45.6	43.4	50.1	31.6	17.1	12.9
T-L	45	28.4	15.8	19U	9.9U	13U	6.5	5.8

4.3.2 ODS-KIT HE

The L-C oriented specimens exhibit the highest fracture toughness followed by the C-R and C-L orientations as seen from the J_Q versus temperature plot in Fig. 39a. At a temperature range of RT to 400 ˚C, the L-C oriented specimen shows a gradual decrease up to 400 ˚C, after which a steep decrease is observed. The fracture toughness of the C-R and C-L oriented specimen does not vary much between RT and 400 ˚C, after which they decrease gradually. Unstable crack propagation took place in ODS-KIT HE at RT in the C-R and C-L orientations. Their corresponding fracture toughness values are suffixed with U in Table 7, where all the fracture toughness values at different temperatures are presented. The L-C oriented specimens at 200 ˚C exhibited a much steeper J-R curve (Fig. 39b) than

the C-R and C-L oriented specimen. For the test at 200 °C, the maximum load in the L-C and in the C-R orientation is similar and is higher than the C-L orientation as seen from the load versus load line displacement plot in Fig. 39c. The L-C orientation exhibits the largest area under the curve. Lesser crack growth is observed for the L-C orientation as compared to the C-R and C-L orientations for the same load line displacement at 200 ˚C as seen from the crack growth versus load line displacement curve in Fig. 39d.

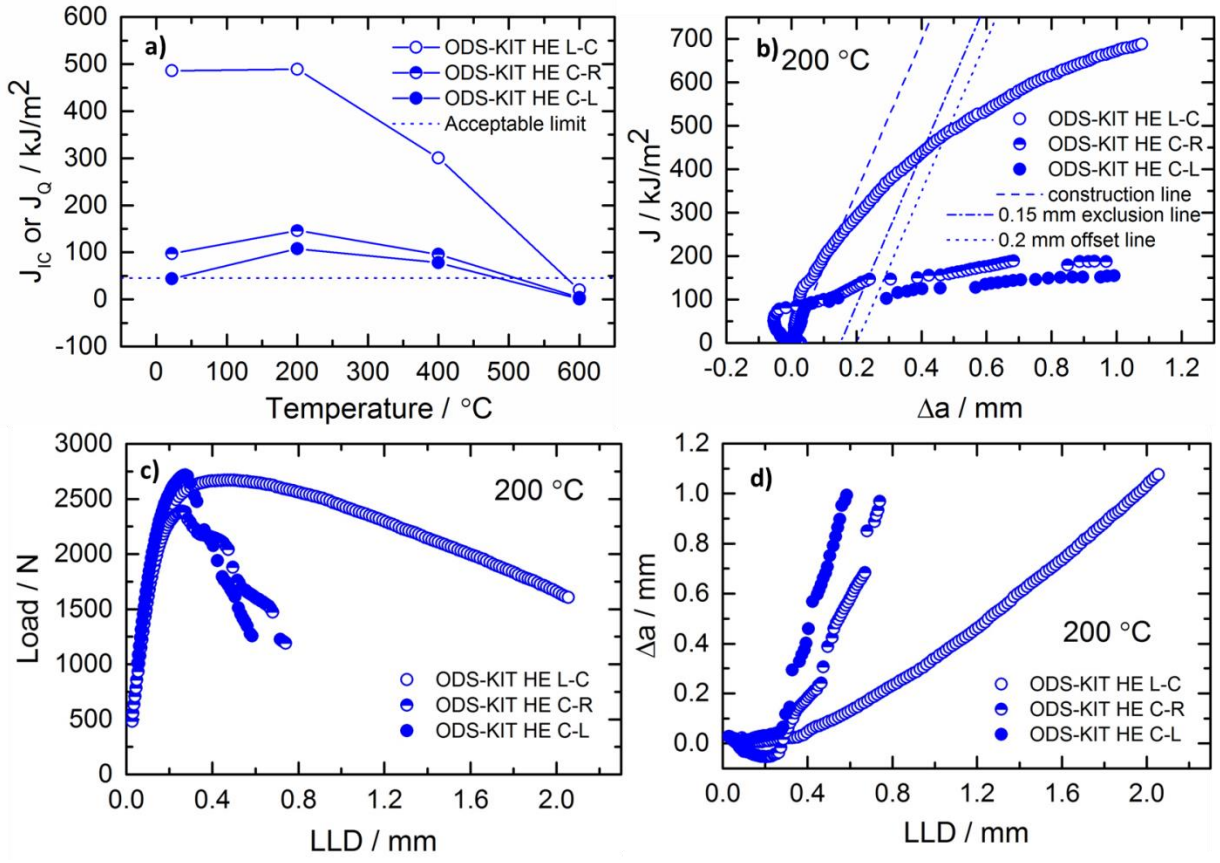

Fig. 39 a) Fracture toughness (J_Q) values at various temperatures, b) J-R curves at 200 ˚C, c) Load versus load line displacement curves at RT and d) crack growth versus load line displacement curves at 200 ˚C for L-C, C-R and C-L oriented specimen of ODS-KIT HE.

Table 7 Fracture toughness (J_Q) values for ODS-KIT HE in various orientations and at various temperatures in kJ/m^2.

Orientation	Temperature (°C)			
	22	200	400	600
L-C	486.27	488.52	300.73	19.69
C-R	97.26U	146.17	95.6	4.04
C-L	44.07U	107.54	78.06	0.95

4.3.3 ODS-CSM

The L-C oriented specimens exhibit the highest fracture toughness in ODS-CSM, similar to ODS-KIT HE as seen from the J_Q versus temperature plot in Fig. 40a. The fracture toughness in C-R and C-L oriented specimens decreases gradually from RT to 600 ˚C while it drops steeply between 200 ˚C and 600 ˚C for the L-C oriented specimen. The crack propagation at all temperatures and in all the orientations was stable and the fracture toughness values are presented in Table 8. The J-R curve at RT shows a steeper curve for the L-C oriented specimen followed by the C-R and the C-L orientated specimens (Fig. 40b). For the test at RT, as also presented in the load versus load line displacement plot in Fig. 40c, the maximum load and the area under the curve is highest in the L-C orientation followed by the C-R and C-L orientations. The crack growth was the least at RT for the L-C orientation followed by the C-R and C-L orientations for the same load line displacement as can be seen from the crack growth versus load line displacement plot in Fig. 40d. A similar trend was also observed in ODS-KIT HE at 200 °C (Fig. 39d).

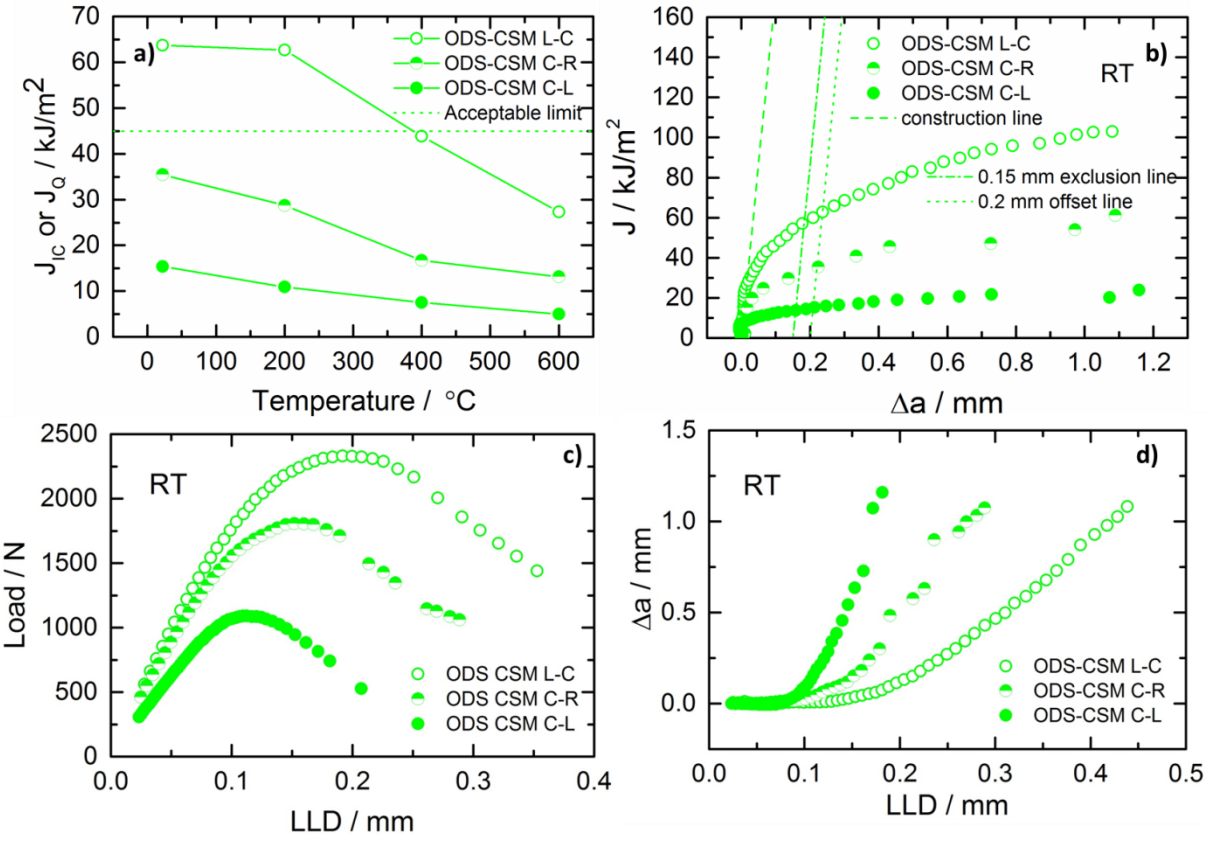

Fig. 40 Fracture toughness (J_Q) values at various temperatures, b) J-R curves at RT, c) Load versus load line displacement curves at RT and d) crack growth versus load line displacement curves at RT for L-C, C-R and C-L oriented specimen of ODS-CSM.

Table 8 Fracture toughness (J_Q) values for ODS-CSM in various orientations and at various temperatures in kJ/m^2.

Orientation	Temperature (°C)			
	22	200	400	600
L-C	63.68	62.64	43.87	27.35
C-R	35.48	28.72	16.7	13.13
C-L	15.31	10.87	7.5	5

4.3.4 Comparison

ODS-KIT HE exhibits overall higher fracture toughness values (Table 7) than the other two ODS steels in all orientations from RT to 400 ˚C. The fracture toughness in the strongest orientation is plotted against the yield strength for various materials at different temperatures and is presented in Fig. 41a. The fracture toughness values are well above the acceptable fracture toughness limit of J_Q = 45 kJ/m^2 (K_{JQ} = 100 MPa√m) as reported by Byun et al. [7] and are close to the fracture toughness values of P91 steel in the temperature range of RT to 400 ˚C. The P91 steel used for comparison exhibited no fracture anisotropy. All the three ODS steels are above the acceptable limit in the temperature range of RT to 400 ˚C and also possess sufficient yield stress for engineering applications (> 500 MPa). Between 400 ˚C and 600 ˚C, ODS-KIT HE loses fracture toughness steeply and drops below the acceptable limit (Fig. 41a). The fracture toughness of ODS-KIT HR and ODS-CSM also drops below the acceptable limit in this temperature range but the drop is not as steep as compared to ODS-KIT HE. The fracture toughness loss is accompanied by large yield strength deterioration for all the ODS steels. The fracture toughness of P91 steel on the other hand drops only slightly between 200 ˚C and 400 ˚C but is still easily above the acceptable fracture toughness limit. Above 400 ˚C, the fracture toughness of P91 steel increases again. The yield strength of P91 deteriorates to a value below 500 MPa at and above 200 ˚C.

Among the ODS steels, the load maximum for ODS-KIT HR is the highest followed by ODS-KIT HE and ODS-CSM at 200 ˚C as seen from the load versus load line displacement plot in Fig. 41b. However, the load maximum for P91 is the highest. The area under the graph is highest for ODS-KIT HE and P91 followed by ODS-KIT HR and ODS-CSM. At 600 °C, among the ODS steels, the maximum load for ODS-KIT HR still remains the highest, yet lower than P91 steel (Fig. 41d). Although the area under the graph for ODS-KIT HE reduces drastically at 600 °C as compared with the test at 200 ˚C, the area under the graph for P91 still remains higher than all of the ODS steels.

At 200 °C, among the ODS steels, the least crack growth takes place for ODS-KIT HE followed by ODS-KIT HR and ODS-CSM for the same load line displacement as seen from the crack growth versus load line displacement curve in Fig. 41c. P91 steel exhibits similar crack growth as ODS-KIT HE. At 600 °C, all the ODS steels exhibit similarly high crack growth (steeper than at 200 °C) while P91

steel exhibits a much lower crack growth for the same load line displacement (shallower than at 200 °C) (Fig. 41e).

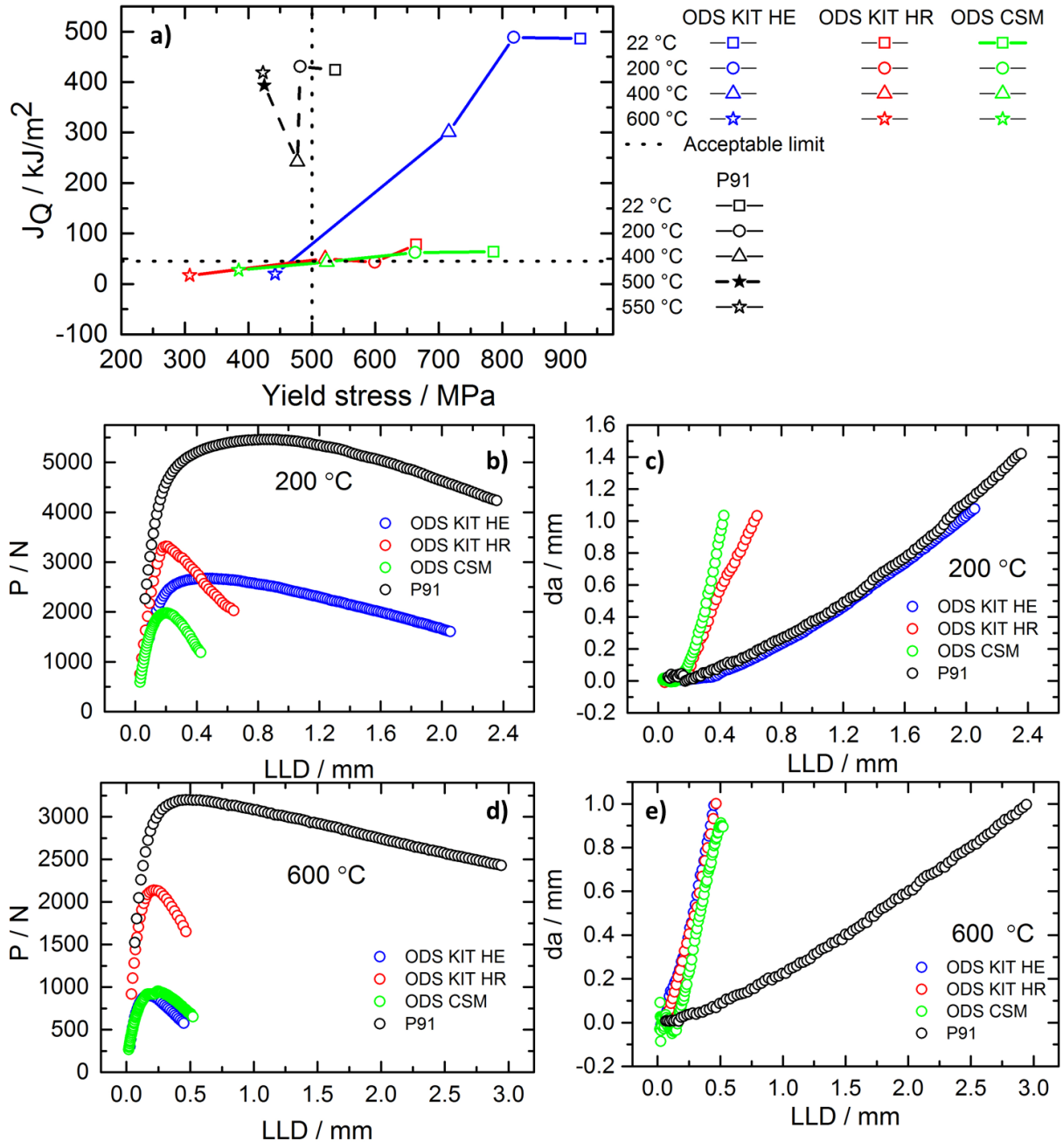

Fig. 41 a) Fracture toughness (J_Q value) versus yield stress plots at different temperatures, (b and d) load versus load line displacement curves at 200 ˚C and 600 ˚C respectively and (c and e) crack growth versus load line displacement curves at 200 ˚C and 600 ˚C respectively for all the three ODS steels in their strongest orientations (L-C and L-T) along with P91 ferritic martensitic steel.

4.3.5 Summary

There is a general trend of decreasing fracture toughness with increasing temperature for all the ODS steels. There is also a dependence of fracture toughness with specimen orientation. The lowest fracture toughness is exhibited by specimen orientations which have crack propagation direction parallel to the

rolling/extrusion direction. All the ODS steels perform well and exhibit fracture toughness above the acceptable limit in the temperature range of RT to 400 °C. ODS-KIT HE especially reaches high fracture toughness in this temperature range, almost comparable with P91. Above 400 °C, the fracture toughness of all ODS steels go below the acceptable limit and the yield strength also reduces drastically.

After fracture toughness, it is important to understand the fracture mechanisms in order to completely describe the fracture behaviour of a material. For that purpose, we will look at the fracture surfaces in the next section. Some questions pertinent for the next section are:

- How do the primary fracture surfaces look like?
- Are there secondary cracks and if yes, how does secondary fracture surface look like?
- What influence do secondary cracks have on primary cracks?
- What are the fracture mechanisms working at various temperatures?

4.4 Fracture surfaces

After fracture toughness testing, the samples were heat tinted and broken apart. The fracture surfaces were investigated under SEM. Each fracture surface narrates a different story giving information about the fracture mechanisms involved. Primary and secondary fracture surfaces were examined for all ODS steels at various temperatures and orientations. The coloured region seen on the fracture surfaces is formed due to heat tinting after testing and represents the crack growth region. At and above 400 ˚C, no additional heat tinting was required as the heat tinting took place during testing.

4.4.1 ODS-KIT HR

Primary cracks

The fracture surfaces comprise of a non-uniform primary crack growth region together with secondary cracks, which are growing in a plane perpendicular to the primary crack plane and running ahead of the primary crack as can be seen from the stereo microscopic images in Fig. 42. The primary crack growth region of the T-L oriented specimen at 200 ˚C and 400 ˚C are not clearly visible due to unstable crack propagation. Secondary cracks can be observed at all the testing temperatures for the L-T oriented specimen but disappear at and above 200 ˚C for the T-L oriented specimen. Primary crack growth is retarded at regions where secondary cracks grow resulting in its irregular shape. The ASTM nine point method suggests no more than 0.05B (where B is the thickness of the C(T) specimen) deviation of the individual primary crack measurements from the average measured final primary crack length. This condition was not fulfilled due to the irregular nature of the primary crack and hence only a provisional J value (J_Q) could be determined (section 4.3).

At -100 ˚C, the L-T oriented specimens experienced both cleavage and ductile fracture as can be seen from the SEM images of fracture surfaces (Fig. 43a, b and c) which shows the existence of both cleav-

age facets and dimples on the same fracture surface. The cleavage fracture region is formed after a small ductile fracture region is already formed (Fig. 43b). The T-L oriented fracture surface at -100 ˚C contains shallower dimples (Fig. 43f) mixed with a few flat cleavage features (Fig. 43d). At RT, the L-T oriented fracture surface is marked with equiaxed dimples whereas slightly elongated flat dimples in the direction of rolling are observed in the T-L oriented fracture surface (Fig. 44).

In the ductile regime (T ≥ RT), regions of fine, medium and large dimples can be observed on the fracture surfaces similar to the one seen for the test at 100 ˚C in the T-L orientation as seen from the SEM image in Fig. 45. The fracture morphology remains predominantly ductile at 200 ˚C and changes to a nano-feature like morphology without dimples at 600 ˚C as can be seen from the SEM image in Fig. 46 which shows the primary fracture surfaces of the L-T orientation at different temperatures. Therefore, the fracture surfaces reflect the trend of J_{IC} with temperature.

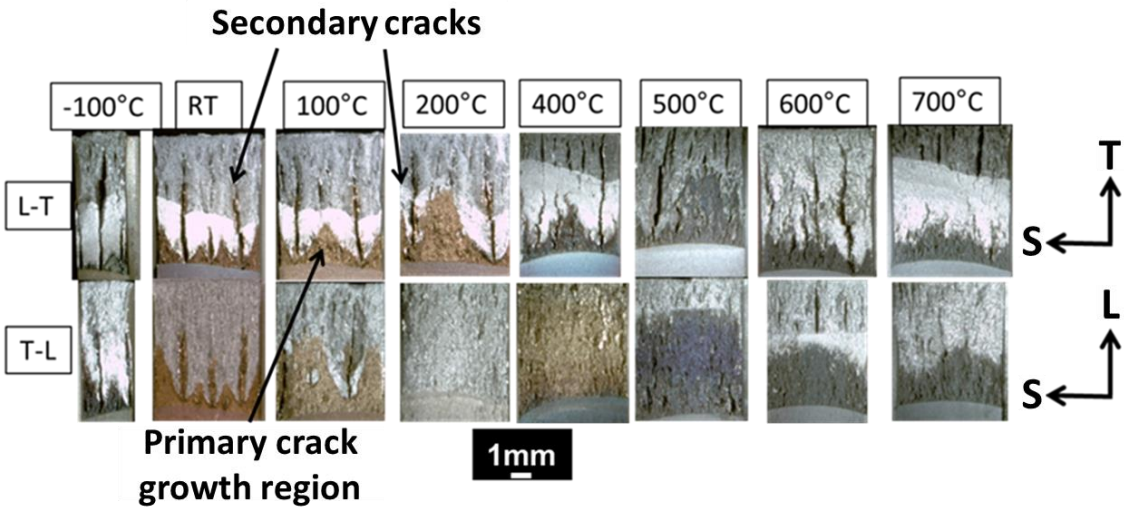

Fig. 42 Stereo microscope images of ODS-KIT HR fracture surfaces at different temperatures and orientations exhibiting secondary cracking.

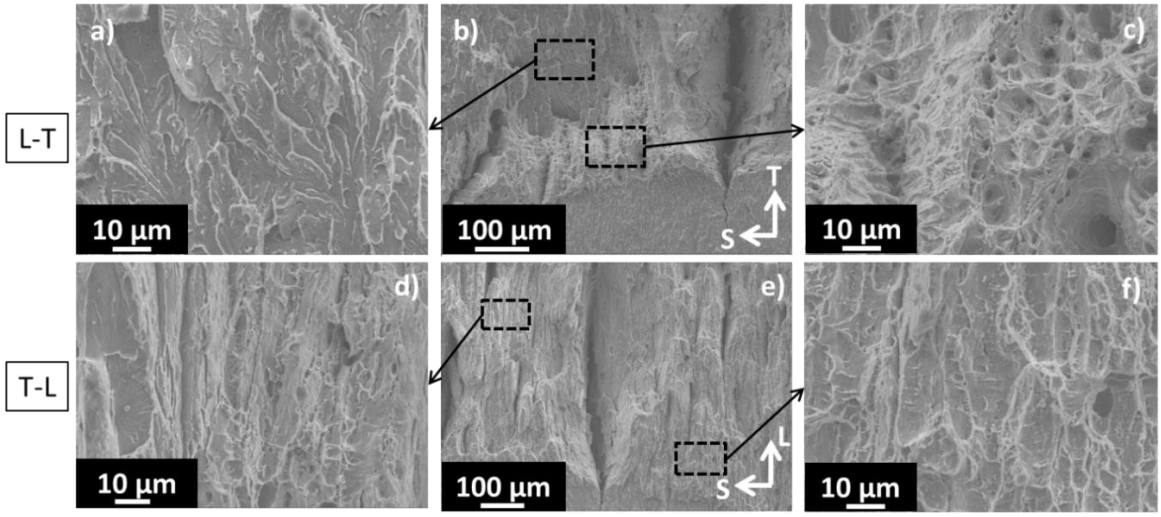

Fig. 43 SEM images of the fracture surfaces at -100 ˚C showing cleavage and ductile fracture in the (a-c) L-T oriented specimen and the (d-f) T-L oriented specimen of ODS-KIT HR.

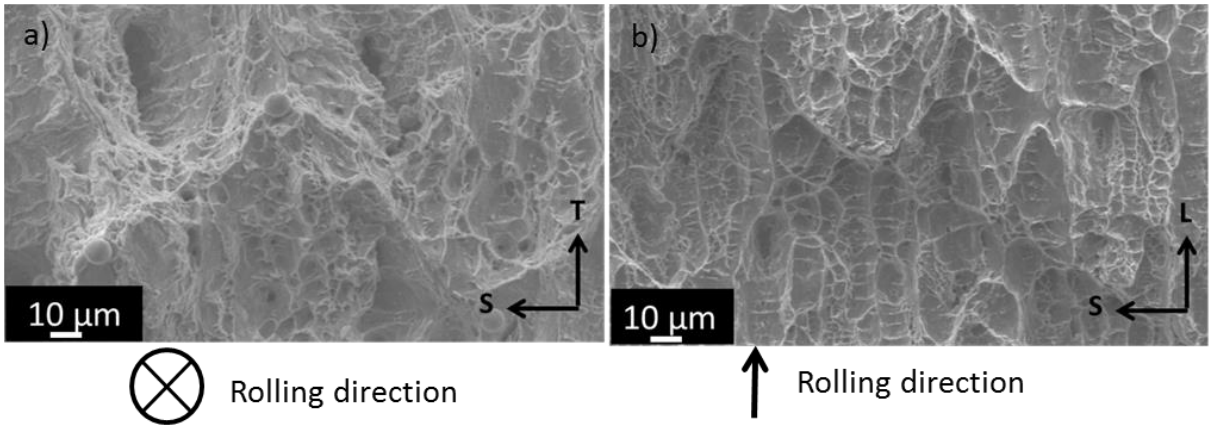

Fig. 44 SEM images of the fracture surfaces at RT showing equiaxed dimples in (a) L-T oriented specimen and flat dimples in (b) T-L oriented specimen of ODS-KIT HR.

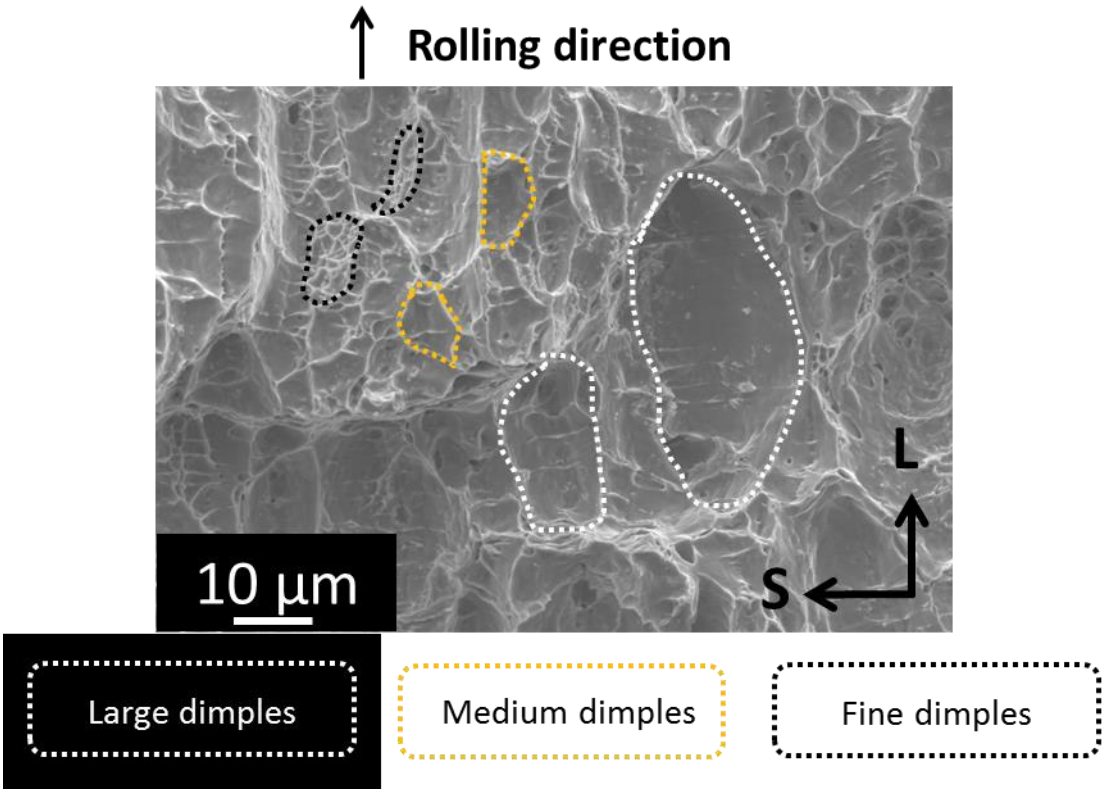

Fig. 45 SEM fracture surface image of ODS-KIT HR at 100 ˚C in the T-L orientation. Three different zones of dimples with different sizes are observed.

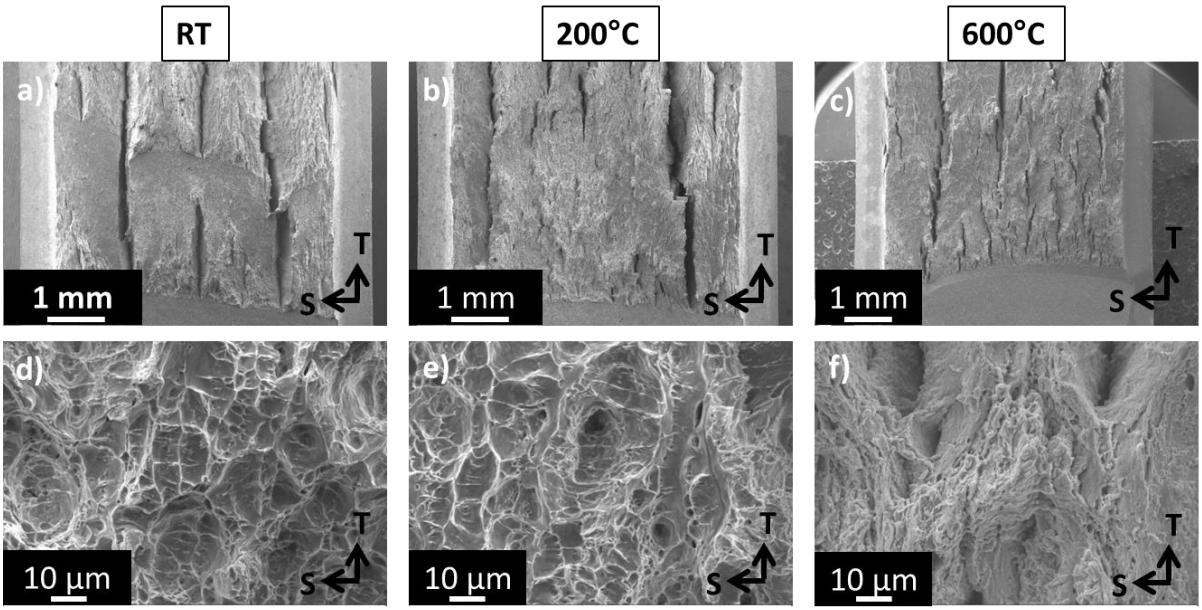

Fig. 46 SEM images of the fracture surfaces in the L-T orientation at (a and d) RT, (b and e) 200 ˚C and (c and f) 600 ˚C of ODS-KIT HR.

Secondary cracks

The secondary cracks in the L-T oriented sample were broken apart at various temperatures according to the cutting scheme in Fig. 16 and investigated using SEM. They are presented in Fig. 47. At RT, the presence of a predominantly cleavage fracture surface with some regions of dimples is observed (Fig. 47a, b and c). At 200 ˚C, dimples (Fig. 47d, e and f) and at 600 ˚C, nano-features without dimples are predominantly observed on the fracture surface (Fig. 47g, h and i).

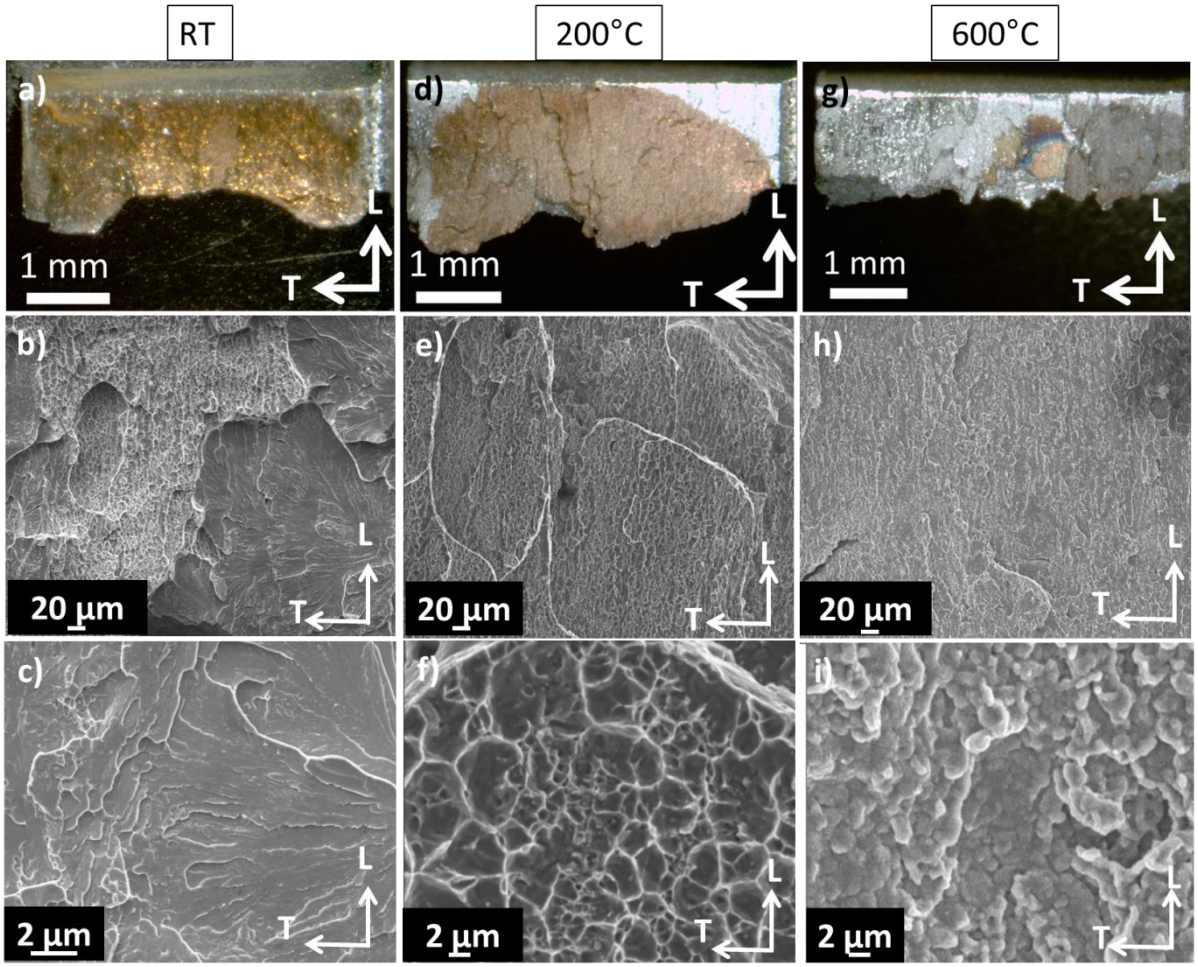

Fig. 47 Stereo microscope and SEM images of the secondary crack fracture surfaces of ODS-KIT HR at (a-c) RT, (d-f) 200 ˚C and (g-i) 600 ˚C.

4.4.2 ODS-KIT HE

The fracture surfaces in hot-extruded materials comprise of a rather uniform crack growth region with minor or no secondary cracking at all temperatures and orientations as can be seen from the stereo microscopic images in Fig. 48. Unstable primary crack growth was observed at RT for the C-R and C-L orientations.

Fracture morphology with features parallel to the extrusion direction is observed at RT for various orientations as seen from the SEM images in Fig. 49. The fracture surface in the L-C orientation predominantly exhibits regions with dimples and occasional flat regions (Fig. 49d) while predominant cleavage fracture with flat surfaces and occasional ductile tearing with dimples are observed in the C-R and C-L orientations at RT (Fig. 49e and f) similar to what was reported in reference [109]. High magnification SEM images of fracture surfaces of differently oriented specimens at different temperatures are presented in Fig. 50. Steps and ridges characteristic of cleavage fracture at RT in the C-R and C-L orientations can also be found in Fig. 50e and i. The fracture surfaces at 200 ˚C and 400 ˚C exhibit dimples characteristic of ductile fracture (Fig. 50a, b, c, f, g, j and k). At 600 ˚C, particle like nano-

features devoid of dimples which are characteristic of intergranular fracture are observed (Fig. 50d, h and l). Such nano-features on the fracture surface were also observed in other works [66,68,97,98].

In the ductile regime (T ≥ 200 ˚C), the fracture surface consists of flat regions of large dimples, medium dimples (mean size 3.2 µm) and fine dimples (mean size 0.7 µm) as can be seen from the SEM image of the fracture surface in the C-R orientation tested at 200 °C (Fig. 51). On the macro scale, at 400 ˚C, the fracture surface exhibits deeper grooves and is more undulating as compared with 200 ˚C. Flat and large dimples, seen on the fracture surface at 200 ˚C become deeper and less flat at 400 ˚C (Fig. 52d and e). At 600 ˚C, the fracture surface looks the flattest and no dimples are seen (Fig. 52f).

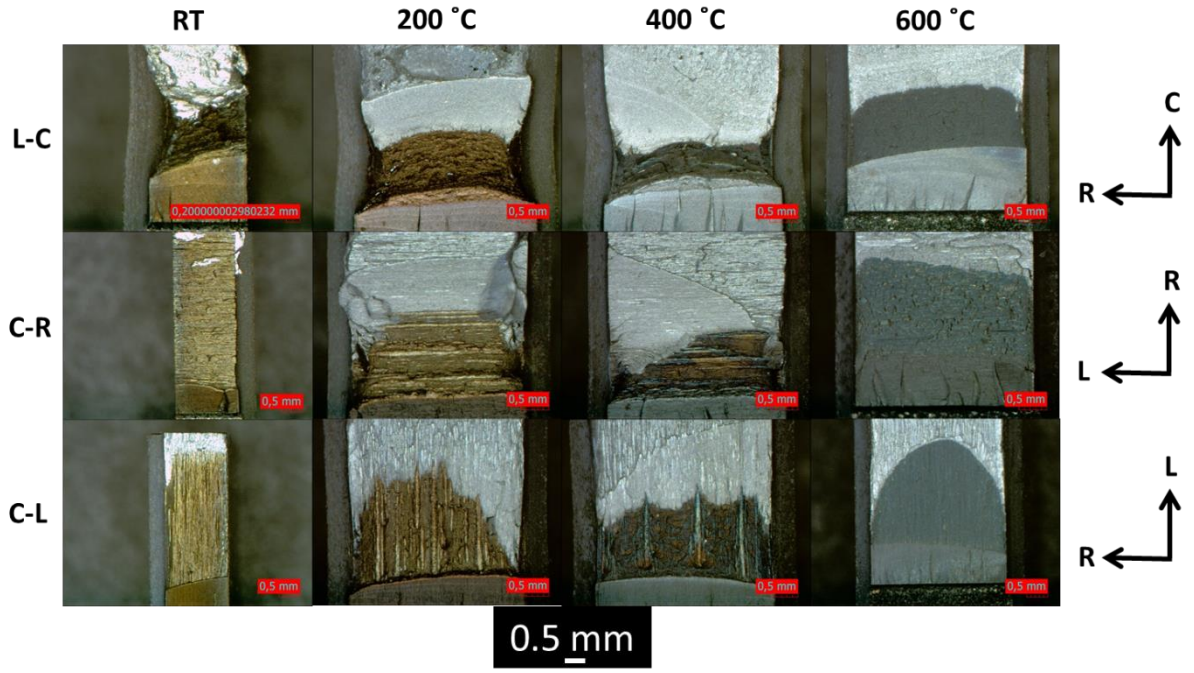

Fig. 48 Stereo microscope images of the ODS-KIT HE fracture surfaces in different orientations and at different temperatures.

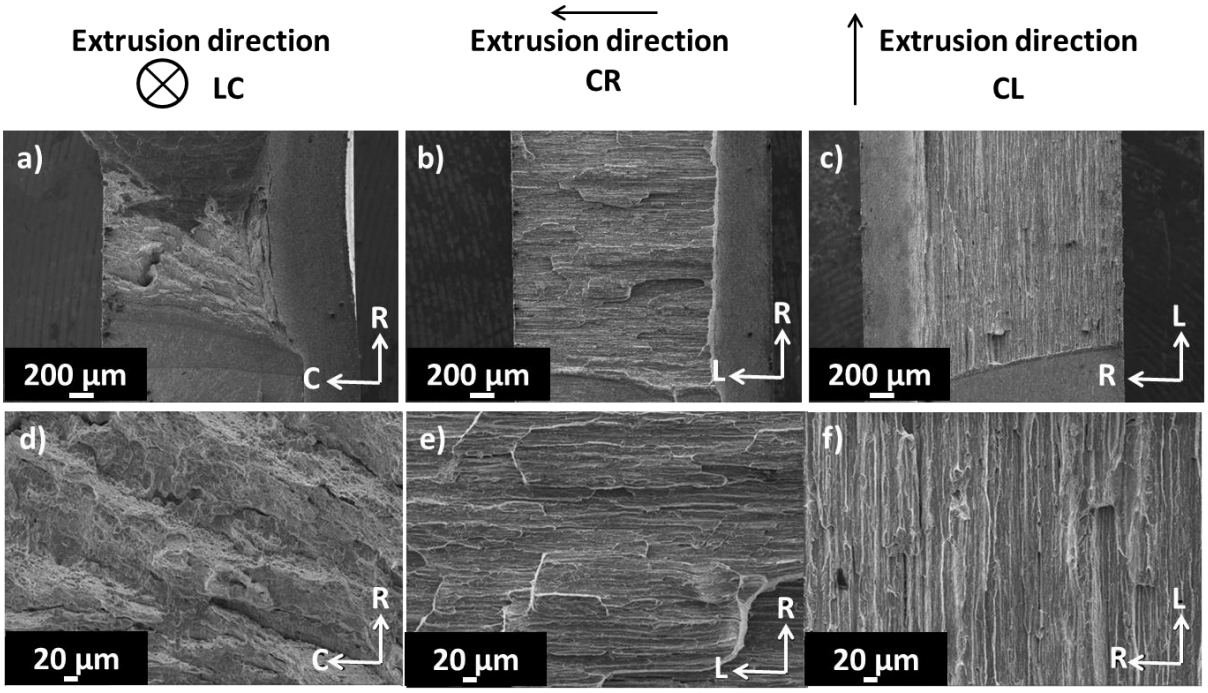

Fig. 49 Low (a-c) and high (d-f) magnification SEM images of the fractures surfaces at RT in different orientations of ODS-KIT HE.

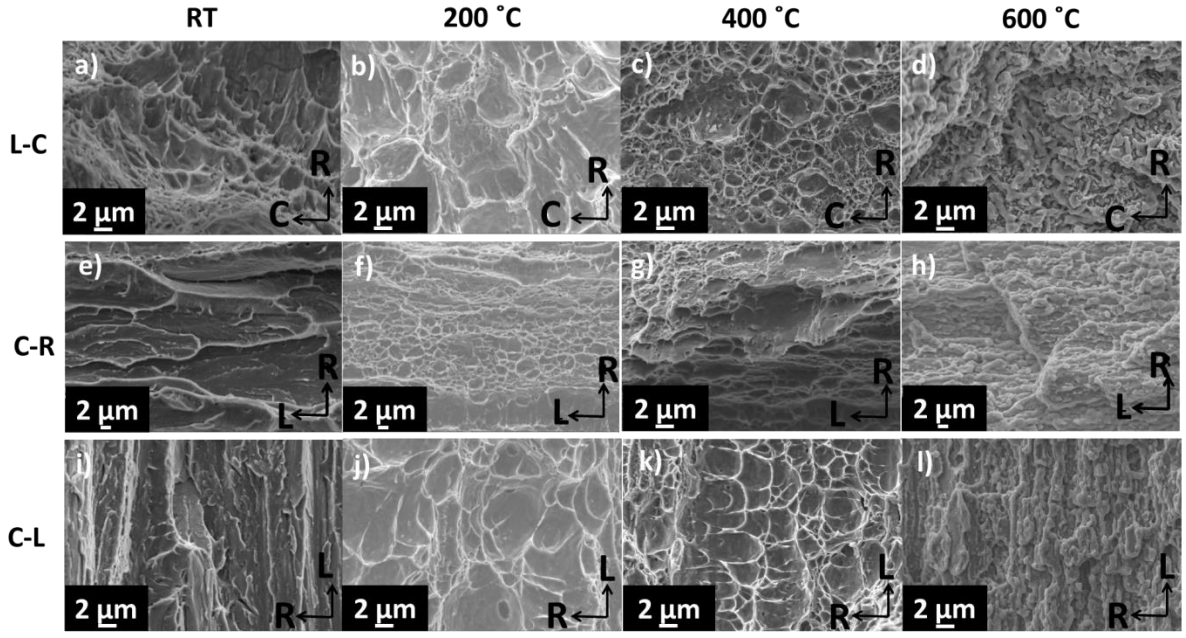

Fig. 50 High magnification SEM images of the fracture surfaces in the L-C (a-d), C-R (e-h) and C-L orientations (i-l) at different temperatures of ODS-KIT HE.

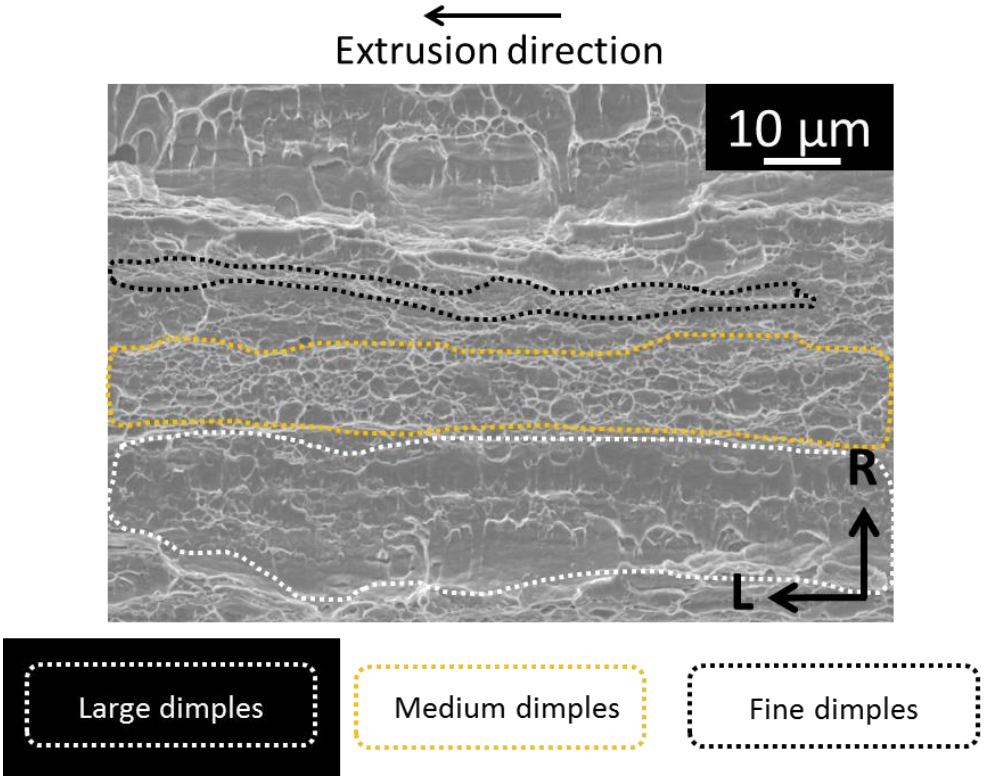

Fig. 51 SEM fracture surface image of ODS-KIT HE at 200 ˚C in the C-R orientation. Three different zones of dimples with different sizes are observed.

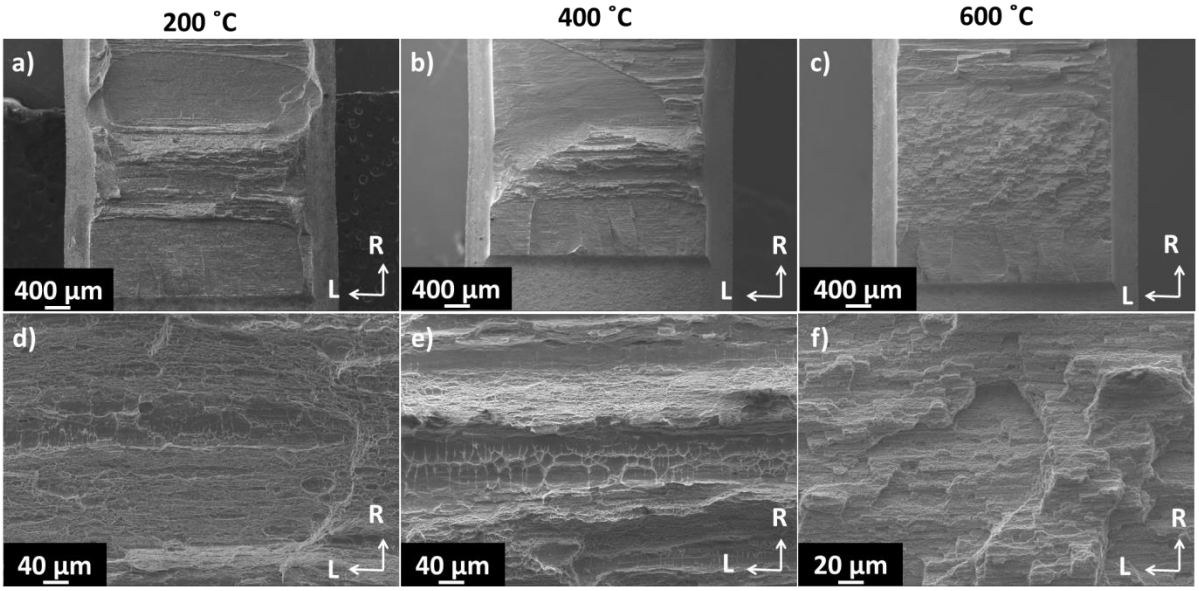

Fig. 52 Fracture surfaces of the C-R oriented specimens at 200 ˚C (a and d), 400 ˚C (b and e) and 600 ˚C (c and f) of ODS-KIT HE.

Secondary cracks

A partially formed secondary crack which is arrested by the surrounding microstructure can be seen on the SEM image of the fracture surface of the L-C oriented sample at RT (Fig. 53**)**. The other orientations exhibit minor or no secondary cracking. Secondary cracks as extensive as in ODS-KIT HR are not observed.

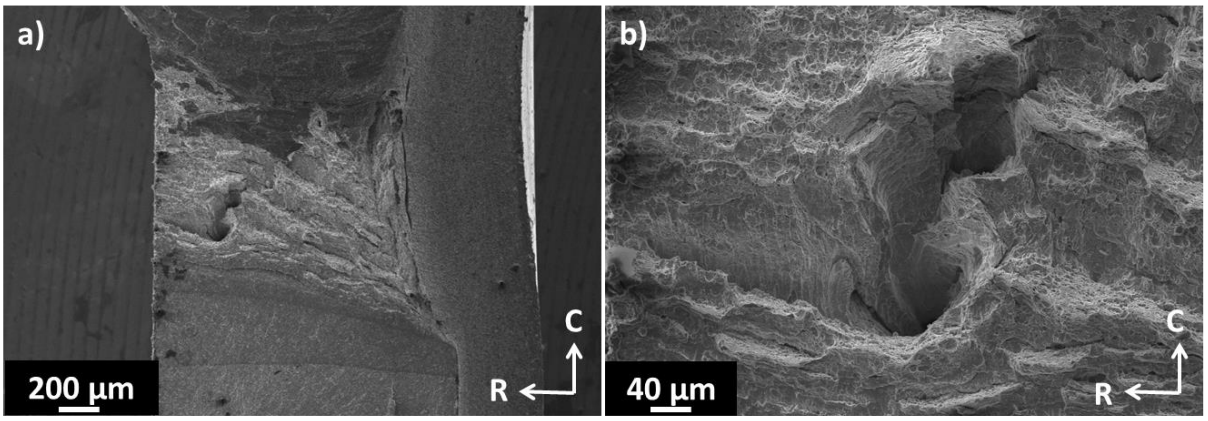

Fig. 53 SEM image showing an arrested secondary crack in a) low magnification and b) high magnification in the L-C oriented specimen of ODS-KIT HE at RT.

4.4.3 ODS-CSM

The fracture surfaces in ODS-CSM comprise of a uniform crack growth region with minor or no secondary cracking at all temperatures and orientations as can be seen from the stereo microscopic images in Fig. 54. There was no instability in primary crack propagation in all the orientations at all temperatures.

Fracture morphology with features parallel to the extrusion direction is observed at RT for various orientations as seen from the SEM images in Fig. 55. The macro fracture surfaces in all the orientations at RT are undulating, the C-L orientation being the flattest (Fig. 55d-f). High magnification SEM images of the fracture surfaces of differently oriented specimens at different temperatures are presented in Fig. 56. Dimples, characteristic of ductile fracture are observed from RT to 400 ˚C in all the orientations (Fig. 56a, b, c, e, f, g, i, j and k). Arrows indicate the sub-micron particles which were found inside the dimples (Fig. 56e). Nano-features with no dimples, characteristic of intergranular fracture, are observed at 600 °C in all the orientations (Fig. 56d, h and l).

In the ductile regime (T ≥ RT), similar regions as in ODS-KIT HE are observed; containing fine dimples (mean size 0.7 µm) and medium dimples (mean size 1.1 µm) as can be seen on the fracture surface in C-R orientation at RT (Fig. 57). The large dimples in ODS-CSM however, are not as large as in ODS-KIT HE. Low magnification SEM images of the primary fracture surface from the C-R oriented specimen at different temperatures are presented in Fig. 58. Undulating fracture morphology is observed from RT up to 600 ˚C. Unlike ODS-KIT HE, the undulation of fracture surface does not flatten drastically between 400 ˚C and 600 ˚C (Fig. 58g and h).

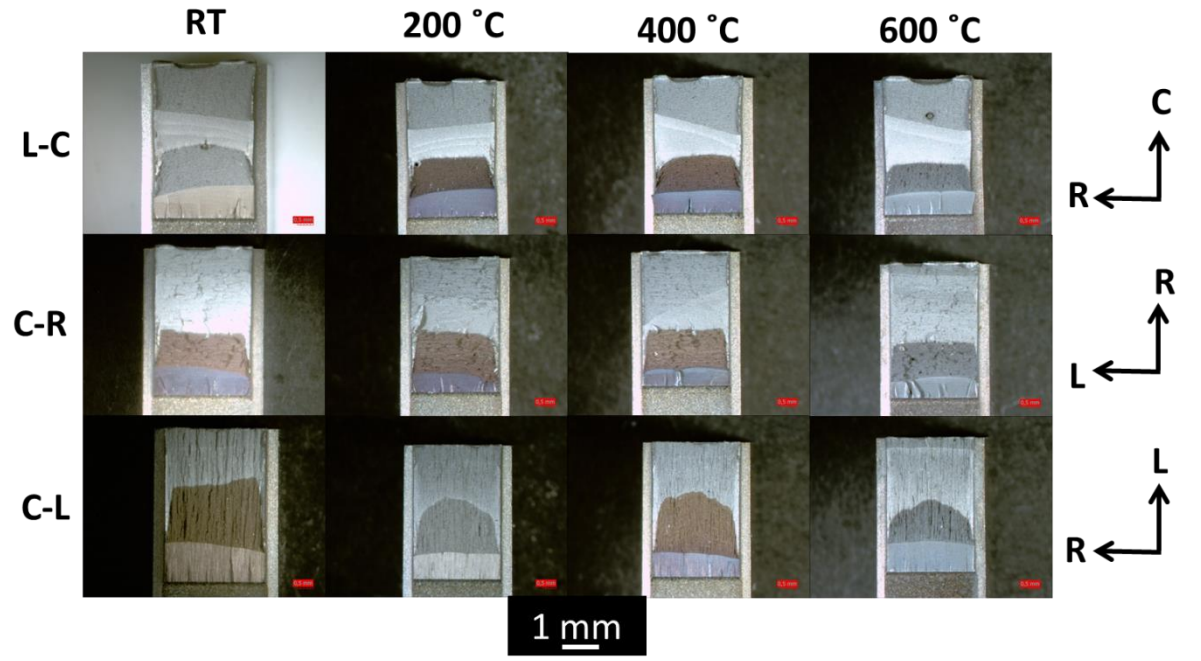

Fig. 54 Stereo microscope images of the ODS-CSM fracture surfaces in different orientations and at different temperatures.

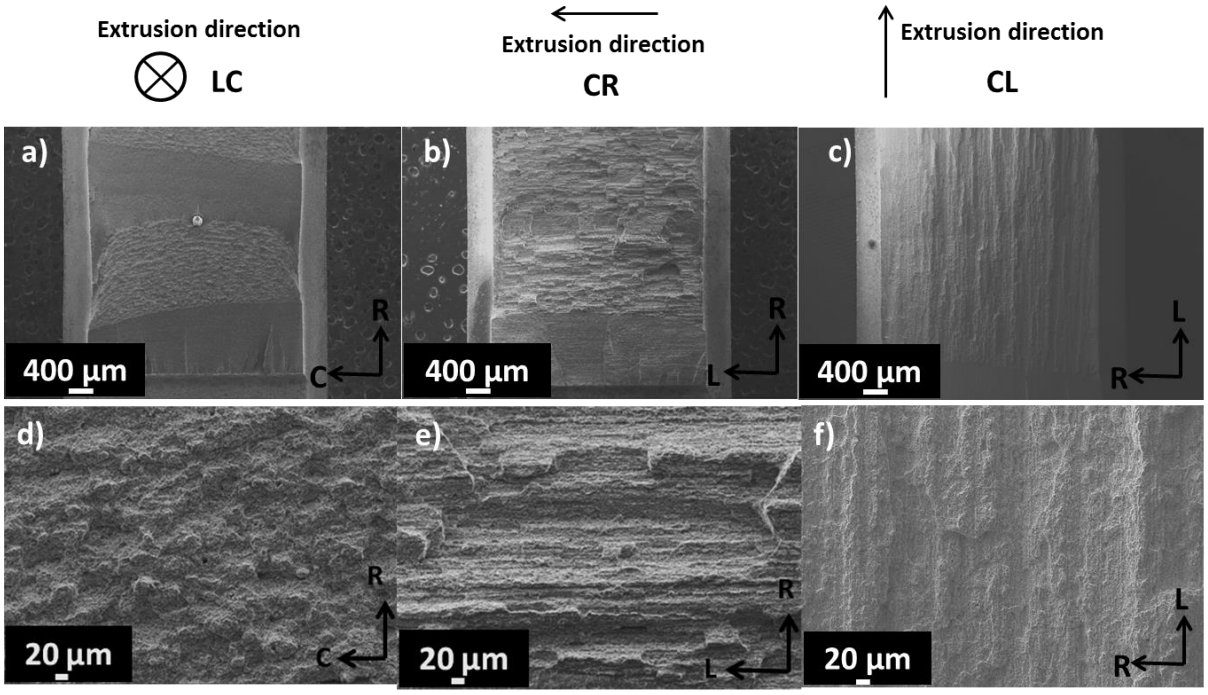

Fig. 55 Low (a-c) and high (d-f) magnification SEM images of the fractures surfaces at RT in different orientations of ODS-CSM.

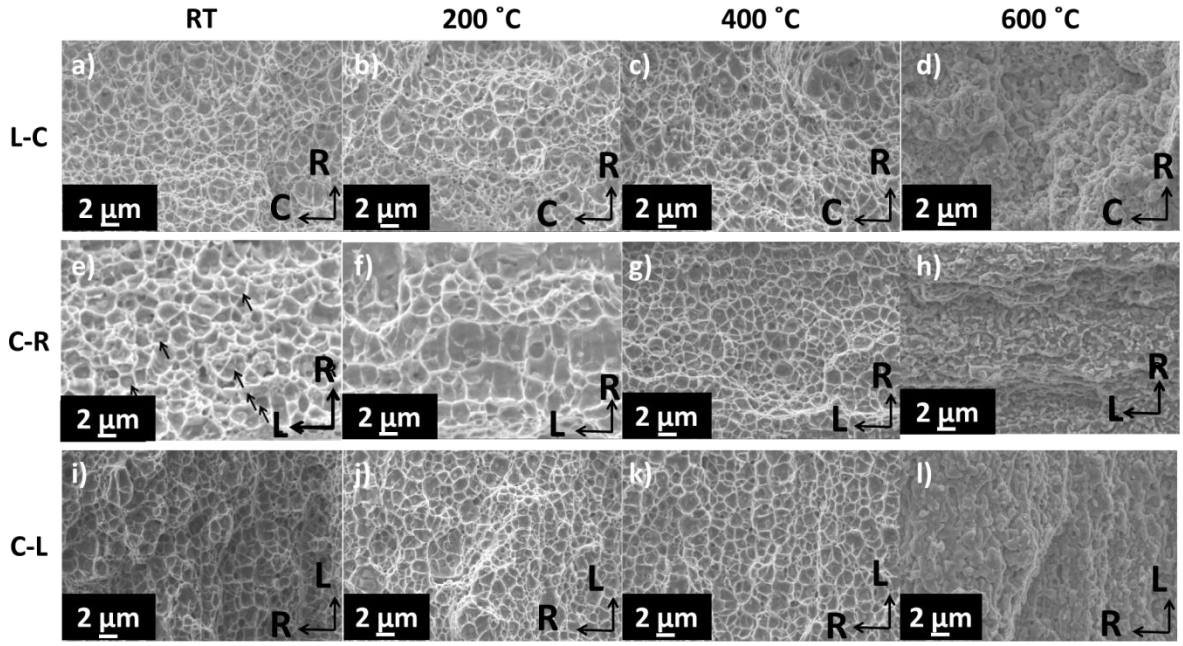

Fig. 56 High magnification SEM images of the fracture surfaces in the L-C (a-d), C-R (e-h) and C-L oriented specimens (i-l) of ODS-CSM at different temperatures.

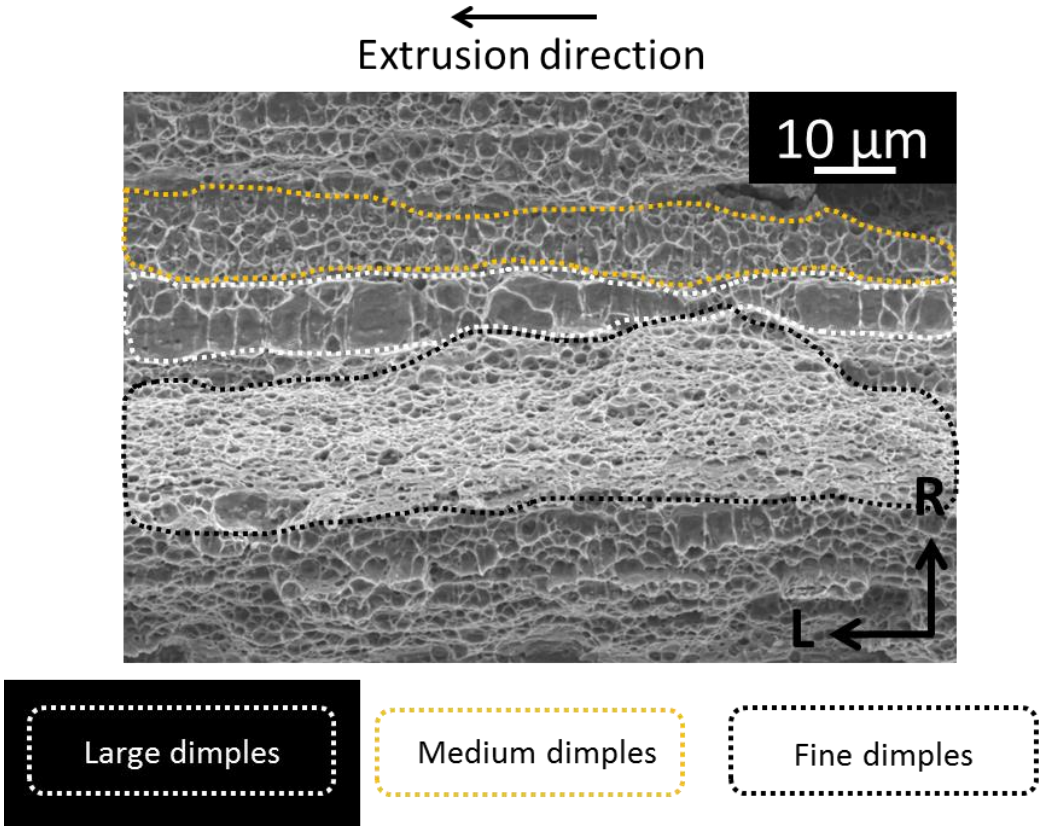

Fig. 57 SEM fracture surface image of ODS-CSM at RT in the C-R orientation. Three different zones of dimples with different sizes are observed.

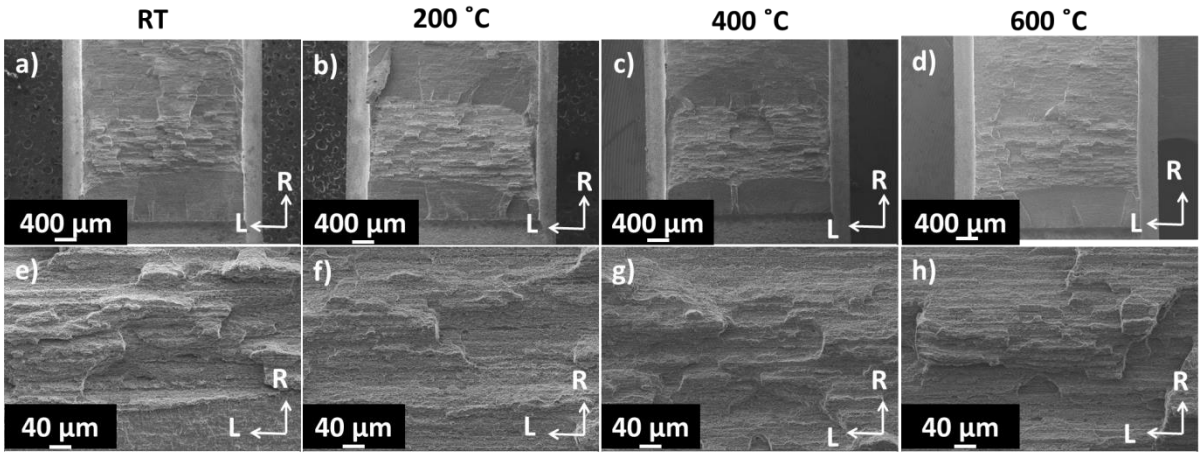

Fig. 58 Fracture surfaces of the C-R oriented specimens at RT (a and e), 200 ˚C (b and f), 400 ˚C (c and g) and 600 ˚C (d and h) of ODS-CSM.

Secondary cracks

Secondary cracks as extensive as in ODS-KIT HR are not observed. Only minor or no secondary cracking is observed in all the orientations. A small partially formed secondary crack is seen on the fracture surface of the specimen in the L-C orientation at RT which is arrested by the surrounding microstructure as can be seen in the SEM image in Fig. 59a and b.

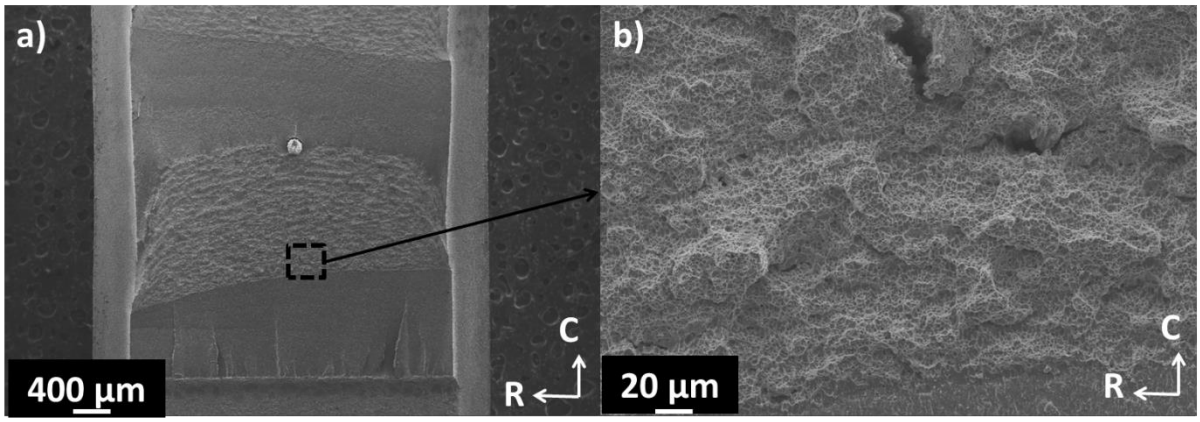

Fig. 59 SEM image showing an arrested secondary crack in a) low magnification and b) high magnification in the L-C oriented specimen of ODS-CSM at RT.

4.4.4 Summary

A non-uniform primary crack growth region is observed on the fracture surfaces of hot-rolled specimens with extensive secondary cracking while a uniform crack growth region is observed for hot-extruded specimens with minor or no secondary cracking. The extent of secondary cracking decreases with increase in temperature in hot-rolled specimens. Hot-rolled specimens exhibit more unstable primary crack propagation than hot-extruded specimen.

Fracture morphology with features parallel to the extrusion/rolling direction is observed for all the ODS steels in all the orientations. Cleavage facets mixed with ductile regions are observed at or below

RT. Predominant dimple regions are found on the fracture surfaces of all the ODS steels between RT and 600 °C in most of the orientations. At and above 600 °C, nano-features without dimples are observed on the fracture surfaces of all the ODS specimens.

Another method of obtaining information about the fracture mechanisms is to study the crack propagation in a material. For this purpose, the results of the crack propagation investigation will be shared in the next section. Some questions pertinent for the next section are:

- Through which region of the microstructure do the cracks propagate?
- What mechanism does primary and secondary crack propagation follow?
- When do secondary cracks propagate with respect to primary cracks?
- Does secondary crack propagation exhibit orientation dependence?

4.5 Crack propagation

Side surfaces of the propagated primary and secondary cracks were investigated using OM, SEM and EBSD after fracture toughness testing. Polishing was sometimes deployed from the side surface to reach the middle of the crack front.

4.5.1 ODS-KIT HR

Primary cracks

The SEM images of the side surfaces of tested C(T) specimens are shown in Fig. 60. At RT, the amount of crack propagation for the L-T oriented specimen was 1 mm for a load line displacement of 1.02 mm while the amount of crack propagation for the T-L oriented specimen was 1.9 mm for a load line displacement of 0.52 mm. Pre-existing pores perpendicular to the crack propagation direction are observed in the L-T orientation while they are observed parallel to the crack propagation direction in the T-L orientation as can be seen from the polished and etched OM images in Fig. 61. The crack tip in the L-T oriented specimen looks blunted and has a larger radius (Fig. 61a) than the crack tip in the T-L oriented specimen (Fig. 61b).

The primary crack appears to propagate preferentially through UFGs as seen in the EBSD grains distribution map of the primary crack in Fig. 62. It is seen that the primary crack propagation direction is perpendicular to the arranged and elongated grains in the L-T orientation (Fig. 62a) while the crack propagation direction is parallel to them in the T-L orientation (Fig. 62b). In both the L-T and T-L orientations, the primary crack branches out in a direction parallel to rolling direction (L direction) as seen from the magnified EBSD images of the selected regions (Fig. 62c - f).

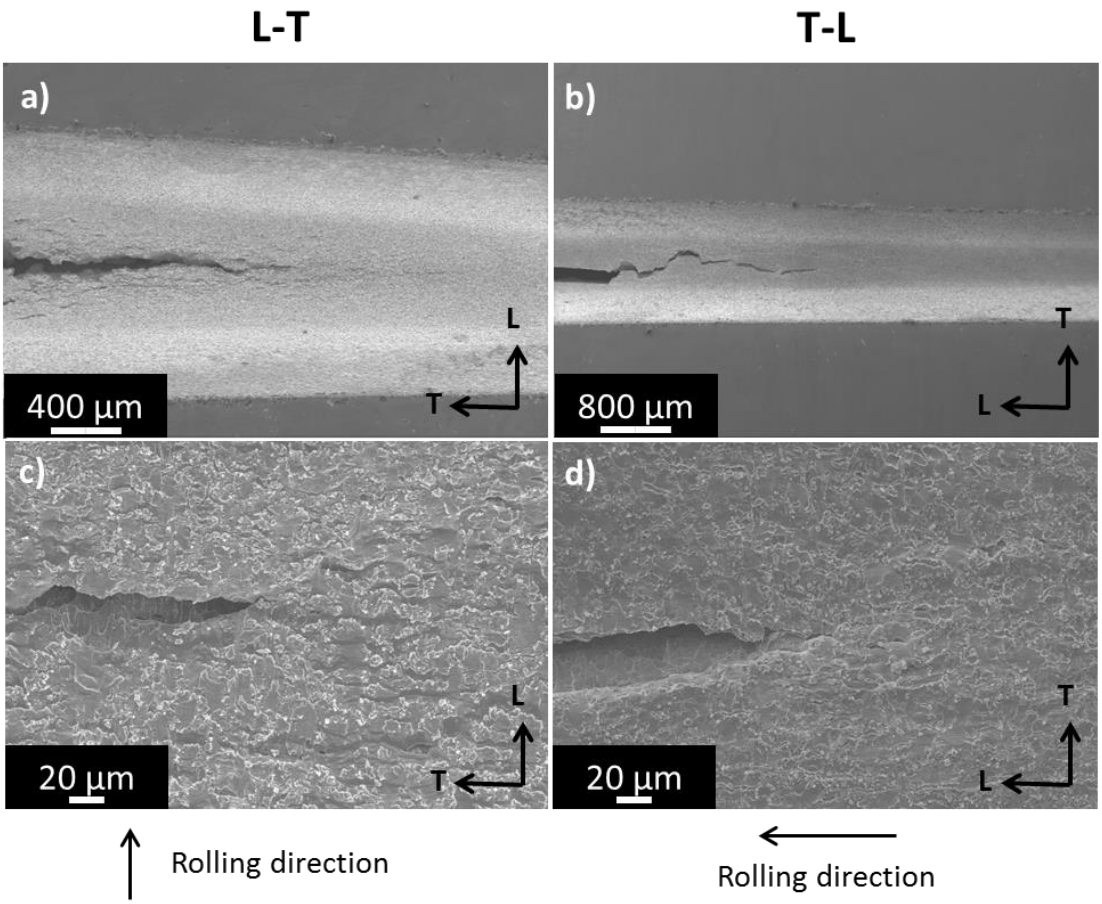

Fig. 60 Side view of the propagated crack in ODS-KIT HR after fracture toughness testing in different orientations at RT using SEM on the sample side surface.

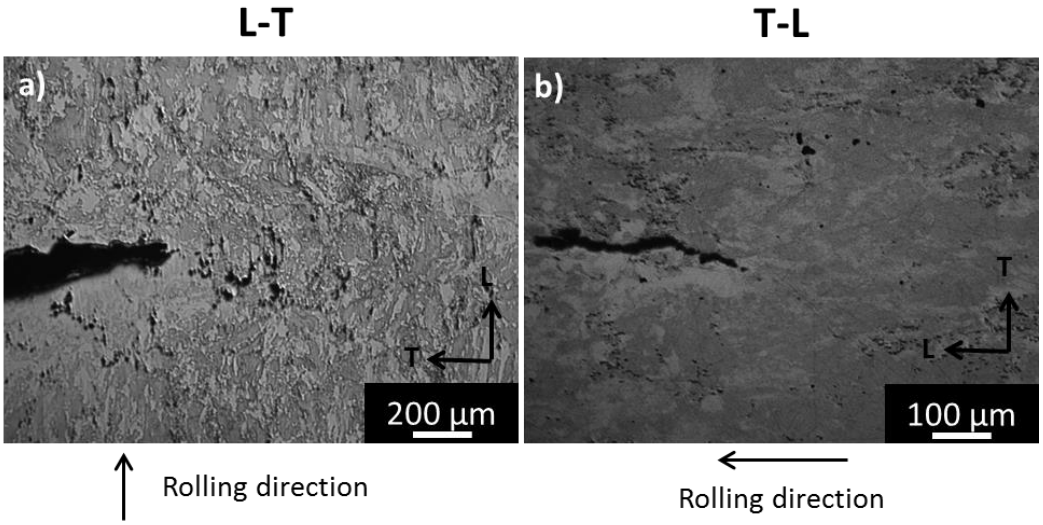

Fig. 61 Side view of the propagated crack close to the crack front middle after fracture toughness testing in different orientations of ODS-KIT HR at RT using optical microscope on polished and etched samples.

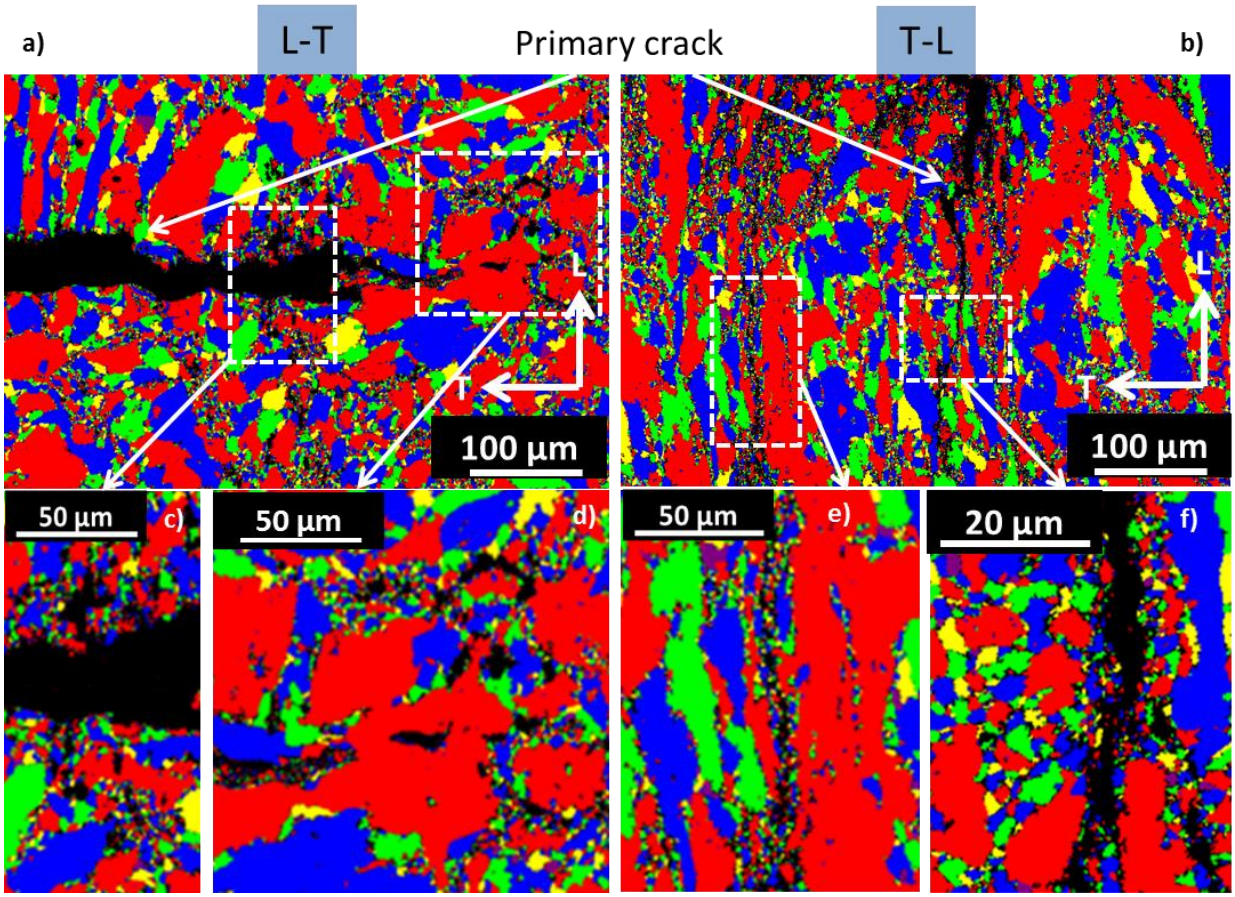

Fig. 62 EBSD grain distribution map of the a) L-T and (b) T-L oriented specimen of ODS-KIT HR showing primary crack growth with respect to arranged and elongated grains. Images (c-f) show the magnified regions from images (a) and (b) indicating crack branching.

Secondary cracks

Interrupted fracture toughness test were performed on a T-L oriented specimen, which was loaded in the elastic range at RT. The sample was then cut apart in the same plane as the primary crack plane and polished. Secondary cracks were observed on the primary crack plane. The secondary cracks initiated even before primary crack growth took place as can be seen from the stereo microscopic image in Fig. 63 (marked by arrows).

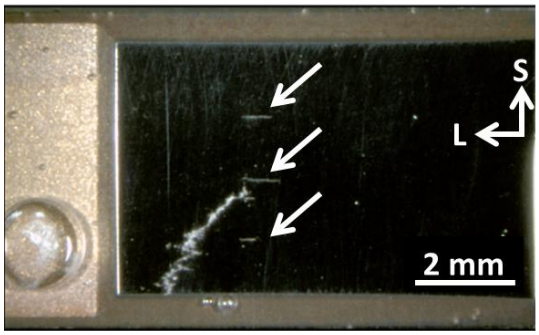

Fig. 63 The fracture surface after an interrupted fracture toughness test on the T-L oriented specimen of ODS-KIT HR at RT. Arrows indicate the presence of secondary cracks before the growth of primary crack.

Secondary crack depths of the L-T and T-L oriented specimens tested at 100˚C were measured using an optical microscope after sectioning and polishing the LS and TS planes, respectively, at every 0.5 mm secondary crack length. A schematic showing secondary crack length and depth of an L-T oriented specimen is presented in Fig. 64. Cumulative crack depths (i.e. including all secondary cracks) were measured. The secondary crack depths are not constant over the length of the secondary crack and reach a maximum at 2.5 mm secondary crack length (marked in Fig. 64c). The OM image of the secondary crack depth plane for the L-T and T-L specimens at 2.5 mm secondary crack length is also shown in Fig. 64a and b, respectively. It is observed that the number and cumulative depth of secondary cracks in the L-T orientation was greater than in the T-L orientation. It is noteworthy that, the integral of the curves in Fig. 64c represent one half of the total fracture surface area formed for all the secondary cracks.

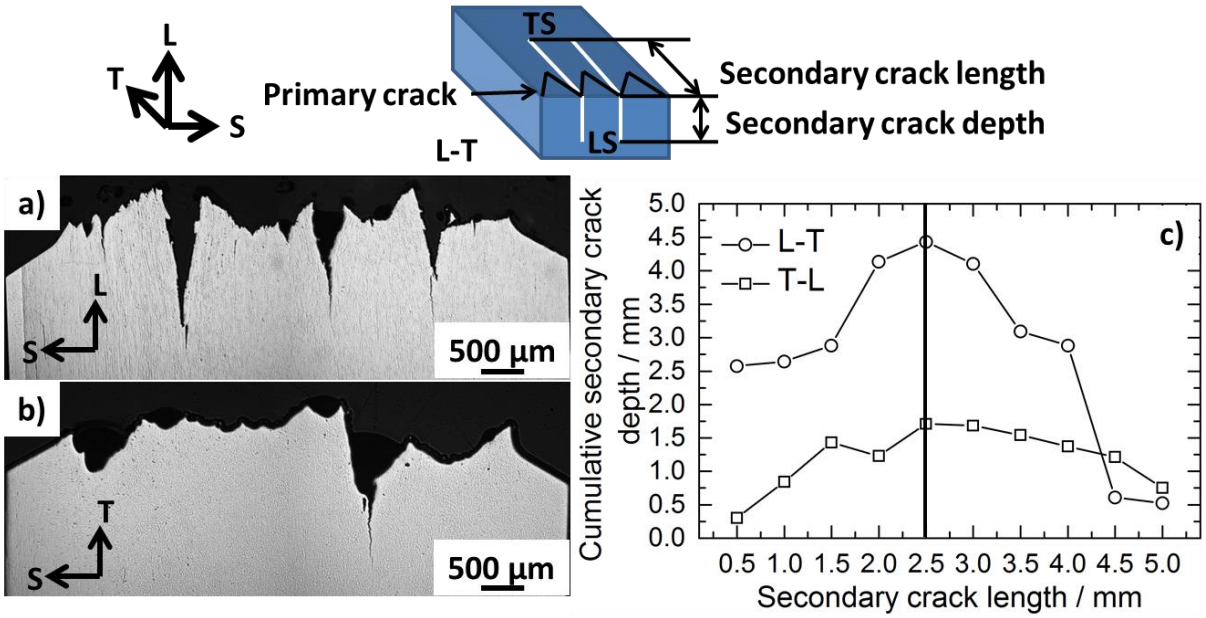

Fig. 64 Optical microscope image showing secondary crack depths at the 2.5 mm secondary crack length section at 100 ˚C in the a) L-T and b) T-L oriented specimen of ODS-KIT HR. c) Shows the graph between cumulative secondary crack depth and secondary crack length for both the orientations. The maximum crack depths are reached at 2.5 mm crack length (marked in c and shown in a and b)

EBSD IPF maps (x, y and z) of the TS plane (a plane parallel to the primary crack plane and containing a secondary crack) at RT and LS plane (a plane perpendicular to both the primary and secondary crack plane and containing a secondary crack) at 600 ˚C for a L-T oriented specimen are shown in Fig. 65 and Fig. 66, respectively. Three line scans were performed for the crack at RT (Fig. 65e) and two for the crack at 600 °C (Fig. 66d). The misorientation line scans with respect to the immediately previous point indicates that at RT, there are several locations across the crack where the misorientation angle changes by 5 degrees or less (two of which are presented as line scan 1 and 2 in Fig. 65). Line scan 1 is magnified in Fig. 65d. There are also few locations, where the misorientation angle changes

by more than 15 degrees (e.g. line scan 3 in Fig. 65). At 600 °C, locations of low misorientation across the secondary crack (< 5°) are not observed and only high misorientations exists (Fig. 66). The situation was found to be similar for T-L oriented specimens at both the temperatures.

With respect to the morphology of the secondary crack as seen from the side surface, the crack edges at RT appear straighter with sharper features than at 600 °C. Similar sharp features were also observed for other ODS-KIT HR specimens at similar testing conditions close to RT.

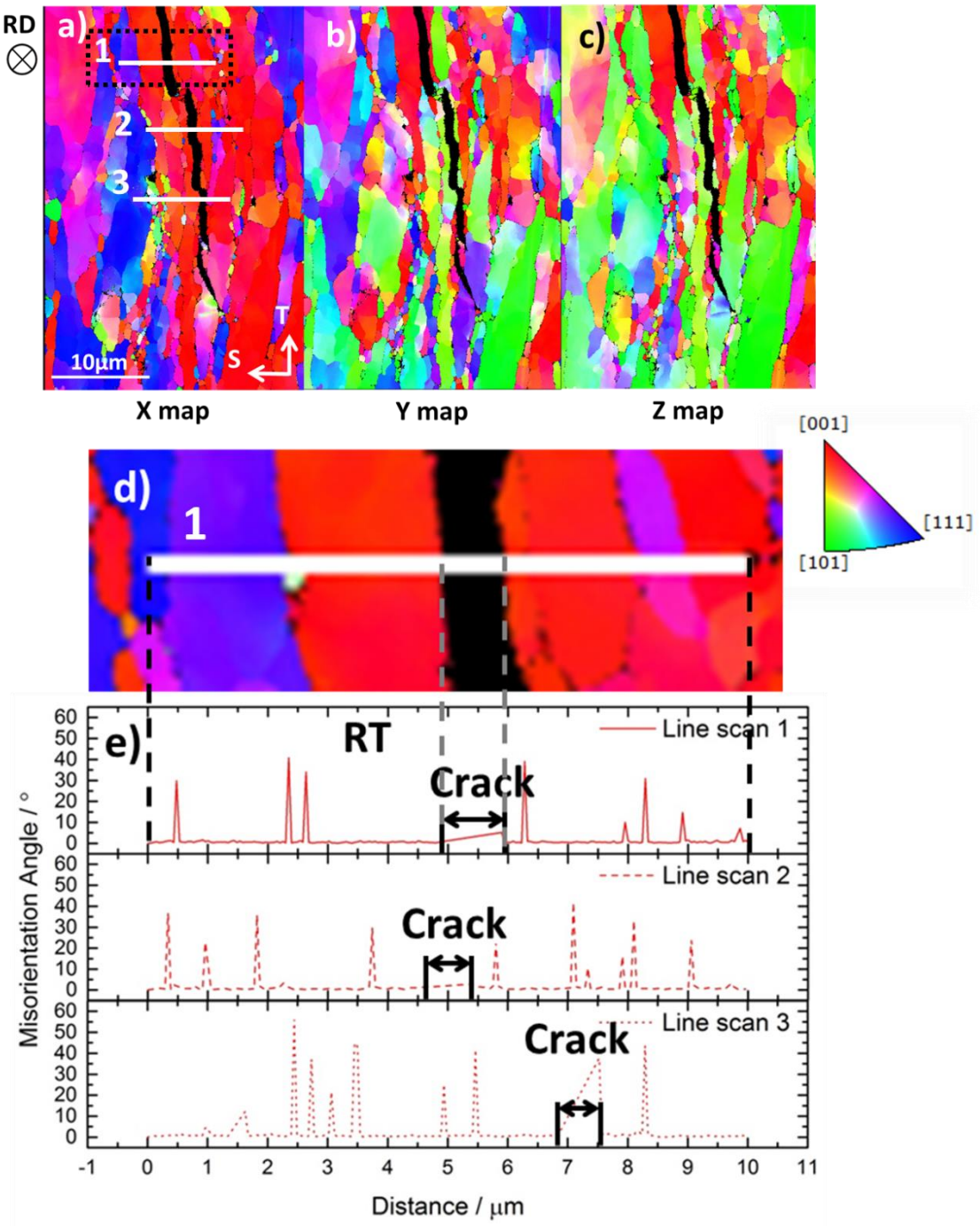

Fig. 65 Misorientation line scan across a secondary crack in an L-T oriented specimen of ODS-KIT HR using EBSD IPF maps of TS plane at RT. Line scan 1 is magnified and the corresponding misorientation versus distance graph is displayed.

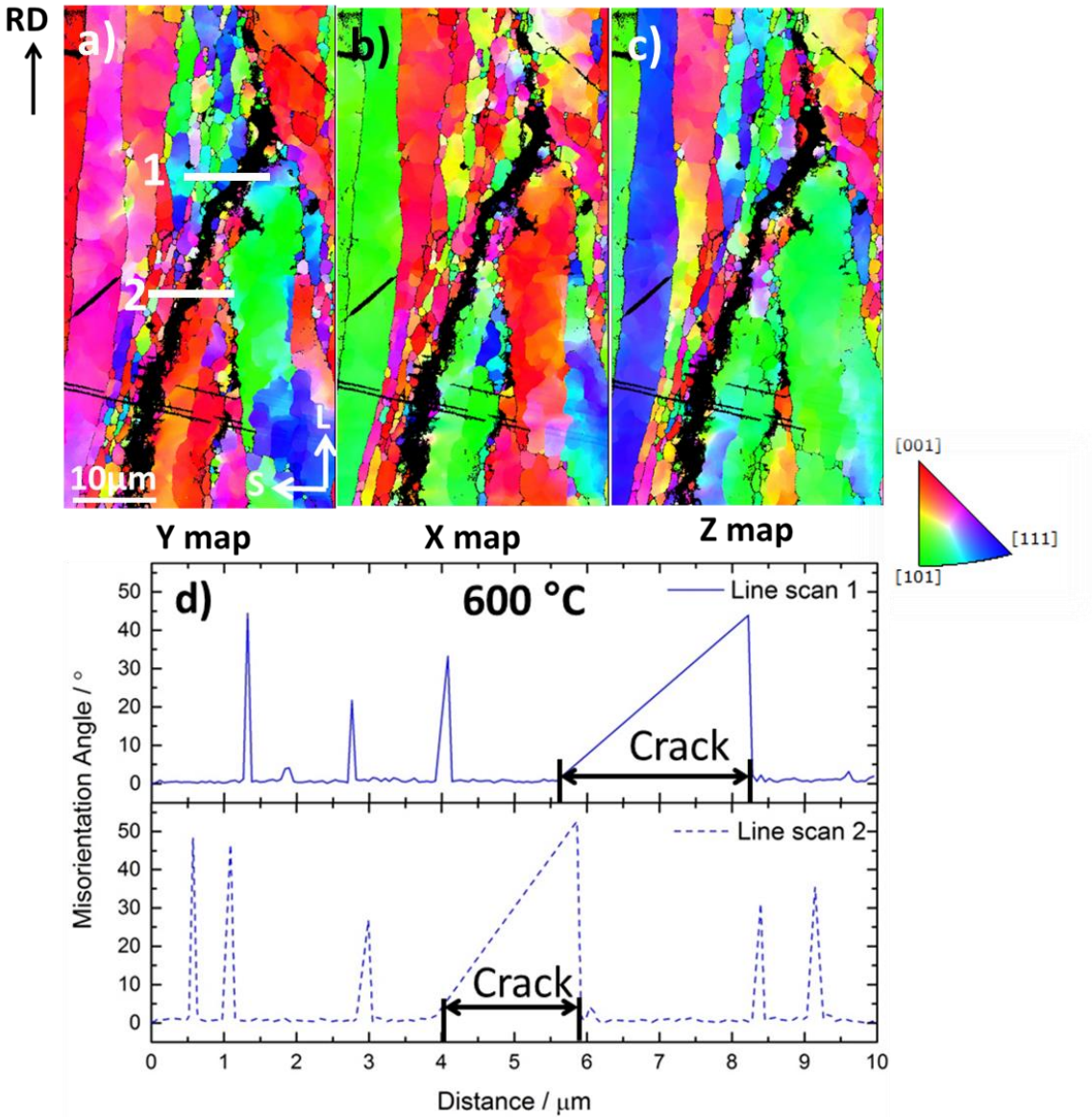

Fig. 66 Misorientation line scan across a secondary crack in an L-T oriented specimen of ODS-KIT HR using EBSD IPF maps of LS plane at 600 °C

4.5.2 ODS-KIT HE

The SEM images of the side surfaces of tested C(T) specimens are shown in Fig. 67. At RT, the amount of crack propagation for the L-C oriented specimen was 0.92 mm for a load line displacement of 1.61 mm, the amount of crack propagation for the C-R oriented specimen was 3.8 mm for a load line displacement of 0.27 mm and the amount of crack propagation for the C-L oriented specimen was 3 mm for a load line displacement of 0.19 mm. Note that there was unstable crack propagation in the C-R and C-L oriented specimens at RT. Morphological fracture features parallel to the extrusion direction can be seen in the high magnification SEM images in Fig. 67d-f.

In the C-L oriented specimen, there is minimal crack deviation and the crack appears to propagate preferentially through the UFGs as seen from the EBSD grain distribution map containing the primary crack as presented in Fig. 68. In the L-C orientation, the crack during propagation gets obstructed by

the perpendicularly elongated coarse grains (Fig. 68b). Some regions of crack branching are also observed stemming out from the primary crack in the direction of extrusion.

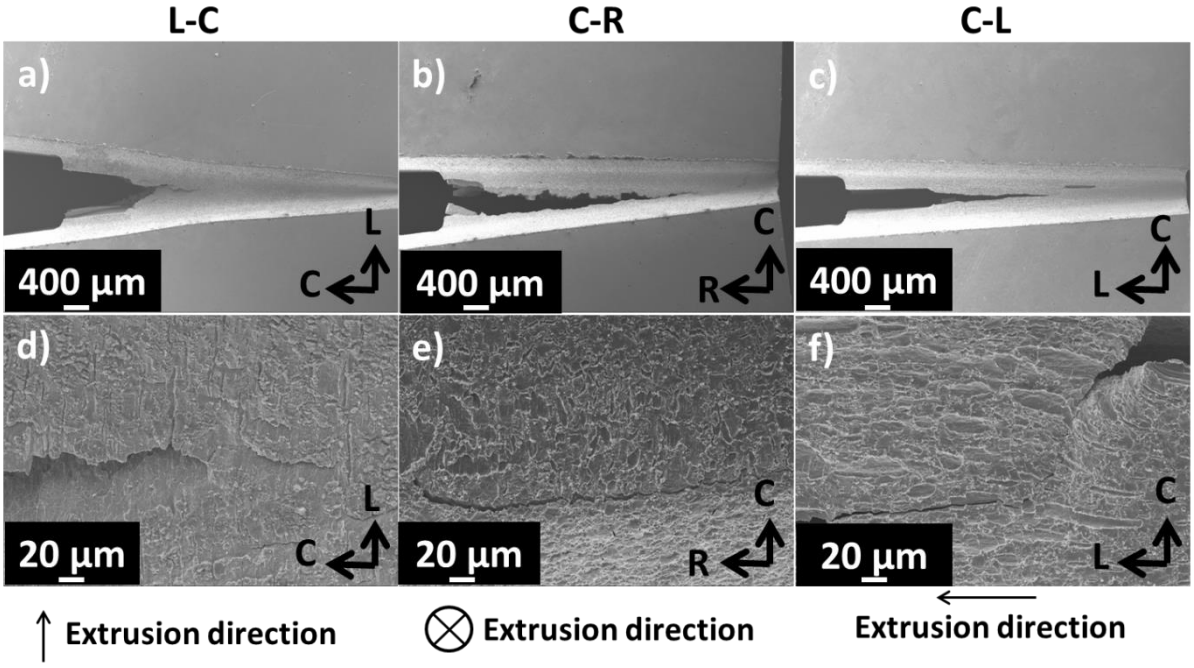

Fig. 67 Side view of the propagated crack after fracture toughness testing in different orientations of ODS-KIT HE at RT.

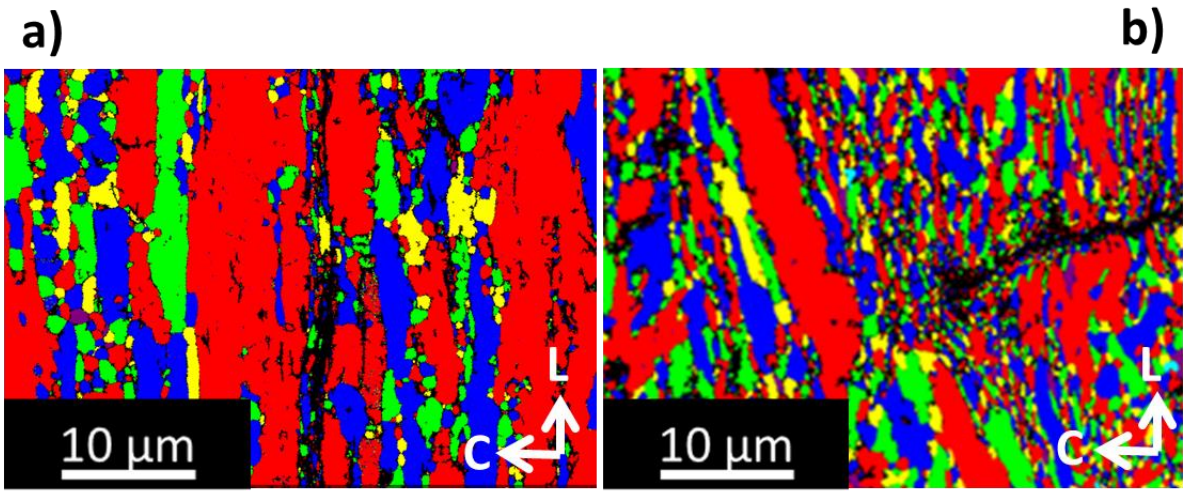

Fig. 68 EBSD grain distribution map of the a) C-L and b) L-C oriented specimen of ODS-KIT HE showing side view of the primary crack growth with respect to the arranged and elongated grains.

4.5.3 ODS-CSM

The SEM images of the side surfaces of tested C(T) specimens are shown in Fig. 69. At RT, the amount of crack propagation for the L-C oriented specimen was 1.24 mm for a load line displacement of 0.35 mm, the amount of crack propagation for the C-R oriented specimen was 1.1 mm for a load line displacement of 0.28 mm and the amount of crack propagation for the C-L oriented specimen was

1.8 mm for a load line displacement of 0.13 mm. No unstable crack propagation was observed for all the orientations. Morphological fracture features parallel to the extrusion direction can be seen in the high magnification SEM images in Fig. 69d-f.

A large crack deviation close to the side surface of the C(T) specimen is observed for the L-C oriented specimen tested at 400 ˚C (Fig. 70a and b). Close to the middle of the crack front, the crack still appears to move in a zig-zag fashion but deviates less as compared to the side surface and generally propagates in a straight line (Fig. 70c and d). A higher magnification backscattered SEM image is presented in Fig. 70e which indicates that the crack propagation at this temperature is through void growth and coalescence.

Crack deviation through UFGs is observed in the EBSD grain distribution map containing a propagating crack in the C-R orientation (Fig. 71a). The primary crack propagation in the L-C orientation is perpendicular to the zones of coarse and fine grains (Fig. 71b) and crack deviation into a plane inclined 45˚ to primary crack plane is observed.

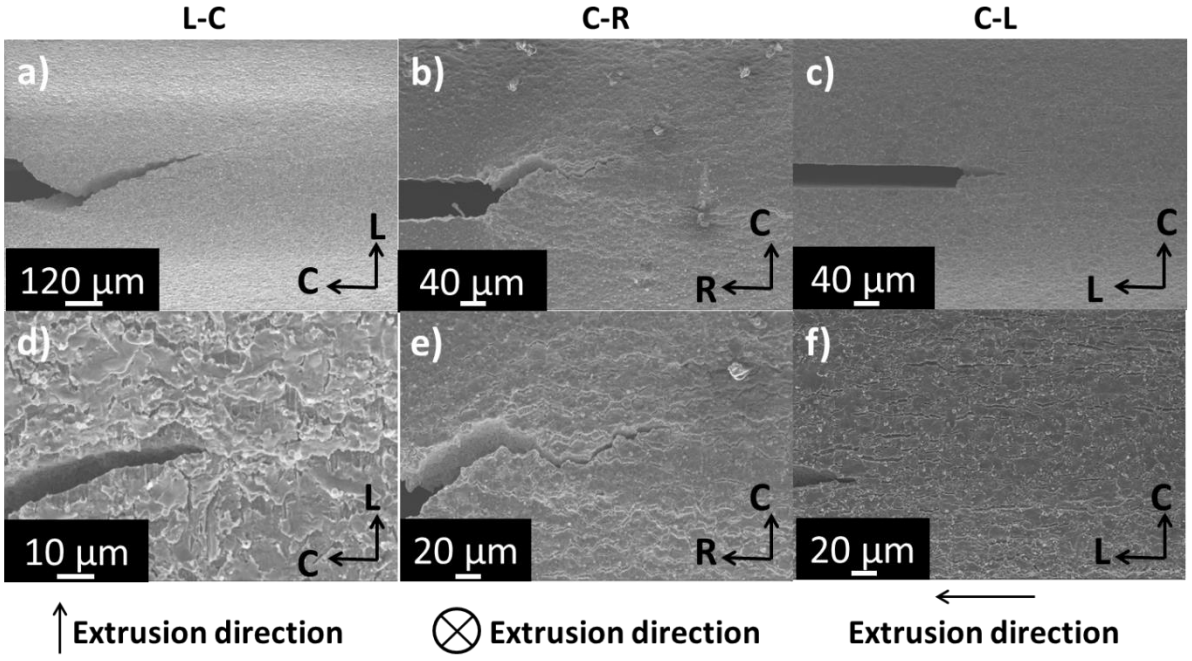

Fig. 69 Side view of the propagated crack after fracture toughness testing in different orientations of ODS-CSM at RT.

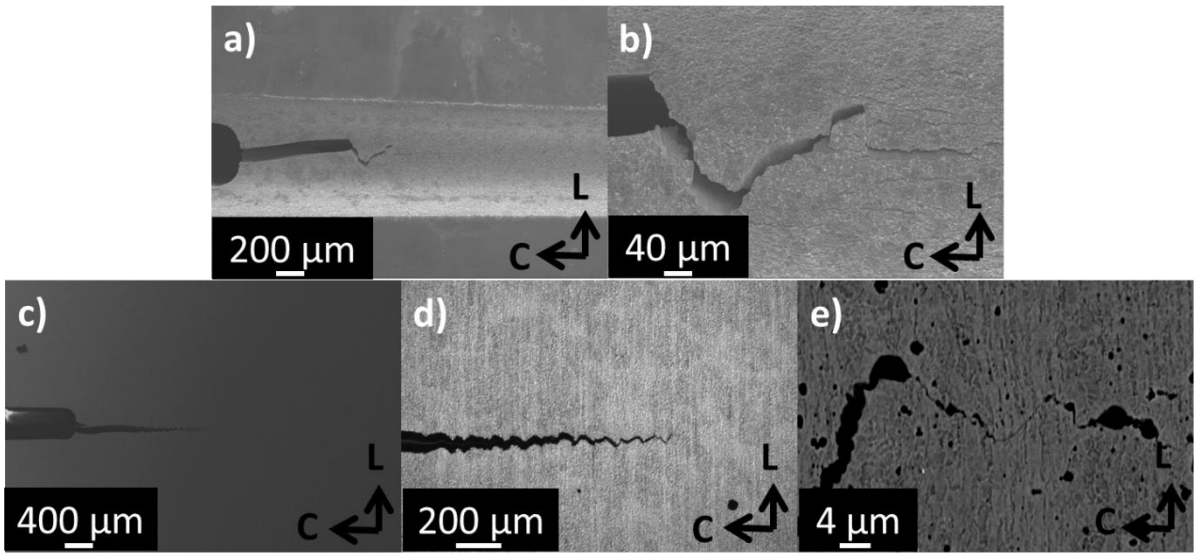

Fig. 70 Side view of the propagated crack close to the specimen surface after fracture toughness testing (a and b) and close to the crack front middle after sectioning and etching (c-d) in the L-C orientation of ODS-CSM at 400 ˚C.

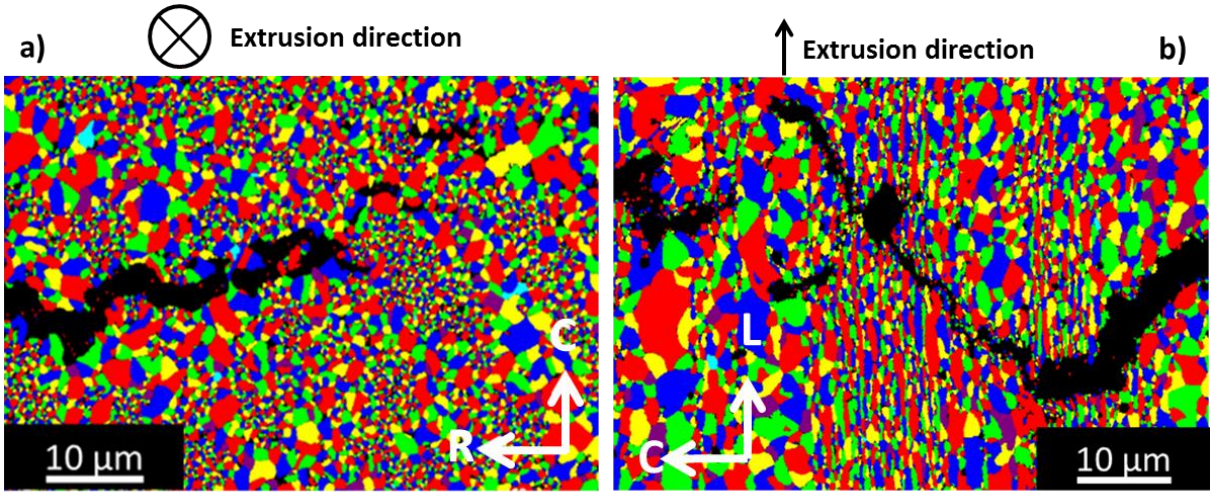

Fig. 71 EBSD grain distribution map of the a) C-R and b) L-C oriented specimen of ODS-CSM showing the side view of the primary crack growth with respect to the grains.

4.5.4 Summary

The primary crack seems to propagate through the UFG regions. Crack growth is always greater in orientations in which the primary crack propagates parallel to the rolling/extrusion direction. The coarse and fine-grained zones in such cases are elongated in the crack propagation direction. In cases where the crack propagation direction is perpendicular to the elongated coarse and fine-grained zones, the crack growth is lesser.

Secondary cracks initiate at lower loads as compared with the primary cracks and also exhibit orientation dependence. They were mainly observed in hot-rolled material. The secondary cracks follow similar fracture mechanisms as primary cracks and depend on the test temperature.

We now have information about all the ODS steels with respect to their microstructure and fracture behaviour. In the discussion section, the information from the results section will be exploited to highlight the main questions of this research, which were already mentioned in the introduction section:

- What are the microstructural factors which affect fracture toughness and why some ODS steels exhibit higher fracture toughness than the others?
- On what microstructural factors is the observed fracture anisotropy dependent?
- On what microstructural factors is secondary cracking dependent and why does it vary for hot-rolled and hot-extruded materials?

5 Discussion

All the three ODS steels exhibit ductile fracture from RT to 400 ˚C except ODS-KIT HE at RT in the C-R (Fig. 49b) and C-L orientations (Fig. 49c). This brittle behaviour is probably due to its higher ductile to brittle transition temperature (DBTT) which arises from its low Ni content and higher average coarse grain size [110]. Impact testing to determine the DBTT could not be performed since large amounts of material were unavailable. Small punch tests (SPT) were used alternatively to investigate the DBTT and the results confirmed that ODS-KIT HE had a higher DBTT than the other materials. A comparative study will be published in the future [111]. It is noteworthy however, that SPT only gives an indication about the comparative DBTT of the materials and cannot be directly compared with the traditional Charpy V notch DBTT values.

The fracture toughness of the ODS steels is lower than P91 steel in the temperature range of RT to 400 ˚C, except ODS-KIT HE (Fig. 41a). This exception is also evident from the lesser crack growth of both ODS-KIT HE and P91 steel for the same load line displacement (Fig. 41c).The fracture toughness of all the ODS steels drops drastically at high temperatures (T > 400 ˚C) due to intergranular fracture as observed from the fracture surfaces at 600 ˚C (Fig. 46, Fig. 50 and Fig. 56). This drop in fracture toughness is corroborated by the crack growth versus load line displacement plots at 600 °C which shows a high crack growth for all the ODS steels (Fig. 41e). The reasons for this loss of fracture toughness can be linked to the weakening of grain boundaries due to segregation of O, N and C at the grain boundaries [69], dislocation pileup at the grain boundaries [68,98,112], Ti and O rich stringers at the prior particle boundaries [113] and shallow plastically deformed zone formation [66]. From the fracture surfaces at 600 ˚C (Fig. 52c and Fig. 58d), it is clear that the fracture surface undulation reduces as compared with lower temperatures as the plastic zone becomes shallower. The loss of undulation in the fracture surface from 400 ˚C to 600 ˚C is the highest in ODS-KIT HE resulting in the highest loss in fracture toughness at 600 ˚C (Fig. 41a). More information about high temperature deformation mechanisms were reported elsewhere [52,68,96]. Cr segregations at the grain boundaries of ODS-CSM however, possibly acts as barriers to grain boundary movement thus making grain boundary sliding difficult at high temperatures. The degradation of fracture toughness from 400 ˚C to 600 ˚C is therefore lower for ODS-CSM than ODS-KIT HE and ODS-KIT HR. Similar effect was observed in reference [54]. The non-ODS reference FM steel P91 exhibits much higher fracture toughness at higher temperatures than ODS steels. Similar results were also reported in reference [7]. This is also evident from Fig. 41e which shows lesser crack growth for P91 steels at 600 ˚C in comparison with ODS steels for the same load line displacement.

Although fracture behaviour at higher temperature is very important from the point of view of application, it is not the primary focus of this research. The three main questions pertaining to this research, as mentioned earlier, are relevant for a lower temperature range and will now be discussed in the subsequent sub-sections.

5.1 Factors affecting fracture toughness

In the temperature range of RT to 400 ˚C, ductile fracture prevails in most ODS steels and orientations apart from a few exceptions as mentioned earlier. In ductile fracture, according to the stress-modified critical strain criteria, fracture in an isotropic material takes place when the local equivalent plastic strain exceeds a critical fracture strain $\bar{\epsilon}_f^*$ over a characteristic distance l_0^* [114–116]. The fracture toughness in terms of mode I J-integral value (J_{IC}) is proportional to the yield stress, the critical fracture strain and the inter-particle spacing (Eq. 18). In Eq. 18, the product of critical fracture strain and characteristic length represents the local ductility of the material. In another work, Ashby suggested that the decohesion strain between a void initiating particle and its matrix is dependent on the work of adhesion between them and other factors as presented in Eq. 19 [116–118]. In this context, it is assumed that the void initiating particles are of equal size, are equally spaced and pre-existing dislocation density and tangling are neglected.

For the initiation of ductile fracture, one can assume that the critical fracture strain ($\bar{\epsilon}_f^*$) is equal to the decohesion strain (ϵ) between the void initiating particle and the matrix. Therefore, J_{IC} can be written in terms of microstructural parameters (W, l and d), yield stress, shear modulus and Burgers vector (Eq. 20). All the parameters were determined using mechanical testing and microstructural investigations except W, which is obtained indirectly.

$$J_{IC} \sim \sigma_0 * \bar{\epsilon}_f^* * l \tag{18}$$

$$\epsilon = \frac{2 * W * l}{G * b^* * d} \tag{19}$$

$$J_{IC} \sim \sigma_0 * \frac{2 * W * l^2}{G * b^* * d} \tag{20}$$

where,

σ_0 = Yield stress

$\bar{\epsilon}_f^*$ = Critical fracture strain

ϵ = Decohesion strain between particle and matrix

l = Mean void initiating particle spacing

W = Work of adhesion or particle-matrix bond strength

G = Shear modulus

d = Size of the void initiating particle

b^* = Burgers vector

5.2 Anisotropic fracture behaviour

The fracture toughness of the L-T oriented samples is higher than that of the T-L oriented samples (Fig. 38a and b) in ODS-KIT HR which is in accordance with previous works on hot-rolled materials [29,74,77]. The hot-extruded specimens from ODS-KIT and ODS-CSM also exhibits fracture toughness anisotropy with the L-C orientation possessing the highest fracture toughness followed by the C-R and C-L orientations (Fig. 39a, b and Fig. 40a, b). This is also in accordance with previous works [29,39,77,78]. There are three fundamental factors which contribute towards fracture anisotropy. How these three factors influence the fracture toughness anisotropy will be discussed in the next subsections. These factors are:

1. Anisotropic crystallographic orientation
2. Anisotropic particle distribution
3. Anisotropic grain morphology

5.2.1 Anisotropic crystallographic orientation

A <110> texture parallel to the rolling or extrusion direction (L) is found in all the materials (Fig. 19, Fig. 25 and Fig. 33), both for the fine and the coarse grains (Fig. 20, Fig. 26 and Fig. 34). This affects the shear modulus of a material in different orientations. Walpole et al. proved that minimum shear modulus in a cubic crystal is achieved in the (110) plane [119]. It must be noted that the variation between the minimum and maximum shear modulus varies for different materials with different anisotropic factors. For iron, this variation is significant. The minimum shear modulus is calculated to be 48 GPa using compliance constants of BCC iron [120]. Due to the <110> texture in the extrusion direction, this shear modulus value corresponds to the L-C oriented specimen (primary crack plane parallel to (110) plane). The other directions perpendicular to the longitudinal direction contained a mixture of all crystal orientations with no dominant texture and hence can be considered isotropic. The isotropic shear modulus was calculated to be 73 GPa using the compliance constants of BCC iron [121]. This shear modulus value corresponds to the C-L and the C-R oriented specimens. The ratio of minimum shear modulus in the longitudinal direction (L) to isotropic shear modulus in the orthogonal directions is therefore calculated to be 0.66.

It was also reported in another work that the <110> direction (which is parallel to the extrusion/rolling direction) exhibits higher void nucleation and growth in ductile fracture as compared to the other directions [122]. This is due to because of the high Taylor factor for the <110> direction as compared to other directions, making it the hardest direction.

5.2.2 Anisotropic particle distribution

Nano- and sub-micron particles

Particles can be classified as nano-particles or as sub-micron particles depending on their size as described in previous sections. The former are responsible for the strength or flow stress of the material. The size and the inter-spacing of the nano-particles determine how effectively they can obstruct dislocations. The distribution of the nano-particles is not perfectly homogenous in all the materials as can be seen from Fig. 21 for ODS-KIT HR, Fig. 27 for ODS-KIT HE and Fig. 35b for ODS-CSM. Yet, the yield stress of the material was reported to be similar in the longitudinal and transverse direction in previous works [39,71]. This is possibly because dislocation obstruction in the bulk material considered as a macroscopic phenomenon does not get affected by the local inhomogeneities of the nano-particle distribution.

Ductile fracture takes place through void growth and coalescence on the void initiating particles and pre-existing pores. Chaouadi et al. [70] reported that the stress-strain incompatibility between the hard nano-particles and the soft iron matrix promoted void nucleation, growth and coalescence. However, it was reported in other studies that void initiation, growth and coalescence is preferred on the sub-micron particles rather than on the nano-particles [14,95,116,123]. In the present work, particles of the size similar to the sub-micron particles are observed inside the dimples on fracture surfaces as marked by arrows in Fig. 56e. This confirms that ductile fracture arises through the sub-micron particles. Also, due to the resolution limit of the SEM, no evidence was discovered for the role of the nano-particles in dimple formation. Similar conclusions were made in reference [22]. Byun et al. [22,66] found that the fracture processes occurring on the nano-scale have limited influence on the fracture toughness and that the meso- and the macroscopic failure mechanisms are the main reasons for the failure. Taking all these observations into account, the sub-micron particles are given the main focus in the present work for the ductile fracture mechanisms which take place between RT and 400 ˚C. For the sub-micron particles, using Eq. 20, one could say that the larger the inter-particle spacing (l) and the smaller the particle size (d) is, the higher the fracture toughness is. These two parameters can vary from one material to the other and also within different regions of a single material due to inhomogeneity and anisotropy.

Fracture surface morphology

The fracture surfaces exhibit dimples in the ductile regime for all the materials. The width and the height of a dimple seen on the fracture surface, depends on the size and the number density of the void initiating particles. When the particles are densely packed, the dimples are finer as a growing dimple meets its neighbour at short distances and its growth is stopped. When the particles are located far away from each other, the dimples can grow and reach larger dimensions before their growth is stopped by its neighbouring dimple. The pronounced existence of large and medium sized dimple regions in ODS-KIT HR (Fig. 45) and in ODS-KIT HE (Fig. 51) in the ductile regime suggest a high

number of low number density sub-micron particle (LD) regions. The flat regions are not formed due to debonding of oxide coated prior particle boundaries as suggested earlier in some studies [42] but are formed due large inter-particle spacing and low ductility. To support this claim, it can be seen from Fig. 52d and e, that the flat region on the fracture surface at 200 ˚C changes into deep dimples at 400 ˚C due to the higher degree of plasticization. This clearly indicates the fracture mechanism to be a typical trans-granular ductile fracture mechanism. The high number of LD regions in ODS-KIT HE is also corroborated by the TEM image in Fig. 28b where thin bands of high number density Ti-enriched sub-micron particles and thick zones of low number density sub-micron particles are observed.

As the large dimples in ODS-CSM are not as big as the large dimples in ODS-KIT (Fig. 57), it suggests denser sub-micron particle distribution in ODS-CSM, even in the LD regions. As compared with ODS-KIT HE, thinner sub-micron particle LD regions are present in ODS-CSM. TEM images indicate the presence of Si and O-enriched sub-micron particles in the HD zones which are parallel to the extrusion direction (Fig. 32). These sub-micron particles are formed in ODS-CSM possibly due to the high Si content in the matrix and due to the contaminations picked up during the manufacturing process. It is fair to assume that improper milling led to inhomogeneous sub-micron particle distribution.

Interaction of crack front with sub-micron particles

To understand the effect of the sub-micron particle distribution anisotropy on the fracture toughness, the intersections of the sub-micron particles arranged in the direction of rolling/extrusion can be visualized with the crack propagation planes in all the orientations (Fig. 72). For simplicity, only ODS-KIT HE is analysed for particle anisotropy. A similar analysis can be performed for the other ODS steels. The crack front propagates through the low number density (LD) and the high number density (HD) particle regions simultaneously or sequentially as shown in Fig. 72 for different orientations. Therefore, the parameters l and d vary for different crack planes and an effective l and d needs to be calculated.

Using Eq. 20 for the ductile fracture of ODS-KIT HE at 200 ˚C, one can find the ratios of the fracture toughness in the different orientations (C-R/C-L and L-C/C-L) and correlate it with ratios of the microstructural features (l and d), shear modulus and yield stress (Eq. 21):

$$\frac{J_{IC}^{CR}}{J_{IC}^{CL}} = \frac{\sigma_0^{CR}}{\sigma_0^{CL}} * \frac{G_{CL}}{G_{CR}} * \frac{l_{CR}^2}{l_{CL}^2} * \frac{d_{CL}}{d_{CR}} \text{ and } \frac{J_{IC}^{LC}}{J_{IC}^{CL}} = \frac{\sigma_0^{LC}}{\sigma_0^{CL}} * \frac{G_{CL}}{G_{LC}} * \frac{l_{LC}^2}{l_{CL}^2} * \frac{d_{CL}}{d_{LC}} \quad (21)$$

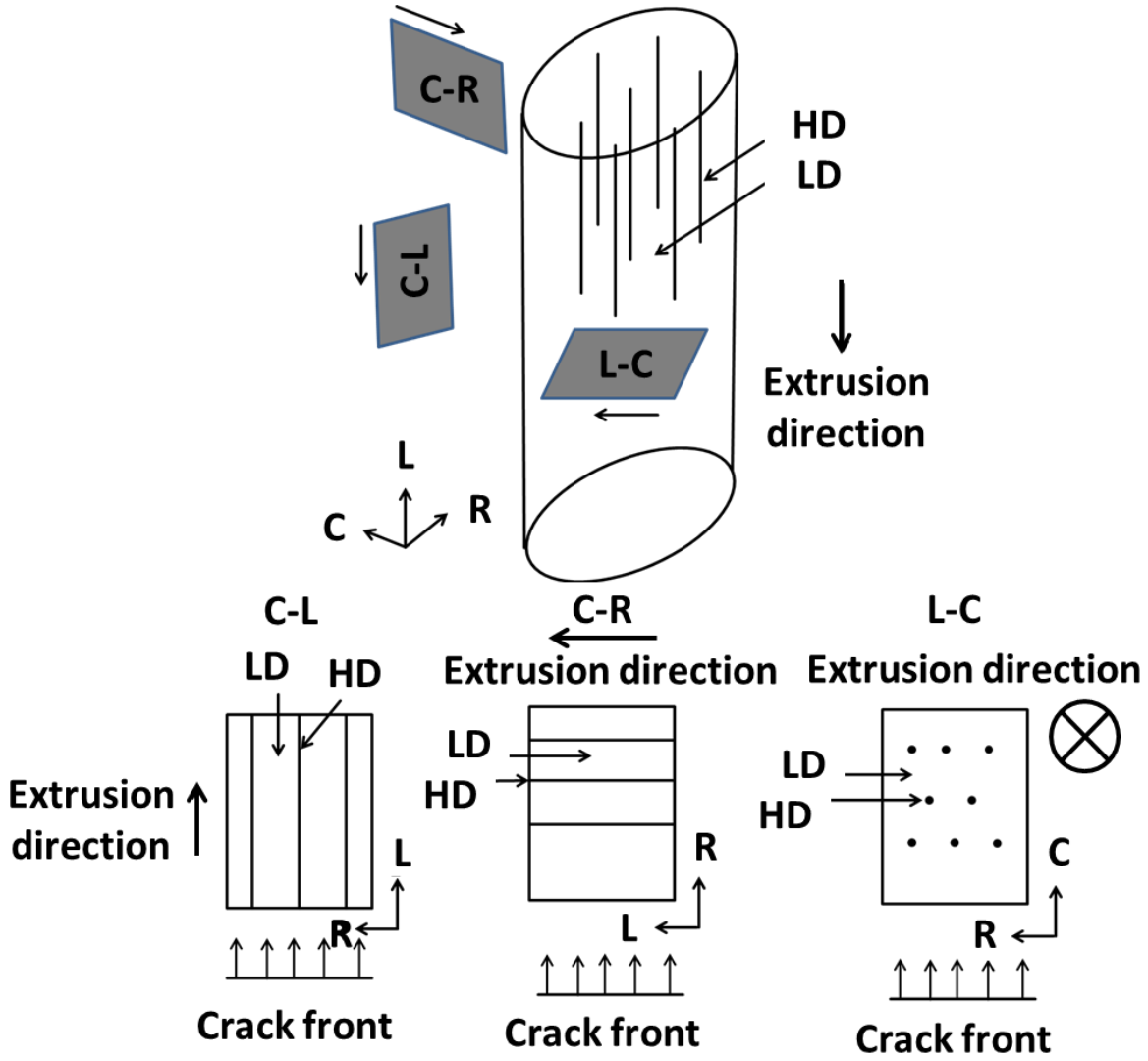

Fig. 72 Schematic showing propagating primary crack planes in different orientations and their relation with the high number density sub-micron particle regions (HD) and the low number density sub-micron particle regions (LD) aligned parallel to the extrusion direction.

C-L orientation

It is seen that the crack propagates through the HD and LD regions simultaneously. The sub-micron particles are arranged parallel to the extrusion direction which is also the direction of crack propagation (Fig. 72). The resistance to crack propagation is higher in the LD region than in the HD region. Effective values of the inter-particle spacing and the particle size for the propagating crack plane are calculated using a parallel combination of LD and HD particle regions weighted with their area fractions (p_{HD} and p_{LD}) (Eq. 22 and 23). This is analogous to a mechanical system with parallel springs. The effective values are presented in Table 9.

$$l_{CL} = l_{eff} = p_{HD} * l_{HD} + p_{LD} * l_{LD} \tag{22}$$

$$d_{CL} = d_{eff} = p_{HD} * d_{HD} + p_{LD} * d_{LD} \tag{23}$$

where,

l_{eff} = Effective inter-particle spacing in the C-L orientation

d_{eff} = Effective particle size in the C-L orientation

l_{HD} = Inter-particle spacing in the high number density region

l_{LD} = Inter-particle spacing in the low number density region

d_{HD} = Particle size in the high number density region

d_{LD} = Particle size in the low number density region

p_{HD} = Fraction of high number density particle region encountered by the crack front

p_{LD} = Fraction of low number density particle region encountered by the crack front

Table 9 Microstructural parameters of inter-particle spacing and particle size in the C-L orientation.

Material	p_{HD}	p_{LD}	${l_{LD}}^2$	d_{LD}	${l_{HD}}^2$	d_{HD}	l_{eff}^2	d_{eff}
ODS-KIT HE	0.05	0.95	0.76	0.06	0.048	0.06	0.701	0.06
ODS-CSM	0.42	0.58	2.72	0.09	8.58	0.47	4.78	0.25

C-R orientation

In the C-R orientation, the crack plane propagates through the HD and the LD regions sequentially as the direction of crack propagation is perpendicular to extrusion direction (Fig. 72). The J_{IC} value depends on the regions through which the crack propagates until a crack extension of 0.2 mm is reached. In case of ODS-KIT HE, as the HD regions are very thin, it is reasonable to assume that the crack travels predominantly through the LD regions. Consequently, the inter-particle spacing and the size of the particle can be associated with the LD region as presented in Table 10.

L-C orientation

The crack has to cut through both the HD and the LD regions towards a direction perpendicular to the extrusion direction (Fig. 72). The HD and LD regions are parallel to the extrusion direction and perpendicular to the crack propagation direction. A similar simplification assuming crack propagation occurring predominantly through the LD regions can also be made for the L-C orientation as it was done for the C-R orientation (Table 10).

Table 10 Microstructural parameters of inter-particle spacing and particle size in the LD regions for the C-R and L-C orientations.

Material	$l_{LD}{}^2$	d_{LD}
ODS-KIT HE	0.76	0.06

Table 11 Ratios of contributing factors to ODS-KIT HE fracture toughness in the C-R and L-C orientations with respect to the C-L orientation at 200 ˚C (Eq. 21).

Orientation Ratio	J_{IC} *Ratio*	σ_0 *Ratio*	G Ratio	l^2 *Ratio*	*d Ratio*
CR/CL	1.36	≈1	1	1.08	1
LC/CL	4.54	≈1	≈1.5	1.08	1

Analysis

The ratios of contributing factors for the fracture toughness are obtained using Eq. 21 and are presented in Table 11. It is noticed that the yield stress ratio of the material remains similar from RT to 400 ˚C in different orientations [39,71] and did not dominantly contribute to the fracture anisotropy. Crystallographic texture of <110> parallel to the extrusion direction results in different shear moduli in different planes (section 5.2.1). This means that the shear modulus of the material in the L-C orientation (towards extrusion direction) is the lowest and its ratio with the shear modulus in the C-L orientation is close to 1.5. This contributes to the increase in fracture toughness ratio. However, the increase is not big enough to compensate for the actual increase in the fracture toughness observed during the experiment ($\frac{J_{IC}^{LC}}{J_{IC}^{CL}} = 4.54$). The C-R and C-L orientations are considered to be equally isotropic and hence their shear moduli are assumed to be equal. It is observed from Table 11 that the inter-particle spacing and particle size ratios do not significantly contribute to the increase in fracture toughness ratios of the C-R and L-C orientations with the C-L orientation (Table 11). This is due to the fact that Eq. 20 was derived for isotropic materials where the particles are of equal size, have equal spacing and have isotropic grains. There is therefore, another factor, missing from Eq. 20, which contributes to the increase in the fracture toughness. This is discussed in the next sub-section.

5.2.3 Anisotropic grain morphology

The microstructure in all the materials is bimodal and elongated towards the rolling/extrusion direction (Fig. 18, Fig. 23 and Fig. 31). Many of the fine grains, especially less than 1 µm, can be classified as ultra-fine grains (UFGs) [124]. The mechanical properties of the UFGs are different from that of the coarse grains with respect to strength and deformation capability. Coarse grains have lesser strength and are able to deform much more than fine grains as the dislocations can interact with each other within the grains forming dislocation cells. The UFGs have a lower deformation capability as dislocations assemble and rearrange themselves at the grain boundary reaching saturation [85,124–126]. This is associated with hardening leading to a higher yield stress with evolving plastic strain. The crack

propagation in the C(T) specimens preferentially follows the ultra-fine grained region as seen through the examples of ODS-KIT HR (Fig. 62) and ODS-KIT HE (Fig. 68a). During loading of the C(T) specimen, the coarse grains reach their yield point first and deform plastically. The fine grains reach their yield point next, but cannot plastically deform significantly, thus initiating voids which subsequently assist the primary crack to propagate. Similar fracture behaviour for a non-ODS bimodal alloy was reported in reference [125].

Hot-rolled material

For the case of ODS-KIT HR, the primary crack propagation in the T-L specimen is along the rolling direction (L direction). The crack propagation has a relatively free path (Fig. 62b) through the ultra-fine grains (arranged in the L direction) and does not face obstruction from the coarse grains which are elongated parallel to the rolling direction and has a GAR value of 10 in the LS plane. The primary crack propagation in the L-T specimen is along the transverse direction (T direction) which is less assisted by fine grains (arranged more in the L than in the T direction) and is less obstructed by the coarse grains which have a GAR value of 4 in the TS plane (less elongated in the TS than in the LS plane). The primary crack in the L-T specimen is blunted by the coarse grains (Fig. 62a). Similar mechanism was also seen in reference [125]. Crack branching in the fine grains is observed to be in a direction parallel to the rolling direction in both the L-T (Fig. 62c and d) and the T-L orientations (Fig. 62e and f). The dissipation of energy by crack branching is more in the L-T than in the T-L orientation as the crack has to deviate more from its original path (along the primary crack). This energy dissipation by branching retards the primary crack propagation. The energy required to propagate the primary crack in the L-T oriented specimen is therefore more than in the T-L oriented specimen resulting in its higher fracture toughness.

Hot-extruded material

In case of hot-extruded materials, the crack propagates through the ultra-fine grains (UFGs) which are arranged in zones elongated in the extrusion direction (Fig. 73a). For ODS-KIT HE in the C-L orientation, there is a possibility of crack deviation towards other adjacently lying ultra-fine grained zones. A schematic of how the grain morphology affects the crack propagation in the extrusion direction is presented in Fig. 73a. EBSD grain distribution maps of ODS-KIT HE containing the propagated crack in the C-L orientation is also shown. Minimal crack deviation (like shown in schematic) is observed due to arrangement of the UFGs in the same direction as the crack propagation. Energy dissipation due to obstruction by coarse grains is small as they are elongated in the direction of crack propagation. In the C-R orientation, the possibility of crack deviation along the UFGs is more as shown in an example involving ODS-CSM (Fig. 73b). The C-R fracture surfaces exhibit wavy macro surface morphology (Fig. 55b and e) confirming crack deviation. However, the energy dissipation is still small as the crack can find a path of least resistance to propagate. In the L-C orientation, during propagation, the crack is blunted while passing through the perpendicularly elongated coarse grains and cannot access any low

resistance path by crack deviation as seen from an example involving ODS-KIT HE (Fig. 73c). The energy dissipation through crack propagation in the L-C orientation is the highest.

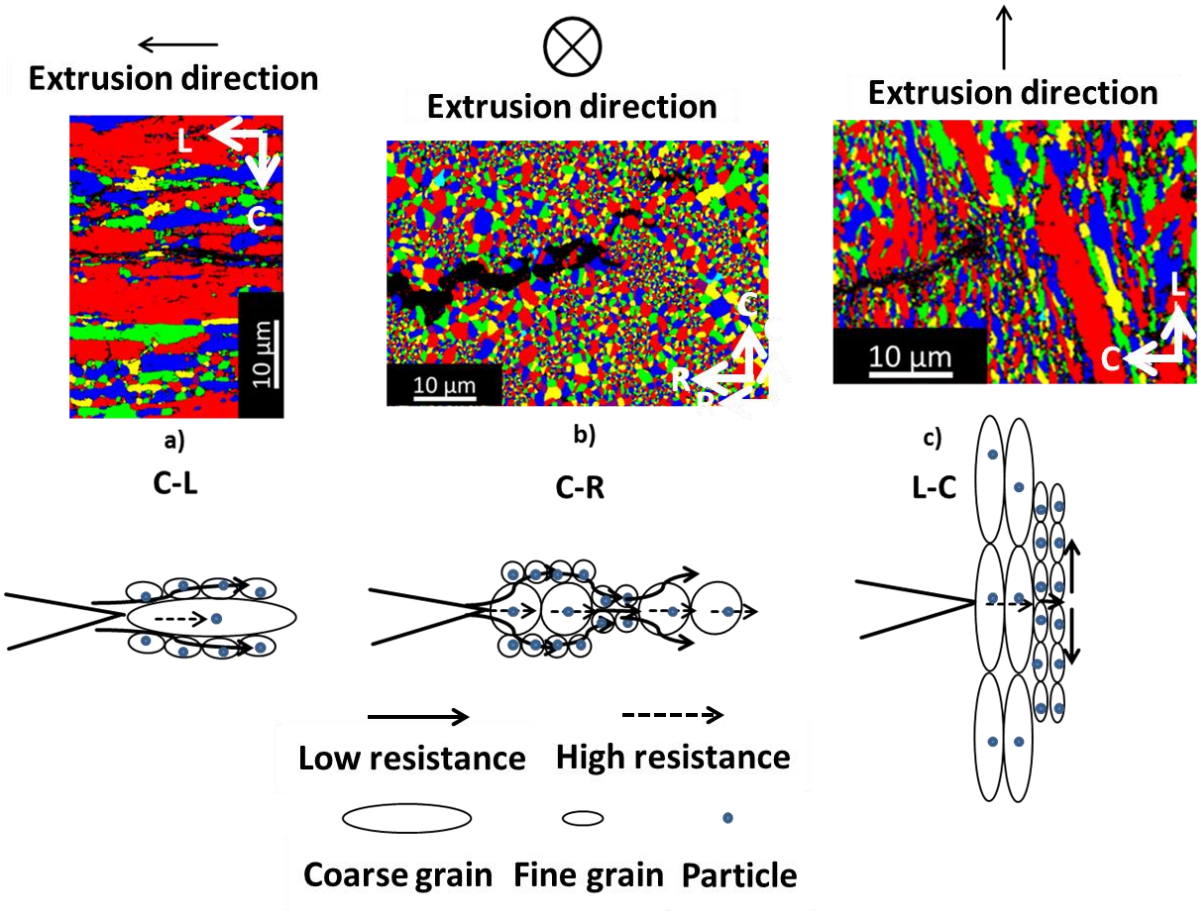

Fig. 73 Schematic showing the side view of the crack propagation in all the three orientations of hot-extruded specimens along with the EBSD grain distribution maps of the side surfaces of tested specimens supporting them.

5.2.4 Dominant contributor to anisotropic fracture toughness

From the above discussion it can be said that the contributions from anisotropy in particle distribution (particle size and inter-spacing) and anisotropy in crystallographic orientations are lesser than the contribution from the anisotropic grain morphology.

Grain morphology anisotropy leads to crack tip blunting, which plays a major role in increasing the fracture toughness of certain orientations. This is the missing factor from Eq. 20 and Eq. 21. The L-C and L-T orientations in hot-extruded and hot-rolled materials, respectively assist greater crack blunting through perpendicularly elongated coarse grains. Even though the load maximum of the L-T and L-C orientations are only slightly higher than the other orientations, the ductility or area under the load displacement curve is much higher (Fig. 38c, Fig. 39c and Fig. 40c). This is due to the crack blunting effect in these orientations. Crack propagation is the least in the L-T and L-C oriented specimen for the same load line displacement due to crack tip blunting (Fig. 38d, Fig. 39d and Fig. 40d). Due to

these reasons, the L-T and L-C orientations possess higher fracture toughness than other orientations. The contribution from crack blunting is minimal in the C-R, C-L and T-L orientations as the crack can deviate and follow the path of least resistance (through overlapping regions of adjacently lying high number density particles and ultra-fine grained zones) and thus possess lower fracture toughness.

5.3 Secondary cracking

Secondary cracks propagate in a plane perpendicular to the primary crack plane (Fig. 74) and are formed due to constraint induced stresses. Pronounced secondary cracking is observed in ODS-KIT HR while partial or no secondary cracking is observed in ODS-KIT HE and ODS-CSM. It is evident from the fracture surfaces of ODS-KIT HR that the secondary cracks exhibit lesser propensity and get arrested with increasing temperature due to crack tip blunting and plastification (Fig. 42). Their contribution to the energy absorption is therefore lesser at higher temperatures. Unlike the primary crack, no fatigue pre-crack is available for the initiation of secondary cracks. Therefore, the initiation of secondary cracks must transpire through the pre-existing microcracks or through decohesion of the sub-micron particles with the matrix, which are lying on the primary crack plane.

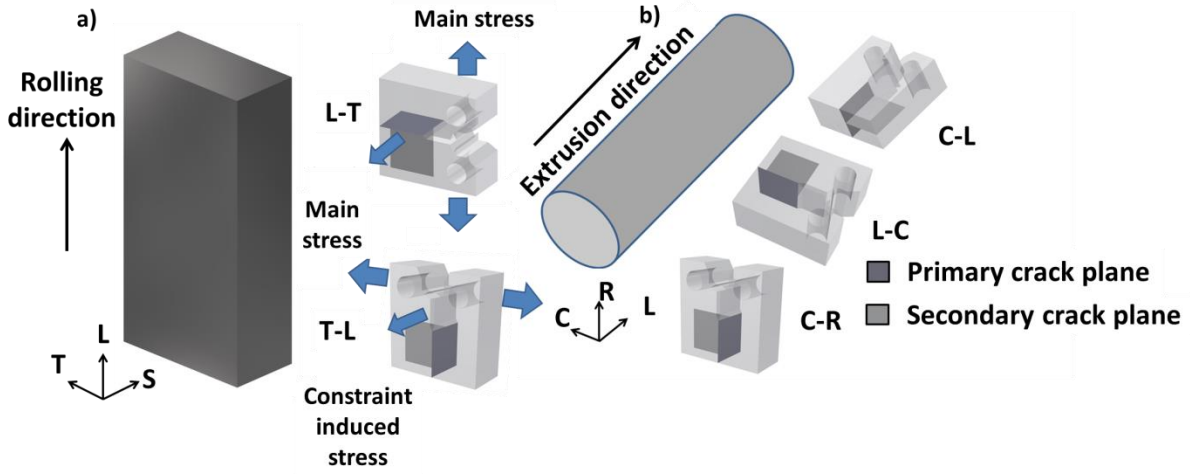

Fig. 74 A schematic illustration of main stress and constraint induced stress in C(T) specimens in a) two orientations of hot-rolled specimen and b) three orientations of hot-extruded specimen indicating primary and secondary crack planes.

5.3.1 General factors affecting secondary cracking

Secondary cracks form in a similar fashion as primary cracks, by cleavage at low temperatures and by void growth and coalescence in the ductile regime. Ashby [117] had suggested that void nucleation due to particle-matrix decohesion takes place when a critical stress is reached at the particle-matrix interface. For ductile fracture, when the constraint induced stress (σ_C) exceeds the critical fracture stress for void nucleation (σ_f) in a particular plane, secondary cracks appear (Eq. 24). σ_f can also be referred to as the critical stress for particle cracking in case of cleavage fracture at low temperatures.

$$\sigma_C > \sigma_f \tag{24}$$

Both these competing stresses can be affected by the microstructural anisotropy in the material. The main microstructural anisotropic factors which can affect secondary cracking are the same factors which affect the primary crack propagation (discussed in section 5.2). The following sub-sections discuss if the same anisotropic factors are important for the present set of materials and if yes, to what extent. It is also discussed how secondary cracking differ in hot-rolled and hot-extruded materials.

5.3.2 Understanding of secondary cracking in hot-rolled ODS steels

It is worth mentioning that in this work, due to material and geometrical limitations, only hot-rolled specimens with "crack-divider" geometries (L-T and T-L) were investigated which typically have lower fracture toughness than hot-rolled specimens with "crack-arrestor" geometries (e.g. L-S and T-S) [84]. Since, the focus was on secondary cracks, which can be clearly understood using the crack-divider geometry in hot-rolled specimens, there was no need to investigate crack arrestor geometries which induces no secondary cracking. For hot-extruded specimens, the terms crack divider and crack arrestor are typically not used.

Effect of crystallographic texture

For ODS-KIT HR, secondary cracks propagate through the LT plane in both the L-T and T-L oriented specimens (Fig. 74). In terms of crystallographic orientation, ODS-KIT HR possesses a strong texture component of {100} <110> (Fig. 19). It was reported that for BCC polycrystalline materials with such texture, when the material uniaxially deforms in the directions L or T, the material does not act axisymmetrically but tends to deform by plane strain under uniaxial tensile stresses along the <110 > direction [74]. As a result of this, tensile stresses in {100} planes (parallel to the rolling plane LT) and compressive stresses in {110} planes (parallel to the rolling direction) are generated [127,128] which have an absolute value of the order of 1/5 and 1/3 of the material flow stress, respectively [129,130]. In a BCC crystal, the most preferable cleavage planes are the {100} planes. Therefore at low temperatures, the tensile stresses cleave the {100} planes, aligned parallel to rolling plane (Fig. 19). As the secondary crack planes (LT planes in Fig. 74a and b) are parallel to the cleavage planes, secondary cracks appear. Similar results were also reported in reference [46].

At higher temperature (ductile regime), it was reported that void growth and coalescence is preferred in the <110> direction [122] which helps secondary crack formation towards the rolling direction (L). The arrangement of Ti-enriched sub-micron particles along the rolling (Fig. 22c) and transverse direction (Fig. 22d) also helps in void growth and coalescence and assists secondary cracking. Pre-existing pores and microcracks elongated in the direction of rolling (Fig. 22a) additionally contributes to secondary cracking, as also reported in reference [67].

Effect of grain morphology

As discussed previously, the anisotropic grain morphology predominantly affects the primary crack propagation (section 5.2.4). The effect is the same for secondary crack propagation. The coarse grains are elongated in the L and T directions (the secondary crack directions), the former more than the latter, leading to less crack blunting and easier crack propagation in these directions. The secondary cracks propagate through the ultra-fine grains similar to primary cracks as was reported in reference [47]. For the secondary crack propagation in the L-T specimen, the crack must propagate in the L (depth) and in the T (in-plane) directions (Fig. 74a). For the T-L oriented specimens, the fracture plane remains the same (LT). The crack now propagates in the T direction (depth) and L direction (in-plane). As crack propagation in these directions is less obstructed (due to less crack blunting), the critical fracture stress σ_f is low for the LT plane. The constraint induced stress σ_C is high enough to overcome the critical fracture stress in both the orientations (Eq. 24). Thus, ODS-KIT HR in the L-T and T-L orientations are majorly affected by secondary cracking. The extent of secondary cracking should have been the same for both the orientations but this is not the case. T-L oriented specimens experience less secondary cracking as compared with the L-T oriented specimens (Fig. 64). The reason is the different constraint induced stresses experienced by specimens in both these orientations. The constraint induced stresses are lower in the T-L orientation than in the L-T orientation. This is due to lower main stresses in the T-L orientation (Fig. 38c) which stem from easier primary crack propagation (as discussed previously). This also explains the early disappearance of the secondary cracks with increasing temperature in the T-L oriented specimens as compared with the L-T oriented specimens (Fig. 42).

Secondary crack initiation

Secondary cracks initiate earlier than the primary cracks at lower loads. In the case of an interrupted fracture mechanics test, they appeared early in the elastic regime during testing, even before primary crack growth (at a low J value of 14 kJ/m^2) as seen from Fig. 63. This early initiation is due to the ease of crack propagation in the secondary crack plane (LT) than in the primary crack plane (TS plane for the L-T oriented specimen and LS plane for the T-L oriented specimen) (Fig. 74). The LT plane (secondary crack plane) contains both the elongated grain directions L and T as compared to only one elongated grain direction L or T in the LS or TS plane (primary crack planes), respectively.

Fracture mechanisms

To explore the fracture mechanisms associated with secondary cracking, EBSD misorientation line scans were performed across a secondary crack lying on a plane perpendicular to the secondary crack plane. Results indicate that the secondary crack was sometimes transgranular (low misorientation angle < 5°) (line scans 1 and 2 in Fig. 65) and sometimes intergranular (high misorientation angle > 15°) (line scans 3 in Fig. 65) at RT while always intergranular at 600˚C (Fig. 66). The low-angle misorientations hint towards the presence of either or both transgranular cleavage and transgranular ductile fracture mechanisms. The presence of both cleavage and ductile fracture is confirmed by SEM images

of the secondary crack surface at RT (Fig. 47b and c). Regions of flat cleavage facets mixed with regions of shallow dimples indicate local variations in the stress states during the crack propagation. Similar observations are also observed for the primary cracks (Fig. 43) at -100 ˚C. The fact that the side view of the secondary crack has predominantly sharp edges (Fig. 65), suggests the preference of cleavage over ductile fracture at low temperatures. Regions of high misorientation angles at RT indicate intergranular fracture and possibly originate due to grain boundary segregations as was reported in other works as well [39,75,78,80]. The ratio of shear to bulk modulus also plays a role in the preference of intergranular over cleavage fracture [95]. Due to the elongated coarse grains, intergranular fracture with typical sharp facets was not observed on the fracture surfaces. Existence of dimples (Fig. 47f) on the fracture surface at a test temperature of 200˚C indicates that the material is already in its ductile regime. The high-angle misorientations at the test temperature of 600˚C (Fig. 66) are observed due to intergranular fracture caused possibly by grain boundary sliding or grain matrix deformation phenomena as reported in a previous work [52]. The side view of the crack does not exhibit sharp edges at 600˚C (Fig. 66) and exhibits nano-features on the secondary crack surface (Fig. 47i), similar to what was observed on primary fracture surfaces (Fig. 46f), confirming a change of fracture mechanism from transgranular to intergranular fracture.

Effect on primary cracks

The existence of secondary cracks not only increases the amount of energy absorbed during fracture, but also helps prevent unstable primary crack initiation. In ODS-KIT HR, the ease of primary crack propagation in the T-L oriented specimen (section 5.2.3) made its propagation unstable in these specimens. However, from -100 °C up to 100 °C, the T-L oriented specimens exhibited stable primary crack propagation due to the existence of secondary cracks which increases energy absorption (Fig. 42). Similar energy absorption was reported in the crack divider geometry at low temperatures due to secondary cracking in reference [46]. The secondary cracks absorb energy and lower the local driving force for growth of primary crack in its vicinity, thus retarding the primary crack and forcing the primary crack to propagate in a stable manner. The stresses at the primary crack tip are also reduced. As the critical fracture stress for cleavage is not reached for primary cracks, it results in the prevention of cleavage fracture. After some amount of primary crack propagation, the critical stress for cleavage crack propagation is reached. Therefore cleavage fracture often follows ductile fracture at low temperatures (Fig. 43). Similar prevention of cleavage fracture in primary cracks was also reported in other works [14,67]. Secondary cracks become less pronounced and disappear near 200 °C in the T-L oriented samples due to secondary crack tip blunting. At this point, the primary crack propagation becomes unstable as the primary crack propagates freely. Increasing the temperature up to 500 °C reduces the amount of secondary cracks further but leads to an increase in the plasticity at the primary crack tip. This increase in the primary crack tip plasticity counterbalances the primary crack instability created by the lack of secondary cracks. Therefore, the primary crack stabilizes again at higher tempera-

tures. Despite these effects of secondary cracks, more investigations are needed with respect to component fracture testing as secondary cracks initiate earlier than the primary crack at lower loads.

5.3.3 Understanding of secondary cracking in hot-extruded ODS steels

For hot-extruded materials, the constraint induced stress is the highest in the L-C oriented specimens. This is due to the high main stresses in the L-C orientation (Fig. 39c and Fig. 40c) as a consequence of the higher primary crack blunting (higher fracture toughness) in this orientation [131]. In the L-C orientation, the primary fracture plane is the CR plane (Fig. 74b). The secondary crack initiating on this plane will propagate in the C (in-plane) and the L (depth) directions. Void nucleation and growth in the ductile regime is easiest along the extrusion direction (L) due to arrangement of sub-micron particles parallel to the extrusion direction. <110> crystallographic texture with respect to the extrusion direction (Fig. 25 and Fig. 33) and UFG zones elongated in the extrusion direction also aid the crack propagation in the L direction. Due to these reasons, the secondary crack can grow easily in depth (L) direction but finds it difficult to propagate in the in-plane (C) direction. As secondary crack propagation in both directions is inter-dependent, this results in a large critical fracture stress (σ_f) on the CL plane. The high constraint induced stress (σ_C) in the L-C orientation (Fig. 39c and Fig. 40c) is only partially able to overcome the critical fracture stress at some locations (Eq. 24). As soon as a secondary crack forms, σ_C drops and goes below σ_f, arresting the secondary crack. Partially formed secondary cracks are therefore observed arrested in the in-plane (C) direction (Fig. 53 and Fig. 59). At low temperatures, trans-granular cleavage should dominate, but only a few grains with {100} cleavage planes parallel to secondary crack plane (CL) are observed (Fig. 25 and Fig. 33). This is due to the general symmetry of hot-extruded materials where grains with {100} cleavage planes are distributed uniformly around the extrusion axis. Therefore, cleavage fracture for secondary cracks is prevented up to a lower temperature as compared with ODS-KIT HR.

In the C-R orientation, the constraint induced stress (σ_C) is similar (ODS-KIT HE) (Fig. 39c) or slightly lower (ODS-CSM) (Fig. 40c) than in the L-C orientation. The primary fracture plane is the RL plane (Fig. 74). The secondary crack initiating on this plane will propagate in the R (in-plane) and the C (depth) directions. Secondary crack propagation is difficult in both these directions as there is no preferential arrangement of sub-micron particles or ultra-fine grains along these directions and there is also no preferential crystallographic orientation along these directions. Hence the critical fracture stress (σ_f) for secondary cracks is the highest for the RL plane. The constraint induced stress σ_C cannot exceed the high σ_f and no secondary cracks are seen (Eq. 24 is not fulfilled).

In the C-L orientation, the constraint induced stress is lower as compared with the L-C orientation (Fig. 39c and Fig. 40c). The primary fracture plane is the LR plane (Fig. 74). The secondary crack initiating on this plane will propagate in the L (in-plane) and the C (depth) directions. Crack propagation is easier in the in-plane L direction but difficult in the depth C direction. The critical fracture

stress (σ_f) is low in the C-L orientation but due to the low constrained induced stress (σ_C), Eq. 24 is not fulfilled and no secondary cracks are formed.

5.3.4 Comparison

Previous works also confirm that the hot-extruded materials have lesser propensity towards secondary cracking than hot-rolled materials [29,71,76–78]. The difference in secondary cracking between hot-rolled and hot-extruded materials investigated in this research originates from the following factors:

- Crystallographic texture: In ODS-KIT HR, the {100} cleavage planes, which assists cleavage fracture at low temperatures, are parallel to the rolling plane. This is the same plane where the secondary cracks operate. This is not the case in hot-extruded materials, where due to the manufacturing process, the {100} cleavage planes are uniformly distributed around the extrusion axis. The <110> texture in the direction of rolling/extrusion on the other hand, affects all the materials similarly.
- Grain morphology: In ODS-KIT HR, the critical fracture stresses for secondary crack initiation are lower due to two dimensional anisotropic grain elongations in the rolling and in the transverse directions. This favours free crack propagation in two directions which coincides with the directions of secondary crack propagation. In hot-extruded materials, only one dimensional anisotropic grain elongation in the direction of extrusion exists which is unable to support pronounced secondary cracking.
- Particle distribution: The sub-micron particles responsible for void growth and coalescence in the ductile regime are arranged in the rolling/extrusion direction for all the materials. In ODS-KIT HR, the sub-micron particles are also arranged along the transverse direction providing additional support for the secondary crack formation. This effect is in synergy with the effect by anisotropic grain morphology.

Additionally, the constraint induced stresses in ODS-KIT HR are higher than in the two hot-extruded materials (Fig. 41b and d). The higher the constraint induced stress is, the higher the possibility of secondary cracking is. Hence, overall, hot-rolled materials are more prone to secondary cracking than hot-extruded materials. The consequence of partial or no secondary crack formation in hot-extruded specimen is unstable primary crack propagation induced by trans-granular cleavage which was observed in the C-R and C-L orientations at RT. In hot-rolled specimens, secondary cracks prevents unstable crack propagation at low temperatures as discussed in section 5.3.2 and as reported earlier in reference [47].

Which of the above mentioned factors is dominantly responsible for pronounced secondary cracking in ODS-KIT HR depends on the testing temperature with respect to the DBTT of the material. At test temperatures lower than the DBTT, the {100} cleavage planes play a dominant role. At test temperatures above the DBTT, the anisotropic grain morphology plays a major role while anisotropic particle

distribution provides only a minor contribution. Similar conclusions about grain morphology were made from the discussion in section 5.2.4 [131].

5.4 Assessment of variation in fracture toughness

It is observed that from RT to 400 ˚C, ODS-KIT HE consistently exhibits higher fracture toughness than ODS-KIT HR and ODS-CSM in all three orientations (Fig. 38a, Fig. 39a and Fig. 40a). In fact, the fracture toughness values in the strongest orientation (L-C) are even higher than that of other ODS steels [7] and P91 steel investigated before (Fig. 41a).

In order to investigate the factors responsible for the high fracture toughness, two hot-extruded ODS steels, ODS-KIT HE and ODS-CSM, are compared in the C-L orientation. At 200 ˚C, Eq. 20 for ductile fracture can be used for both materials to separate the relative contributions of the yield stress, the inter-particle spacing, the size of the sub-micron particle and the interfacial bond strength between the sub-micron particle and matrix. Eq. 25 displays the separated ratios. The Burgers vector is assumed to be similar for both the materials as both have a BCC Fe matrix. As both the materials have similar composition and similar preferential orientation of grains in the <110> direction parallel to the extrusion direction, it is reasonable to assume that for the C-L orientation, the shear moduli of both materials are similar. The contribution from crack blunting (explained in section 5.2.3) is also assumed to be similar for both the materials in the C-L orientation as crack growth is the easiest in this direction.

$$\frac{J_{IC}^{KIT\ HE}}{J_{IC}^{CSM}} = \frac{\sigma_0^{KIT\ HE}}{\sigma_0^{CSM}} * \frac{l_{KIT\ HE}^2}{l_{CSM}^2} * \frac{d_{CSM}}{d_{KIT\ HE}} * \frac{W_{KIT\ HE}}{W_{CSM}} \tag{25}$$

Table 12 Relative contributions of the microstructural factors towards fracture toughness at 200 ˚C in the C-L orientation of ODS-KIT HE and ODS-CSM (Eq. 25).

Orientation	$\frac{J_{IC}^{KIT\ HE}}{J_{IC}^{CSM}}$	$\frac{\sigma_0^{KIT\ HE}}{\sigma_0^{CSM}}$	$\frac{l_{KIT\ HE}^2}{l_{CSM}^2}$	$\frac{d_{CSM}}{d_{KIT\ HE}}$	$\frac{W_{KIT\ HE}}{W_{CSM}}$
C-L	9.89	1.14	0.15	4.2	13.8

5.4.1 Yield stress (σ_0)

The yield and ultimate tensile strength of ODS-KIT HE is higher than that of ODS-CSM (Fig. 37a) in the longitudinal direction in the temperature range of RT to 400 ˚C. This contributes towards fracture toughness in ductile fracture (Eq. 18). It was reported in other works that the yield stress in the transverse orientation is similar to the yield stress in the longitudinal orientation [39,71]. The yield stress depends on how effective the nano-particles are in obstructing dislocations. The size and the inter-particle spacing of the nano-particles are important parameters contributing to this effectiveness. The fact that ODS-KIT was produced by a Fe_3Y precursor while ODS-CSM was produced by a Y_2O_3 precursor can have an effect on the composition of nano-particles and their ability to ob-

struct dislocations, but this was not confirmed through experimental investigations. A similar precursor Fe_2Y however, used in other works, led to formation of nano-particles similar to the ones obtained from the Y_2O_3 precursor [132] and resulted in similar yield strength as from the Y_2O_3 precursor at all temperatures [133]. Kim et al. [54] observed the nano-particles to be present on the grain boundaries. However, in this research, the nano-particles of the materials investigated had no preferential location and are inhomogenously distributed in HD and LD regions. Through TEM micrographs, it is found that the inter-particle spacing of the nano-particles in the HD regions of both materials is similar (inter-particle spacing: 10 nm and volume fraction: 0.148). However, ODS-KIT HE has a slightly smaller average nano-particle size (3 nm) than ODS-CSM (8 nm). Therefore the strengthening induced by the nano-particles is more pronounced in ODS-KIT HE.

Strengthening is also dependent on the grain size through the Hall-Petch strengthening relation [54]. The fine grains in both the materials exhibit similar sizes (0.65 µm). However, the coarse grains of ODS-KIT HE (4.7 µm) are larger than the coarse grains of ODS-CSM (2.1 µm). The contribution from Hall-Petch strengthening to the yield stress is therefore more pronounced in ODS-CSM than in ODS-KIT HE.

Dislocation forest strengthening, which depends on the interaction of moving and dislocations arising from the initial severe plastic deformation and processing steps thereafter, has a greater contribution towards yield stress resulting in higher yield stress in ODS-KIT HE. This is because ODS-KIT HE was manufactured with a higher extrusion ratio than ODS-CSM, thus inducing more dislocations.

Contributions through grain matrix hardening [54], which includes both solid solution and intrinsic lattice friction strengthening, might be similar in both materials owing to the similar composition of both the materials. The yield stress ratio between ODS-KIT HE and ODS-CSM at 200 ˚C only amounts to a value of 1.14 (Table 12) which is far less than the fracture toughness ratio of 9.89 in the C-L orientation.

5.4.2 Void initiating sub-micron particle size and inter-particle spacing (d and l)

The larger the inter-particle spacing (l) and the smaller the particle size (d) is, the higher the fracture toughness is (Eq. 20). The effective inter-particle spacing and the effective mean size in the C-L orientation of both the materials are calculated using Eq. 22 and Eq. 23, respectively and their ratios are presented in Table 12. The ratio of the inter-particle spacing lowers the fracture toughness ratio because the inter-particle spacing of ODS-CSM is larger than that of ODS-KIT HE (Table 5). The smaller sub-micron particle size of ODS-KIT HE however, proves to be beneficial for the fracture toughness ratio. These contributions however still cannot explain the high experimental fracture toughness of ODS-KIT HE as compared to ODS-CSM ($\frac{J_{IC}^{KIT\ HE}}{J_{IC}^{CSM}} = 9.89$) in the C-L orientation.

5.4.3 Particle-matrix bond strength (W)

The particle-matrix bond strength depends on the chemical composition of the sub-micron particle and the matrix. The higher this bond strength is, the higher the fracture toughness is. It is reasonable to assume that the Ti-enriched sub-micron particles in ODS-KIT HE and Si, O-enriched sub-micron particles in ODS-CSM have different values of W. This affects the fracture toughness differently. The high experimental fracture toughness of ODS-KIT HE as compared to ODS-CSM can only be explained if the interfacial particle-matrix strength of ODS-KIT HE is higher than that of ODS-CSM. This ratio is determined using the known ratios (Table 12) of the fracture toughness, the yield stress, the inter-particle spacing and the particle size in Eq. 25 and is solved for the interfacial particle-matrix strength ratio. It is seen from the above analysis that the highest contribution to the fracture toughness in ODS-KIT HE comes from the interfacial particle-matrix strength. It can also be concluded that the interfacial particle-matrix strength of Ti particles with ODS-KIT HE matrix is higher than Si and O particles with ODS-CSM matrix. This should however, be confirmed with direct experimental or simulation based investigations in the future.

5.4.4 Other contributors

The Cr enrichments at the grain boundaries may additionally contribute to the lower fracture toughness in ODS-CSM. The crack propagation in the L-C orientation of ODS-CSM exhibits slant fracture (Fig. 70a and b) at the specimen surface which is characteristic of shear instability [95]. The plane stress condition on the crack front close to the free surfaces possibly results in such fracture behaviour. On the other hand, a relatively straight zig-zag crack front towards the middle of the crack front is observed (Fig. 70c, d, e and Fig. 71b). Due to the plane strain condition in the middle of the crack front, the shear instability reduces. It was reported that shear instability takes place in materials with low strain hardening capacity and involves much less plastic work than a full void growth and coalescence [95]. This can also be a reason contributing to the low fracture toughness of ODS-CSM.

Although the particle-matrix bond strength of ODS-KIT HR should be the same as ODS-KIT HE, the morphology of grains is completely different. Therefore the fracture toughness of these materials cannot be compared. Fig. 41b shows that the load maximum of ODS-KIT HR at 200 ˚C is higher than that of ODS-KIT HE. However, ODS-KIT HR still exhibits lower fracture toughness than ODS-KIT HE due to lower ductility or lesser area under the curve and higher crack growth for the same load line displacement (Fig. 41c). This lower ductility in ODS-KIT HR is due to the different grain morphology, different arrangement of sub-micron particles, and an extensive arrangement of voids and pores in the rolling and transverse directions as compared with ODS-KIT HE.

6 Conclusions

The fracture behaviour of three ferritic ODS steels were investigated using microstructural characterization techniques. The following are the major conclusions from this work:

Fracture toughness

- The fracture toughness of a material is dependent on the critical fracture strain and hence on the microstructural parameters such as the size of the sub-micron particle, the inter-particle spacing, the sub-micron particle-matrix bond strength, the yield stress, the shear modulus and the Burgers vector.
- Sub-micron particles are mainly responsible for ductile fracture through void growth and coalescence while nano-particles do not play a direct role in the ductile fracture mechanism.
- In the temperature range from RT to 400 ˚C, fracture toughness is dominantly affected by the sub-micron particle-matrix interfacial strength. The sub-micron particle-matrix interfacial strength between Si-enriched particle and matrix is lower than Ti-enriched particle and matrix. This leads to lower fracture toughness in ODS-CSM.
- Cr segregations at the grain boundaries and shear instability during crack propagation can lower the fracture toughness as was the case with ODS-CSM
- Large sub-micron particle size and small inter-particle spacing also contribute towards low fracture toughness but are not the dominant factors.
- Low value of yield stress is the least dominant factor contributing towards low fracture toughness.

Fracture anisotropy

- The anisotropic fracture behaviour observed in all the three ODS steels is due to the anisotropic crystallographic texture, the anisotropic sub-micron particle distribution and the anisotropic grain morphology.
- Primary cracks propagate preferentially through the fine-grained region. The fine-grained regions consist of UFGs which have lower ductility than coarse grains. The UFGs initiate voids after reaching their yield stress later during loading while the coarse grains reach their yield stress earlier but are able to deform.
- Anisotropic grain morphology is the dominant contributor towards fracture toughness anisotropy. In the L-C and L-T orientations, the elongated coarse grains are perpendicular to the crack propagation direction, which induces crack blunting and high energy absorption. Crack deviation through low resistance paths in the C-R and C-L/T-L orientations leads to lesser energy absorption as compared with crack blunting.
- Arrangement and morphology of pre-existing pores and microcracks in the rolling/extrusion direction also lowers the fracture toughness in the T-L and C-L oriented specimens.

- The shear modulus is the lowest in (110) planes which, due to the <110> texture with respect to the rolling/extrusion direction, correspond to the L-C orientation. In hot-extruded materials, the other perpendicular directions are considered isotropic with no texture. The ratio of the minimum shear modulus parallel to the extrusion direction to the isotropic shear modulus in the perpendicular direction for hot-extruded materials indicates that crystallographic texture is not the dominant factor affecting the fracture toughness anisotropy. Similar conclusions can be made for hot-rolled materials.
- The anisotropy in nano-particle distribution does not have any effect on the yield stress and fracture toughness of the materials in different orientations.
- The flat regions on fracture surfaces are not due to debonding of oxide coated prior particle boundaries but due to large inter-particle spacing of sub-micron particles in local regions.
- It was observed that the inter-particle spacing of the sub-micron particles and the sub-micron particle size has an effect on the fracture toughness anisotropy but they do not contribute dominantly.
- The intersection of the crack planes with the arranged sub-micron particles in the LD and HD regions allows calculation of the effective inter-particle spacing and the effective particle size for a particular orientation. A parallel combination analogous to a parallel mechanical spring system was considered for C-L and T-L orientation. For L-C, C-R and L-T orientations, the crack was assumed to always be in the LD region.
- Fracture toughness of ODS-KIT HR is lower than ODS-KIT HE due to the two-dimensional microstructural anisotropy towards the rolling and transverse direction as compared with the one-dimensional microstructural anisotropy of ODS-KIT HE towards the extrusion direction.

Secondary cracking

- At temperatures below the DBTT, the occurrence of secondary cracks in hot-rolled materials is assisted by the {100} cleavage planes which are aligned parallel to the rolling plane. In hot-extruded materials, these {100} cleavage planes are distributed uniformly around the extrusion axis hindering secondary cracking.
- At temperatures higher than the DBTT, secondary cracking via void growth and coalescence is more frequent in hot-rolled than in hot-extruded materials as the critical fracture stresses in secondary crack planes are lower due to the two dimensionally anisotropic elongated 'pan-cake' shaped grains which allows free crack propagation in two directions. In hot-extruded materials, the one dimensional 'cigar' like grain morphology with grains elongated in the direction of extrusion only allows free crack propagation in one direction and hence hinders secondary cracking.
- At temperatures higher than the DBTT, the sub-micron particle anisotropy also affects secondary cracking. Sub-micron particle arrangement in two directions assists secondary cracking

more in hot-rolled material than one dimensional sub-micron particle arrangement in hot-extruded materials.

- The constraint induced stress in the hot-rolled material is higher than in hot-extruded materials which also assist in higher degree of secondary cracking in hot-rolled materials.
- In ODS-KIT HR, secondary crack propagation is more pronounced in the L-T orientation than in the T-L orientation due to the higher constraint induced stress available for its growth.
- In ODS-KIT HR at RT, secondary cracking arise predominantly through cleavage and inter-granular fracture possibly due to segregations at the grain boundary. Between RT and 600 ˚C, secondary cracking arise through transgranular ductile fracture and at or above 600 ˚C, secondary cracking takes place through intergranular fracture due to the weakening of the grain boundaries.
- Secondary cracks are able to stabilize the primary crack propagation as well as prevent cleavage fracture at low temperatures. However, they initiate at lower loads than the primary crack.

Bibliography

[1] S. Chu, A. Majumdar, Opportunities and challenges for a sustainable energy future, Nature. 488 (2012) 294–303. doi:10.1038/nature11475.

[2] U.S. DOE nuclear energy research advisory committee, Generation IV international forum, A technology roadmap for generation IV nuclear energy systems, 2012.

[3] C. Capdevila, H.K.D.H. Bhadeshia, Manufacturing and microstructural evolution of mechanically alloyed oxide dispersion strengthened superalloys, Adv. Eng. Mater. 3 (2001) 647–656. doi:10.1002/1527-2648(200109)3:9<647::AID-ADEM647>3.0.CO;2-4.

[4] P. Dubuisson, Y. de Carlan, V. Garat, M. Blat, ODS ferritic/martensitic alloys for sodium fast reactor fuel pin cladding, J. Nucl. Mater. 428 (2012) 6–12. doi:10.1016/j.jnucmat.2011.10.037.

[5] A. Shirazdi, S. Jackson, eds., Structural alloys for power plants - Operational challenges and high-temperature materials, Woodhead Publishing, Cambridge, UK, 2014.

[6] P. He, On the structure-property correlation and the evolution of Nanofeatures in 12-13.5% Cr oxide dispersion strengthened ferritic steels, KIT Scientific Publishing, Karlsruhe, Baden, 2013.

[7] T.S. Byun, D.T. Hoelzer, J.H. Kim, S.A. Maloy, A comparative assessment of the fracture toughness behavior of ferritic-martensitic steels and nanostructured ferritic alloys, J. Nucl. Mater. 484 (2017) 157–167. doi:10.1016/j.jnucmat.2016.12.004.

[8] ITER - the way to new energy, ITER. (n.d.). http://www.iter.org (accessed April 9, 2018).

[9] S.J. Zinkle, J.T. Busby, Structural materials for fission & fusion energy, Mater. Today. 12 (2009) 12–19. doi:10.1016/S1369-7021(09)70294-9.

[10] G.J. Butterworth, O.N. Jarvis, Comparison of transmutation and activation effects in five ferritic alloys and AISI 316 stainless steel in a fusion neutron spectrum, J. Nucl. Mater. 123 (1984) 982–988. doi:10.1016/0022-3115(84)90205-8.

[11] G.R. Odette, M.J. Alinger, B.D. Wirth, Recent developments in irradiation-resistant steels, Annu. Rev. Mater. Res. 38 (2008) 471–503. doi:10.1146/annurev.matsci.38.060407.130315.

[12] H. Schroeder, H. Ullmaier, Helium and hydrogen effects on the embrittlement of iron- and nickel-based alloys, J. Nucl. Mater. 179 (1991) 118–124. doi:10.1016/0022-3115(91)90025-3.

[13] S.J. Zinkle, Fusion materials science: Overview of challenges and recent progress, Phys. Plasmas. 12 (2005) 058101. doi:10.1063/1.1880013.

[14] G.R. Odette, Recent progress in developing and qualifying nanostructured ferritic alloys for advanced fission and fusion applications, JOM. 66 (2014) 2427–2441. doi:10.1007/s11837-014-1207-5.

[15] R.L. Klueh, E.E. Bloom, The development of ferritic steels for fast induced-radioactivity decay for fusion reactor applications, Nucl. Eng. Des. Fusion. 2 (1985) 383–389. doi:10.1016/0167-899X(85)90026-6.

[16] R.L. Klueh, D.S. Gelles, T.A. Lechtenberg, Development of ferritic steels for reduced activation: The US program, J. Nucl. Mater. 141 (1986) 1081–1087. doi:10.1016/0022-3115(86)90146-7.

[17] S. Ukai, M. Harada, H. Okada, M. Inoue, S. Nomura, S. Shikakura, T. Nishida, M. Fujiwara, K. Asabe, Tube manufacturing and mechanical properties of oxide dispersion strengthened ferritic steel, J. Nucl. Mater. 204 (1993) 74–80. doi:10.1016/0022-3115(93)90201-9.

[18] D.K. Mukhopadhyay, F.H. Froes, D.S. Gelles, Development of oxide dispersion strengthened ferritic steels for fusion, J. Nucl. Mater. 258 (1998) 1209–1215. doi:10.1016/S0022-3115(98)00188-3.

[19] T. Okuda, M. Fujiwara, Dispersion behaviour of oxide particles in mechanically alloyed ODS steel, J. Mater. Sci. Lett. 14 (1995) 1600–1603. doi:10.1007/BF00455428.

[20] M.J. Alinger, G.R. Odette, D.T. Hoelzer, On the role of alloy composition and processing parameters in nanocluster formation and dispersion strengthening in nanostuctured ferritic alloys, Acta Mater. 57 (2009) 392–406. doi:10.1016/j.actamat.2008.09.025.

[21] M.K. Miller, D.T. Hoelzer, E.A. Kenik, K.F. Russell, Nanometer scale precipitation in ferritic MA/ODS alloy MA957, J. Nucl. Mater. 329–333, Part A (2004) 338–341. doi:10.1016/j.jnucmat.2004.04.085.

[22] T.S. Byun, J.H. Yoon, S.H. Wee, D.T. Hoelzer, S.A. Maloy, Fracture behavior of 9Cr nanostructured ferritic alloy with improved fracture toughness, J. Nucl. Mater. 449 (2014) 39–48. doi:10.1016/j.jnucmat.2014.03.007.

[23] M.A. Sokolov, D.T. Hoelzer, R.E. Stoller, D.A. McClintock, Fracture toughness and tensile properties of nano-structured ferritic steel 12YWT, J. Nucl. Mater. 367-370 (2007) 213–216. doi:10.1016/j.jnucmat.2007.03.143.

[24] C.C. Eiselt, M. Klimenkov, R. Lindau, A. Möslang, G.R. Odette, T. Yamamoto, D. Gragg, Tensile and fracture toughness properties of the nanostructured oxide dispersion strengthened ferritic alloy 13Cr–1W–0.3Ti–0.3Y2O3, J. Nucl. Mater. 417 (2011) 193–196. doi:10.1016/j.jnucmat.2010.12.066.

[25] A. Steckmeyer, M. Praud, B. Fournier, J. Malaplate, J. Garnier, J.L. Béchade, I. Tournié, A. Tancray, A. Bougault, P. Bonnaillie, Tensile properties and deformation mechanisms of a 14Cr ODS ferritic steel, J. Nucl. Mater. 405 (2010) 95–100. doi:10.1016/j.jnucmat.2010.07.027.

[26] Z. Oksiuta, P. Mueller, P. Spätig, N. Baluc, Effect of thermo-mechanical treatments on the microstructure and mechanical properties of an ODS ferritic steel, J. Nucl. Mater. 412 (2011) 221–226. doi:10.1016/j.jnucmat.2011.03.006.

[27] Z. Oksiuta, P. Hosemann, S.C. Vogel, N. Baluc, Microstructure examination of Fe–14Cr ODS ferritic steels produced through different processing routes, J. Nucl. Mater. 451 (2014) 320–327. doi:10.1016/j.jnucmat.2014.04.004.

[28] D.T. Hoelzer, J. Bentley, M.A. Sokolov, M.K. Miller, G.R. Odette, M.J. Alinger, Influence of particle dispersions on the high-temperature strength of ferritic alloys, J. Nucl. Mater. 367–370, Part A (2007) 166–172. doi:10.1016/j.jnucmat.2007.03.151.

[29] H. Hadraba, B. Fournier, L. Stratil, J. Malaplate, A.-L. Rouffié, P. Wident, L. Ziolek, J.-L. Béchade, Influence of microstructure on impact properties of 9–18%Cr ODS steels for fusion/fission applications, J. Nucl. Mater. 411 (2011) 112–118. doi:10.1016/j.jnucmat.2011.01.038.

[30] R.L. Klueh, P.J. Maziasz, I.S. Kim, L. Heatherly, D.T. Hoelzer, N. Hashimoto, E.A. Kenik, K. Miyahara, Tensile and creep properties of an oxide dispersion-strengthened ferritic steel, J. Nucl. Mater. 307–311, Part 1 (2002) 773–777. doi:10.1016/S0022-3115(02)01046-2.

[31] S. Ukai, M. Harada, H. Okada, M. Inoue, S. Nomura, S. Shikakura, K. Asabe, T. Nishida, M. Fujiwara, Alloying design of oxide dispersion strengthened ferritic steel for long life FBRs core materials, J. Nucl. Mater. 204 (1993) 65–73.

[32] P. He, M. Klimenkov, R. Lindau, A. Möslang, Characterization of precipitates in nano structured 14% Cr ODS alloys for fusion application, J. Nucl. Mater. 428 (2012) 131–138. doi:10.1016/j.jnucmat.2011.08.026.

[33] R. Kasada, N. Toda, K. Yutani, H.S. Cho, H. Kishimoto, A. Kimura, Pre- and post-deformation microstructures of oxide dispersion strengthened ferritic steels, J. Nucl. Mater. 367 (2007) 222–228. doi:10.1016/j.jnucmat.2007.03.141.

[34] J. Ribis, Y. de Carlan, Interfacial strained structure and orientation relationships of the nanosized oxide particles deduced from elasticity-driven morphology in oxide dispersion strengthened materials, Acta Mater. 60 (2012) 238–252. doi:10.1016/j.actamat.2011.09.042.

[35] L. Barnard, G.R. Odette, I. Szlufarska, D. Morgan, An ab initio study of Ti–Y–O nanocluster energetics in nanostructured ferritic alloys, Acta Mater. 60 (2012) 935–947. doi:10.1016/j.actamat.2011.11.011.

[36] F. Bergner, I. Hilger, J. Virta, J. Lagerbom, G. Gerbeth, S. Connolly, Z. Hong, P.S. Grant, T. Weissgärber, Alternative fabrication routes toward oxide-dispersion-strengthened steels and model alloys, Metall. Mater. Trans. A. 47 (2016) 5313–5324. doi:10.1007/s11661-016-3616-2.

[37] S. Ukai, M. Fujiwara, Perspective of ODS alloys application in nuclear environments, J. Nucl. Mater. 307 (2002) 749–757.

[38] T. Chen, E. Aydogan, J.G. Gigax, D. Chen, J. Wang, X. Wang, S. Ukai, F.A. Garner, L. Shao, Microstructural changes and void swelling of a 12Cr ODS ferritic-martensitic alloy after high-dpa self-ion irradiation, J. Nucl. Mater. 467 (2015) 42–49. doi:10.1016/j.jnucmat.2015.09.016.

[39] M.J. Alinger, G.R. Odette, G.E. Lucas, Tensile and fracture toughness properties of MA957: implications to the development of nanocomposited ferritic alloys, J. Nucl. Mater. 307–311, Part 1 (2002) 484–489. doi:10.1016/S0022-3115(02)01220-5.

[40] R.L. Klueh, J.P. Shingledecker, R.W. Swindeman, D.T. Hoelzer, Oxide dispersion-strengthened steels: A comparison of some commercial and experimental alloys, J. Nucl. Mater. 341 (2005) 103–114. doi:10.1016/j.jnucmat.2005.01.017.

[41] A. Wang, P.F. Thomson, P.D. Hodgson, A study of pore closure and welding in hot rolling process, J. Mater. Process. Technol. 60 (1996) 95–102. doi:10.1016/0924-0136(96)02313-8.

[42] J.H. Kim, T.S. Byun, D.T. Hoelzer, Tensile fracture characteristics of nanostructured ferritic alloy 14YWT, J. Nucl. Mater. 407 (2010) 143–150. doi:10.1016/j.jnucmat.2010.09.054.

[43] I. Hilger, F. Bergner, T. Weißgärber, Bimodal grain size distribution of nanostructured ferritic ODS Fe–Cr alloys, J. Am. Ceram. Soc. 98 (2015) 3576–3581. doi:10.1111/jace.13833.

[44] H. OKADA, S. UKAI, M. INOUE, Effects of Grain Morphology and Texture on High Temperature Deformation in Oxide Dispersion Strengthened Ferritic Steels, J. Nucl. Sci. Technol. 33 (1996) 936–943. doi:10.1080/18811248.1996.9732035.

[45] M. Lewandowska, K.J. Kurzydlowski, Recent development in grain refinement by hydrostatic extrusion, J. Mater. Sci. 43 (2008) 7299–7306. doi:10.1007/s10853-008-2810-z.

[46] S. Ukai, W. Izawa, N. Oono, S. Hayashi, Y. Kohno, S. Ohtsuka, T. Kaito, Charpy impact property related to 100 cleavage fracture in 15CrODS steel, Mater. Sci. Technol. 30 (2014) 1709–1714. doi:10.1179/1743284714Y.0000000604.

[47] A. Das, H.W. Viehrig, F. Bergner, C. Heintze, E. Altstadt, J. Hoffmann, Effect of microstructural anisotropy on fracture toughness of hot rolled 13Cr ODS steel – The role of primary and secondary cracking, J. Nucl. Mater. 491 (2017) 83–93. doi:10.1016/j.jnucmat.2017.04.059.

[48] B. Fournier, A. Steckmeyer, A.-L. Rouffie, J. Malaplate, J. Garnier, M. Ratti, P. Wident, L. Ziolek, I. Tournie, V. Rabeau, J.M. Gentzbittel, T. Kruml, I. Kubena, Mechanical behaviour of ferritic ODS steels – Temperature dependancy and anisotropy, J. Nucl. Mater. 430 (2012) 142–149. doi:10.1016/j.jnucmat.2012.05.048.

[49] R. Jamaati, M.R. Toroghinejad, M.A. Mohtadi-Bonab, H. Edris, J.A. Szpunar, M.R. Salmani, Texture development of ARB-processed steel-based nanocomposite, J. Mater. Eng. Perform. 23 (2014) 4436–4445. doi:10.1007/s11665-014-1233-z.

[50] E. Aydogan, S. Pal, O. Anderoglu, S.A. Maloy, S.C. Vogel, G.R. Odette, J.J. Lewandowski, D.T. Hoelzer, I.E. Anderson, J.R. Rieken, Effect of tube processing methods on the texture and grain boundary characteristics of 14YWT nanostructured ferritic alloys, Mater. Sci. Eng. A. 661 (2016) 222–232. doi:10.1016/j.msea.2016.02.085.

[51] A. Chauhan, F. Bergner, A. Etienne, J. Aktaa, Y. de Carlan, C. Heintze, D. Litvinov, M. Hernandez-Mayoral, E. Oñorbe, B. Radiguet, A. Ulbricht, Microstructure characterization and

strengthening mechanisms of oxide dispersion strengthened (ODS) Fe-9%Cr and Fe-14%Cr extruded bars, J. Nucl. Mater. 495 (2017) 6–19. doi:10.1016/j.jnucmat.2017.07.060.

[52] J.H. Kim, T.S. Byun, D.T. Hoelzer, High temperature deformation mechanisms of nanostructured ferritic alloys in the context of internal variable theory of inelastic deformation, J. Nucl. Mater. 442 (2013) 458–462. doi:10.1016/j.jnucmat.2013.02.048.

[53] J. Rösler, E. Arzt, A new model-based creep equation for dispersion strengthened materials, Acta Metall. Mater. 38 (1990) 671–683. doi:10.1016/0956-7151(90)90223-4.

[54] J.H. Kim, T.S. Byun, D.T. Hoelzer, C.H. Park, J.T. Yeom, J.K. Hong, Temperature dependence of strengthening mechanisms in the nanostructured ferritic alloy 14YWT: Part II—Mechanistic models and predictions, Mater. Sci. Eng. A. 559 (2013) 111–118. doi:10.1016/j.msea.2012.08.041.

[55] A. Steckmeyer, V.H. Rodrigo, J.M. Gentzbittel, V. Rabeau, B. Fournier, Tensile anisotropy and creep properties of a Fe–14CrWTi ODS ferritic steel, J. Nucl. Mater. 426 (2012) 182–188. doi:10.1016/j.jnucmat.2012.03.016.

[56] J. Malaplate, F. Mompiou, J.-L. Béchade, T. Van Den Berghe, M. Ratti, Creep behavior of ODS materials: A study of dislocations/precipitates interactions, J. Nucl. Mater. 417 (2011) 205–208. doi:10.1016/j.jnucmat.2010.12.059.

[57] R.L. Klueh, A.T. Nelson, Ferritic/martensitic steels for next-generation reactors, J. Nucl. Mater. 371 (2007) 37–52. doi:10.1016/j.jnucmat.2007.05.005.

[58] A. Alamo, V. Lambard, X. Averty, M.H. Mathon, Assessment of ODS-14%Cr ferritic alloy for high temperature applications, J. Nucl. Mater. 329–333, Part A (2004) 333–337. doi:10.1016/j.jnucmat.2004.05.004.

[59] A. Hasegawa, M. Ejiri, S. Nogami, M. Ishiga, R. Kasada, A. Kimura, K. Abe, S. Jitsukawa, Effects of helium on ductile-brittle transition behavior of reduced-activation ferritic steels after high-concentration helium implantation at high temperature, J. Nucl. Mater. 386 (2009) 241–244. doi:10.1016/j.jnucmat.2008.12.102.

[60] K. Yutani, H. Kishimoto, R. Kasada, A. Kimura, Evaluation of Helium effects on swelling behavior of oxide dispersion strengthened ferritic steels under ion irradiation, J. Nucl. Mater. 367 (2007) 423–427. doi:10.1016/j.jnucmat.2007.03.016.

[61] D.A. McClintock, D.T. Hoelzer, M.A. Sokolov, R.K. Nanstad, Mechanical properties of neutron irradiated nanostructured ferritic alloy 14YWT, J. Nucl. Mater. 386–388 (2009) 307–311. doi:10.1016/j.jnucmat.2008.12.104.

[62] A. Kimura, H.-S. Cho, N. Toda, R. Kasada, K. Yutani, H. Kishimoto, N. Iwata, S. Ukai, M. Fujiwara, High burnup fuel cladding materials R&D for advanced nuclear systems, J. Nucl. Sci. Technol. 44 (2007) 323–328. doi:10.1080/18811248.2007.9711289.

[63] R. Lindau, A. Möslang, M. Schirra, P. Schlossmacher, M. Klimenkov, Mechanical and microstructural properties of a hipped RAFM ODS-steel, J. Nucl. Mater. 307–311, Part 1 (2002) 769–772. doi:10.1016/S0022-3115(02)01045-0.

[64] Z. Dapeng, L. Yong, L. Feng, W. Yuren, Z. Liujie, D. Yuhai, ODS ferritic steel engineered with bimodal grain size for high strength and ductility, Mater. Lett. 65 (2011) 1672–1674. doi:10.1016/j.matlet.2011.02.064.

[65] M.A. Auger, T. Leguey, A. Muñoz, M.A. Monge, V. de Castro, P. Fernández, G. Garcés, R. Pareja, Microstructure and mechanical properties of ultrafine-grained Fe–14Cr and ODS Fe–14Cr model alloys, J. Nucl. Mater. 417 (2011) 213–216. doi:10.1016/j.jnucmat.2010.12.060.

[66] T.S. Byun, J.H. Kim, J.H. Yoon, D.T. Hoelzer, High temperature fracture characteristics of a nanostructured ferritic alloy (NFA), J. Nucl. Mater. 407 (2010) 78–82. doi:10.1016/j.jnucmat.2010.09.031.

[67] M.E. Alam, S. Pal, S.A. Maloy, G.R. Odette, On delamination toughening of a 14YWT nanostructured ferritic alloy, Acta Mater. 136 (2017) 61–73. doi:10.1016/j.actamat.2017.06.041.

[68] J.H. Kim, T.S. Byun, E. Shin, J.-B. Seol, S. Young, N.S. Reddy, Small angle neutron scattering analyses and high temperature mechanical properties of nano-structured oxide dispersion-strengthened steels produced via cryomilling, J. Alloys Compd. 651 (2015) 363–374. doi:10.1016/j.jallcom.2015.08.100.

[69] D.T. Hoelzer, K.A. Unocic, M.A. Sokolov, T.S. Byun, Influence of processing on the microstructure and mechanical properties of 14YWT, J. Nucl. Mater. 471 (2016) 251–265. doi:10.1016/j.jnucmat.2015.12.011.

[70] R. Chaouadi, G. Coen, E. Lucon, V. Massaut, Crack resistance behavior of ODS and standard 9%Cr-containing steels at high temperature, J. Nucl. Mater. 403 (2010) 15–18. doi:10.1016/j.jnucmat.2010.05.021.

[71] M. Serrano, M. Hernández-Mayoral, A. García-Junceda, Microstructural anisotropy effect on the mechanical properties of a 14Cr ODS steel, J. Nucl. Mater. 428 (2012) 103–109. doi:10.1016/j.jnucmat.2011.08.016.

[72] P. He, R. Lindau, A. Moeslang, H.R.Z. Sandim, The influence of thermomechanical processing on the microstructure and mechanical properties of 13.5Cr ODS steels, Fusion Eng. Des. 88 (2013) 2448–2452. doi:10.1016/j.fusengdes.2013.04.005.

[73] Z. Oksiuta, P. Olier, Y. de Carlan, N. Baluc, Development and characterisation of a new ODS ferritic steel for fusion reactor application, J. Nucl. Mater. 393 (2009) 114–119. doi:10.1016/j.jnucmat.2009.05.013.

[74] J. Chao, C. Capdevila, M. Serrano, A. Garcia-Junceda, J.A. Jimenez, G. Pimentel, E. Urones-Garrote, Notch impact behavior of oxide-dispersion-strengthened (ODS) Fe20Cr5Al alloy, Metall. Mater. Trans. A. 44 (2013) 4581–4594. doi:10.1007/s11661-013-1815-7.

[75] M. Serrano, A. García-Junceda, R. Hernández, M.H. Mayoral, On anisotropy of ferritic ODS alloys, Mater. Sci. Technol. 30 (2014) 1664–1668. doi:10.1179/1743284714Y.0000000552.

[76] A. García-Junceda, M. Hernández-Mayoral, M. Serrano, Influence of the microstructure on the tensile and impact properties of a 14Cr ODS steel bar, Mater. Sci. Eng. A. 556 (2012) 696–703. doi:10.1016/j.msea.2012.07.051.

[77] A.L. Rouffié, P. Wident, L. Ziolek, F. Delabrouille, B. Tanguy, J. Crépin, A. Pineau, V. Garat, B. Fournier, Influences of process parameters and microstructure on the fracture mechanisms of ODS steels, J. Nucl. Mater. 433 (2013) 108–115. doi:10.1016/j.jnucmat.2012.08.050.

[78] R. Kasada, S.G. Lee, J. Isselin, J.H. Lee, T. Omura, A. Kimura, T. Okuda, M. Inoue, S. Ukai, S. Ohnuki, T. Fujisawa, F. Abe, Anisotropy in tensile and ductile–brittle transition behavior of ODS ferritic steels, J. Nucl. Mater. 417 (2011) 180–184. doi:10.1016/j.jnucmat.2010.12.069.

[79] J. Chao, R. Rementeria, M. Aranda, C. Capdevila, J. Gonzalez-Carrasco, Comparison of ductile-to-brittle transition behavior in two similar ferritic oxide dispersion strengthened alloys, Materials. 9 (2016) 637. doi:10.3390/ma9080637.

[80] E. Altstadt, M. Serrano, M. Houska, A. García-Junceda, Effect of anisotropic microstructure of a 12Cr-ODS steel on the fracture behaviour in the small punch test, Mater. Sci. Eng. A. 654 (2016) 309–316. doi:10.1016/j.msea.2015.12.055.

[81] B.L. Bramfitt, A.R. Marder, A study of the delamination behavior of a very low-carbon steel, Metall. Trans. A. 8 (1977) 1263–1273. doi:10.1007/BF02643841.

[82] D.L. Bourell, Cleavage delamination in impact tested warm-rolled steel, Metall. Trans. A. 14 (1983) 2487–2496. doi:10.1007/BF02668890.

[83] F. Ersoy, S. Gavrilov, K. Verbeken, Investigating liquid-metal embrittlement of T91 steel by fracture toughness tests, J. Nucl. Mater. 472 (2016) 171–177. doi:10.1016/j.jnucmat.2015.12.019.

[84] Y. Kimura, T. Inoue, F. Yin, K. Tsuzaki, Delamination toughening of ultrafine grain structure steels processed through tempforming at elevated temperatures, ISIJ Int. 50 (2010) 152–161. doi:10.2355/isijinternational.50.152.

[85] A. Chauhan, D. Litvinov, J. Aktaa, High temperature tensile properties and fracture characteristics of bimodal 12Cr-ODS steel, J. Nucl. Mater. 468 (2016) 1–8. doi:10.1016/j.jnucmat.2015.11.013.

[86] S. Kalyanam, A.J. Beaudoin, R.H. Dodds Jr., F. Barlat, Delamination cracking in advanced aluminum–lithium alloys – Experimental and computational studies, Eng. Fract. Mech. 76 (2009) 2174–2191. doi:10.1016/j.engfracmech.2009.06.010.

[87] J.H. Kim, T.S. Byun, D.T. Hoelzer, S.-W. Kim, B.H. Lee, Temperature dependence of strengthening mechanisms in the nanostructured ferritic alloy 14YWT: Part I—Mechanical and microstructural observations, Mater. Sci. Eng. A. 559 (2013) 101–110. doi:10.1016/j.msea.2012.08.042.

[88] T.S. Byun, J.H. Yoon, D.T. Hoelzer, Y.B. Lee, S.H. Kang, S.A. Maloy, Process development for 9Cr nanostructured ferritic alloy (NFA) with high fracture toughness, J. Nucl. Mater. 449 (2014) 290–299. doi:10.1016/j.jnucmat.2013.10.007.

[89] Z. Oksiuta, Study of microstructure and mechanical properties of 14% Cr ODS steel produced by hot isostatic pressing followed by hot forging, Inż. Mater. 1 (2016) 32–36. doi:10.15199/28.2016.3.6.

[90] J.H. Kim, T.S. Byun, J.H. Lee, J.Y. Min, S.W. Kim, C.H. Park, B.H. Lee, Effects of processing condition on the microstructural and tensile properties of 14Cr-based oxide dispersion strengthened alloys, J. Nucl. Mater. 449 (2014) 300–307. doi:10.1016/j.jnucmat.2013.09.043.

[91] I. Hilger, X. Boulnat, J. Hoffmann, C. Testani, F. Bergner, Y. De Carlan, F. Ferraro, A. Ulbricht, Fabrication and characterization of oxide dispersion strengthened (ODS) 14Cr steels consolidated by means of hot isostatic pressing, hot extrusion and spark plasma sintering, J. Nucl. Mater. 472 (2016) 206–214. doi:10.1016/j.jnucmat.2015.09.036.

[92] X. Boulnat, M. Perez, D. Fabregue, T. Douillard, M.-H. Mathon, Y. de Carlan, Microstructure evolution in nano-reinforced ferritic steel processed by mechanical alloying and spark plasma sintering, Metall. Mater. Trans. A. 45 (2014) 1485–1497. doi:10.1007/s11661-013-2107-y.

[93] I. Grants, D. Räbiger, T. Vogt, S. Eckert, G. Gerbeth, Application of magnetically driven tornado-like vortex for stirring floating particles into liquid metal, Magnetohydrodynamics. 51 (2015) 419–424.

[94] Z. Oksiuta, M. Lewandowska, P. Unifantowicz, N. Baluc, K.J. Kurzydlowski, Influence of Y2O3 and Fe2Y additions on the formation of nano-scale oxide particles and the mechanical properties of an ODS RAF steel, Fusion Eng. Des. 86 (2011) 2417–2420. doi:10.1016/j.fusengdes.2011.01.023.

[95] A. Pineau, A.A. Benzerga, T. Pardoen, Failure of metals I – Brittle and ductile fracture, Acta Mater. (2016). doi:10.1016/j.actamat.2015.12.034.

[96] J. Han Kim, T. Sang Byun, D.T. Hoelzer, Stress relaxation behavior of nanocluster-strengthened ferritic alloy at high temperatures, J. Nucl. Mater. 425 (2012) 147–155. doi:10.1016/j.jnucmat.2011.06.040.

[97] M. Praud, F. Mompiou, J. Malaplate, D. Caillard, J. Garnier, A. Steckmeyer, B. Fournier, Study of the deformation mechanisms in a Fe–14% Cr ODS alloy, J. Nucl. Mater. 428 (2012) 90–97. doi:10.1016/j.jnucmat.2011.10.046.

[98] A. Chauhan, D. Litvinov, Y. de Carlan, J. Aktaa, Study of the deformation and damage mechanisms of a 9Cr-ODS steel: Microstructure evolution and fracture characteristics, Mater. Sci. Eng. A. 658 (2016) 123–134. doi:10.1016/j.msea.2016.01.109.

[99] T. L. Anderson, Fracture Meechanics - Fundamentals and Applications, Third, Taylor & Francis, Boca Raton, Florida, USA, 2005.

[100] E. Smith, Cleavage fracture in mild steel, Int. J. Fract. 4 (1968) 131–145.

[101] ASTM Standard E1820-13, Standard test method for measurement of Fracture Toughness, (2013).

[102] K. Arora, H. Viehrig, Evaluation of the ASTM and ISO J initiation procedures by applying the unloading compliance technique to reactor pressure vessel steels, J. Test. Eval. 39 (2011). doi:10.1520/JTE103405.

[103] J.D. Landes, R. Herrera, A new look at J-R curve analysis, Int. J. Fract. 36 (1988) R9–R14. doi:10.1007/BF00034820.

[104] K. Wallin, T. Saario, P. Auerkari, H. Saarelma, K. Torronen, Comparison of potential drop and unloading compliance methods in determining ductile crack extension, in: F. Loss, E. Wessel (Eds.), Elastic-Plast. Fract. Test Methods Users Exp., ASTM International, 100 Barr Harbor Drive, PO Box C700, West Conshohocken, PA 19428-2959, 1985: pp. 363–363–12. http://www.astm.org/DIGITAL_LIBRARY/STP/PAGES/STP34535S.htm (accessed February 5, 2015).

[105] Kim Wallin, Fracture toughness of engineering materials - Estimation and application, EMAS Publishing, 2011.

[106] J. D. Landes, J calculation - front face displacement measurement on a compact specimen, Int. J. Fract. 16 (1980).

[107] A. Winkelmann, C. Trager-Cowan, F. Sweeney, A.P. Day, P. Parbrook, Many-beam dynamical simulation of electron backscatter diffraction patterns, Ultramicroscopy. 107 (2007) 414–421. doi:10.1016/j.ultramic.2006.10.006.

[108] C. Wang, M. Wang, J. Shi, W. Hui, H. Dong, Effect of microstructural refinement on the toughness of low carbon martensitic steel, Scr. Mater. 58 (2008) 492–495. doi:10.1016/j.scriptamat.2007.10.053.

[109] J. Chao, C. Capdevila, Anisotropy in mechanical properties and fracture behavior of an oxide dispersion Fe20Cr5Al alloy, Metall. Mater. Trans. A. 45 (2014) 3767–3780. doi:10.1007/s11661-014-2329-7.

[110] A. Pineau, Global and local approaches of fracture - Transferability of laboratory test results to components, in: A.S. Argon (Ed.), Top. Fract. Fatigue, 1st ed., Springer-Verlag New York, 1992.

[111] E. Altstadt, F. Bergner, A. Das, M. Houska, Effect of anisotropic microstructure of ODS steels on small punch test results, Theor. Appl. Fract. Mech. 100 (2019) 191–199. doi:10.1016/j.tafmec.2019.01.014.

[112] S. Pal, M.E. Alam, G.R. Odette, S.A. Maloy, D.T. Hoelzer, J.J. Lewandowski, Microstructure, texture and mechanical properties of the 14YWT nanostructured ferritic alloy NFA-1, in: Mech. Creep Behav. Adv. Mater., Springer International Publishing, Cham, 2017: pp. 43–54. http://link.springer.com/10.1007/978-3-319-51097-2_4 (accessed September 5, 2017).

[113] M.E. Alam, S. Pal, K. Fields, S.A. Maloy, D.T. Hoelzer, G.R. Odette, Tensile deformation and fracture properties of a 14YWT nanostructured ferritic alloy, Mater. Sci. Eng. A. 675 (2016) 437–448. doi:10.1016/j.msea.2016.08.051.

[114] R.O. Ritchie, W.L. Server, R.A. Wullaert, Critical fracture stress and fracture strain models for the prediction of lower and upper shelf toughness in nuclear pressure vessel steels, Metall. Trans. A. 10 (1979) 1557–1570. doi:10.1007/BF02812022.

[115] R.O. Ritchie, A.W. Thompson, On macroscopic and microscopic analyses for crack initiation and crack growth toughness in ductile alloys, Metall. Trans. A. 16 (1985) 233–248.

[116] W.M. Garrison, N.R. Moody, Ductile fracture, J. Phys. Chem. Solids. 48 (1987) 1035–1074. doi:10.1016/0022-3697(87)90118-1.

[117] M.F. Ashby, Work hardening of dispersion-hardened crystals, Philos. Mag. 14 (1966) 1157–1178. doi:10.1080/14786436608224282.

[118] H.F. Fischmeister, E. Navara, K.E. Easterling, Effects of alloying on structural stability and cohesion between phases in oxide/metal composites, Met. Sci. J. 6 (1972) 211–215. doi:10.1179/030634572790445803.

[119] L.J. Walpole, The elastic shear moduli of a cubic crystal, J. Phys. Appl. Phys. 19 (1986) 457.

[120] J. Turley, G. Sines, The anisotropy of Young's modulus, shear modulus and Poisson's ratio in cubic materials, J. Phys. Appl. Phys. 4 (1971) 264. doi:10.1088/0022-3727/4/2/312.

[121] J.M.J. Den Toonder, J.A.W. Van Dommelen, F.P.T. Baaijens, The relation between single crystal elasticity and the effective elastic behaviour of polycrystalline materials: theory, measurement and computation, Model. Simul. Mater. Sci. Eng. 7 (1999) 909.

[122] S.K. Yerra, C. Tekog˘lu, F. Scheyvaerts, L. Delannay, P. Van Houtte, T. Pardoen, Void growth and coalescence in single crystals, Int. J. Solids Struct. 47 (2010) 1016–1029. doi:10.1016/j.ijsolstr.2009.12.019.

[123] A.S. Argon, J. Im, R. Safoglu, Cavity formation from inclusions in ductile fracture, Metall. Trans. A. 6 (1975) 825. doi:10.1007/BF02672306.

[124] H. Liu, Y. Shen, J. Ma, P. Zheng, L. Zhang, Grain size dependence of uniform elongation in single-phase FCC/BCC metals, J. Mater. Eng. Perform. 25 (2016) 3599–3605. doi:10.1007/s11665-016-2245-7.

[125] Z. Lee, V. Radmilovic, B. Ahn, E.J. Lavernia, S.R. Nutt, Tensile deformation and fracture mechanism of bulk bimodal ultrafine-grained Al-Mg alloy, Metall. Mater. Trans. A. 41 (2009) 795–801. doi:10.1007/s11661-009-0007-y.

[126] M.S. Oskooie, H. Asgharzadeh, Strength and ductility enhancement in nanostructured AI6063 with a bimodal grain size distribution, IOP Conf. Ser. Mater. Sci. Eng. 63 (2014) 012022. doi:10.1088/1757-899X/63/1/012022.

[127] E.C. Oliver, M.R. Daymond, P.J. Withers, Interphase and intergranular stress generation in carbon steels, Acta Mater. 52 (2004) 1937–1951. doi:10.1016/j.actamat.2003.12.035.

[128] N.Y. Zolotorevsky, N.Y. Krivonosova, Effect of ferrite crystals' plastic anisotropy on residual stresses in cold-drawn steel wire, Mater. Sci. Eng. A. 205 (1996) 239–246.

[129] J. Gil Sevillano, D. González, J.M. Martínez-Esnaola, Heterogeneous deformation and internal stresses developed in BCC wires by axisymmetric elongation, Mater. Sci. Forum. 550 (2007) 75–84. doi:10.4028/www.scientific.net/MSF.550.75.

[130] J. Gil Sevillano, J. Alkorta, D. González, S. Van Petegem, U. Stuhr, H. Van Swygenhoven, In situ neutron diffraction study of internal micro-stresses developed by plastic elongation in <110> textured BCC wires, Adv. Eng. Mater. 10 (2008) 951–954. doi:10.1002/adem.200800209.

[131] A. Das, H.W. Viehrig, E. Altstadt, C. Heintze, J. Hoffmann, On the influence of microstructure on the fracture behaviour of hot extruded ferritic ODS steels, J. Nucl. Mater. 497 (2017) 60–75. doi:10.1016/j.jnucmat.2017.10.051.

[132] C.A. Williams, P. Unifantowicz, N. Baluc, G.D.W. Smith, E.A. Marquis, The formation and evolution of oxide particles in oxide-dispersion-strengthened ferritic steels during processing, Acta Mater. 61 (2013) 2219–2235. doi:10.1016/j.actamat.2012.12.042.

[133] J. Macías-Delgado, T. Leguey, V. de Castro, M.A. Auger, M.A. Monge, P. Spätig, N. Baluc, R. Pareja, Microstructure and tensile properties of ODS ferritic steels mechanically alloyed with Fe 2 Y, Nucl. Mater. Energy. 9 (2016) 372–377. doi:10.1016/j.nme.2016.09.019.

Publications and Presentations

Publications

April 2017 EFFECT OF MICROSTRUCTURAL ANISOTROPY ON FRACTURE TOUGHNESS OF HOT ROLLED 13CR ODS STEEL - THE ROLE OF PRIMARY AND SECONDARY CRACKING

Journal of Nuclear Materials

A. Das, H.W. Viehrig, F. Bergner, C. Heintze, E. Altstadt, J. Hoffmann

October 2017 ON THE INFLUENCE OF MICROSTRUCTURE ON THE FRACTURE BEHAVIOUR OF HOT-EXTRUDED FERRITIC ODS STEELS

Journal of Nuclear Materials

A. Das, H.W. Viehrig, E. Altstadt, C. Heintze, , J. Hoffmann

Oral presentations

March 2015 FRACTURE BEHAVIOR AND MECHANISMS OF ODS STEELS

3rd ODISSEUS Workshop on ODS steels, Oxford University, England

A. Das, H.W. Viehrig

October 2015 FRACTURE BEHAVIOR AND MECHANISMS OF ODS STEELS

Klausurtagung for University of Siegen in Bonn, Germany

A. Das, H.W. Viehrig

April 2016 SMALL SPECIMEN FRACTURE TOUGHNESS AND SECONDARY CRACKING IN ODS STEELS

4th ODISSEUS Workshop on ODS steels, HZDR, Dresden, Germany

A. Das, H.W. Viehrig

December 2016 FRACTURE BEHAVIOR AND MECHANISMS OF ODS STEELS

KOMPOST Doktoranden Seminar, HZDR, Dresden, Germany

A. Das, H.W. Viehrig

June 2017 EFFECT OF MICROSTRUCTURE ON THE FRACTURE BEHAVIOR OF HOT-EXTRUDED FERRITIC ODS STEELS

4th International Workshop on ODS materials, HZDR, Dresden, Germany

A. Das, H.W. Viehrig

October 2017 THE INFLUENCE OF MICROSTRUCTURE ON THE FRACTURE BEHAVIOR OF FERRITIC ODS STEELS

Klausurtagung for University of Siegen in Remagen-Bonn, Germany

A. Das, H.W. Viehrig

Poster presentations

December 2015 FRACTURE BEHAVIOR AND MECHANISMS OF ODS STEELS

KOMPOST Doktoranden Seminar, HZDR, Dresden, Germany

A. Das, H.W. Viehrig

September 2016 FRACTURE BEHAVIOR AND MECHANISMS OF ODS STEELS

Material Science and Engineering Congress in Darmstadt, Germany

A. Das, H.W. Viehrig

October 2016 FRACTURE BEHAVIOR AND MECHANISMS OF ODS STEELS

PhD Seminar for HZDR, Oberwiesenthal, Germany

A. Das, H.W. Viehrig

December 2017 THE INFLUENCE OF MICROSTRUCTURE ON THE FRACTURE BEHAVIOR OF FERRITIC ODS STEELS

KOMPOST Doktoranden Seminar, Technische Universität Dresden, Dresden, Germany

A. Das, H.W. Viehrig